2016

# Electrochemical Reduction Of Carbon Dioxide On Carbon Nanostructures: Defect Structures & Electrocatalytic Activity

Pranav Parag Sharma
*University of South Carolina*

## Recommended Citation

Sharma, P. P.(2016). *Electrochemical Reduction Of Carbon Dioxide On Carbon Nanostructures: Defect Structures & Electrocatalytic Activity.* (Doctoral dissertation). Retrieved from http://scholarcommons.sc.edu/etd/3785

# ELECTROCHEMICAL REDUCTION OF CARBON DIOXIDE ON CARBON NANOSTRUCTURES: DEFECT STRUCTURES & ELECTROCATALYTIC ACTIVITY

by

Pranav Parag Sharma

Bachelor of Technology
National Institute of Technology, Warangal, 2007

Master of Science
Clarkson University, 2010

---

Submitted in Partial Fulfillment of the Requirements

For the Degree of Doctor of Philosophy in

Chemical Engineering

College of Engineering & Computing

University of South Carolina

2016

Accepted by:

Xiao-Dong Zhou, Major Professor

Bihter Padak, Committee Member

John R. Regalbuto, Committee Member

John W. Weidner, Committee Member

Guiren Wang, Committee Member

Lacy Ford, Senior Vice Provost and Dean of Graduate Studies

# DEDICATION

To my parents and my wife, Udita

# ACKNOWLEDGEMENTS

I would like to express my gratitude towards my advisor Dr. Xiao-Dong Zhou, for his continuous guidance, support and encouragement during this doctoral work. He always encouraged me to think deeply and this has helped me improve as a researcher. I also thank my thesis committee members, Dr. Bihter Padak, Dr. John R. Regalbuto and Dr. Guiren Wang for their time and suggestions.

I would like to thank Dr. Jingjie Wu at Rice University and Dr. Fu-Sheng Ke at Wuhan University for helping me throughout my doctoral study with valuable discussions. I am grateful to Dr. Perry J. Pellechia at the Department of Chemistry for helping me with nuclear magnetic resonance spectroscopy measurements.

I would also like to acknowledge the help provided by my colleagues at Rice University, especially, Dr. Ram Yadav for synthesizing the N-doped carbon nanostructures and Mingjie Liu with density functional theory calculations.

Finally, I thank all my friends and family members, especially, my wife Udita, for the support, care and encouragement.

# ABSTRACT

The advantages of the electrochemical conversion of carbon dioxide to fuels using renewable energy sources are two-fold: (1) it has the potential to accomplish a carbon-neutral energy cycle and (2) it can provide an approach to tackle the environmental challenges caused by anthropogenic carbon dioxide emissions. Although thermodynamically possible, the kinetics of carbon dioxide reduction to fuels remains challenging and therefore, an efficient and robust electrocatalyst is needed to promote the reaction. The ideal catalyst for the electrochemical $CO_2$ reduction must be capable of mediating multiple proton-coupled electron transfer reactions at low overpotentials, suppressing the concurrent hydrogen evolution reaction, converting $CO_2$ to desired chemicals with high selectivity, and achieving long-term stability. Extensive research has been carried out on metallic electrocatalysts during the past three decades; however, none of these materials are simultaneously efficient and stable for practical purposes. This Ph.D. dissertation focuses on the investigation of the electro-reduction of $CO_2$ on carbon nanostructures with a focus on understanding the relationship between defect structures and electrocatalytic activity.

The initial focus of this work was to accomplish active performance and durability for electrosynthesis of fuels from $CO_2$ using cost-effective catalysts. N-doped carbon nanotubes (NCNTs) were demonstrated as highly efficient, selective and more importantly, stable catalysts to achieve $CO_2$ conversion to CO. The catalytic activity of these NCNTs was further benchmarked against other metallic catalysts reported in literature **(Chapter 2)**. Compared to noble metals Ag & Au, these NCNTs exhibited a lower overpotential to achieve similar selectivity towards CO formation. The second part of this work was a study of the dependence of catalytic activity, i.e., the overpotential and selectivity for CO formation on the defect structures (pyridinic, graphitic, pyrrolic-N) inside NCNTs. The presence of both pyridinic and graphitic-N was found to significantly decrease the absolute overpotential and increase the selectivity towards CO formation **(Chapter 3)**. The third part of this thesis work was to investigate $CO_2$ reduction on N-doped graphene, in order to explore morphology effects on catalytic activity of NCNTs towards CO formation **(Chapter 4)**. Overall, pyridinic-N defects exhibited the highest catalytic activity; thereby suggesting the directions for developing carbon nanostructures as metal-free electrocatalysts for $CO_2$ reduction.

# TABLE OF CONTENTS

DEDICATION .......... iii

ACKNOWLEDGEMENTS .......... iv

ABSTRACT .......... v

LIST OF TABLES .......... x

LIST OF FIGURES .......... xi

LIST OF SYMBOLS .......... xvi

LIST OF ABBREVIATIONS .......... xvii

Chapter 1: Introduction and Thesis Objectives .......... 1

- 1.1 Rising $CO_2$ Levels .......... 1
- 1.2 Electrochemical Reduction of $CO_2$ .......... 2
- 1.3 Thermodynamic Aspects: $CO_2$ Electro-reduction .......... 2
- 1.4 Kinetic Aspects: $CO_2$ Electro-reduction .......... 4
- 1.5 Thesis Objectives .......... 7
- References .......... 9

Chapter 2: Achieving Highly Efficient, Selective and Stable $CO_2$ Reduction on Nitrogen-doped Carbon Nanotubes .......... 14

- 2.1 Introduction .......... 14
- 2.2 Experimental Methods .......... 15
- 2.3 Results & Discussion .......... 18
- 2.4 Conclusions .......... 35

References ....................................................................................................36

Chapter 3: Nitrogen Doped Carbon Nanotube Arrays for High Efficiency Electrochemical Reduction of $CO_2$: On the Understanding of Defects, Defect Density, and Selectivity ....................................................................................................39

3.1 Introduction ....................................................................................................39

3.2 Experimental Methods ....................................................................................................40

3.3 Results & Discussion ....................................................................................................43

3.4 Conclusions ....................................................................................................56

References ....................................................................................................57

Chapter 4: Incorporation of Nitrogen Defects for Efficient Reduction of $CO_2$ via Two-Electron Pathway on Three-Dimensional Graphene Foam ....................................................................................................61

4.1 Introduction ....................................................................................................61

4.2 Experimental Methods ....................................................................................................63

4.3 Results & Discussion ....................................................................................................65

4.4 Conclusions ....................................................................................................76

References ....................................................................................................77

Chapter 5: Electrocatalytic Conversion of Carbon Dioxide to Fuels: A Review on the Interaction between $CO_2$ and the Liquid Electrolyte ....................................................................................................80

5.1 $CO_2$ in Aqueous Electrolyte ....................................................................................................82

5.2 $CO_2$ in Organic Solvents ....................................................................................................103

5.3 $CO_2$ in Ionic Liquids ....................................................................................................108

5.4 Summary ....................................................................................................118

References ....................................................................................................119

Chapter 6: Summary and Future Directions ....................................................................................................129

6.1 Summary ....................................................................................................129

6.2 Future Directions ........................................................................................131

Appendix A: Selective Formation of $C_2$ Products from the Electrochemical Conversion of $CO_2$ on Cu Electrodes Comprised of Nanoporous Ribbon Arrays ..................................134

Appendix B: Electrocatalytic Activity of Rutile Titanium Dioxide towards the Conversion of Carbon Dioxide to CO and Formate ......................................................148

Appendix C: The Role of Nonstoichiometry on the Electrocatalytic Properties of $TiO_{2-x}$ towards the Conversion of Carbon Dioxide to Fuels......................................................161

Appendix D: Author's Publications...................................................................171

# LIST OF TABLES

Table 1.1 Equilibrium standard reduction potentials for conversion of $CO_2$ to various products....3

Table 1.2 Products from $CO_2$ reduction at different metal electrodes under various conditions....6

Table 2.1 Kinetic data of NCNTs, Au and Ag for electroreduction of $CO_2$ to CO. $j_0$ denotes the exchange current density....34

Table 3.1 Double layer capacitance for various electrodes. The geometric area of all electrodes is 1 $cm^2$....52

Table 4.1 Apparent exchange current density of N-doped graphene, N-doped CNTs, and metal electrodes....70

Table 4.2 Gas permeability of various electrodes measured at a compression ratio of 10%....73

Table 5.1 Products from $CO_2$ reduction in different electrolyte systems at various metal electrodes....84

Table 5.2 Thermodynamic Gibbs energy of formation of various species at 25°C and 1 atm....87

Table 5.3 Comparison of solubility of $CO_2$ in water, and water containing NaCl in different concentrations at 1 bar pressure and various temperatures....89

Table 5.4 Comparison of solubility of $CO_2$ in water, and water containing NaCl in different concentrations at 303.15 K and various pressures....89

Table 5.5 Calculated asymmetric stretching frequencies for $CO_2$ and $H_2O$ in $CO_2$-$(H_2O)$ n, n=1,2,…,8. $CO_2$ and $H_2O$ are denoted by C and W respectively....100

Table 5.6 $CO_2$ solubility in organic solvents....103

# LIST OF FIGURES

Figure 1.1 Global energy consumption in 2014 showing dependency on fossil fuels ........3

Figure 1.2 Commonly proposed $CO_2$ reduction routes in aqueous acidic medium............5

Figure 2.1 Physical characterization of NCNTs. (a) and (b) SEM images of NCNTs at low and high magnification, respectively. (c)TEM images of NCNTs, inset showing a single multi-wall NCNT. (d) EELS element mapping of N and C. (e) XRD pattern. (f) Raman spectrum. (g) A representative XPS of N 1s for NCNTs. The N1s is deconvoluted into three peaks representing three different N functionalities. (h) Statistic N atomic content and relative percent. (i) A schematic of graphitic, pyrrolic and pyridinic N configuration..........................................................................................................20

Figure 2.2 TEM characterization of NCNTs. (a) Low magnification images of NCNTs and (b) the corresponding tube diameter distribution.......................................................21

Figure 2.3 XPS characterization of NCNTs. (a) Survey scan of NCNTs showing C, N and O elements. (b) Fine scan of C 1s.........................................................................21

Figure 2.4 SEM images of pure CNTs. (a) A low magnification image showing the CNT arrays. (b) A high resolution image ....................................................................22

Figure 2.5 Microstructural characterization of pure CNTs. (a) XRD showing the same peak diffraction as NCNTs. A small diffraction peak assigned to iron species was observed. (b) Raman spectrum ..........................................................................22

Figure 2.6 Performance of NCNTs for selectively electrochemical reduction of $CO_2$ to CO. (a) CVs for NCNTs in Ar and $CO_2$ saturated 0.1 M $KHCO_3$ electrolyte, 50 mV $s^{-1}$. (b) Dependence of FE of CO on applied cell potential during electrocatalysis of $CO_2$ reduction for both NCNTs and CNTs catalysts. (c) Partial current density of CO versus applied cell potential for NCNTs and CNTs catalysts. (d) Stability of performance of NCNTs for $CO_2$ reduction operated at potentiostatic mode of -0.8 V for 10 h. Both current density and FE of CO maintain steady over the duration of test...........................24

Figure 2.7 Electrochemical activity of Ag nanoparticles for $CO_2$ reduction. (a) Faradaic efficiency for CO, and (b) total current density at each tested cell voltage.......................25

Figure 2.8 Electrochemical activity of Au powder for $CO_2$ reduction. (a) Faradaic efficiency of CO, and (b) total current density at each tested cell voltage .......................25

Figure 2.9 Comparison of overpotential and yield of CO of NCNTs with metal catalysts. For Au, Ag, and $MoS_2$ catalyst, the lowest overpotential is chosen to reach a comparable FE of CO of around 80%. For Zn, Cu, and Sn catalyst, the overpotential for the maximum FE of CO is used ........ 26

Figure 2.10 Electrochemical activity of Zn powder for $CO_2$ reduction. (a) Faradaic efficiency of CO and formate, and (b) total current density at each tested cell voltage .... 27

Figure 2.11 Electrochemical activity of Cu nanoparticles for $CO_2$ reduction. (a) Faradaic efficiency for CO, formate and $C_2H_4$, (b) Faradaic efficiency for $CH_3OH$ and $C_2H_5OH$, and (b) total current density at each tested cell voltage ........ 27

Figure 2.12 Cyclic voltammetry of NCNTs and CNTs in the electrolyte of 0.1 M KOH saturated with Ar. Scan rate: 50 mV/s. ........ 28

Figure 2.13 Physical characterization of NCNTs after long term operation. (a) Low magnification TEM images, (b) a high magnification TEM image of a single NCNT, (c) the survey spectrum of XPS, the F coming from the Nafion binder, (d) and (e) fine scans of C1s and N1s respectively ........ 29

Figure 2.14 Kinetic activity of NCNTs and metal catalysts. (a) The correlation of calculated adsorption energies of the key bound intermediates of COOH* and CO*. (b) The experimental Tafel plots of NCNTs, Au and Ag electrodes ........ 33

Figure 3.1 Physical characterization of as-synthesized NCNTs (a, b) Cross-sectional SEM images, (c) TEM image, (d) Raman spectra of NCNTs synthesized using ACN precursor at various temperatures ........ 44

Figure 3.2 Raman spectra of NCNTs synthesized using dimethyl formamide (DMF) and triethylamine (TEA) precursors at 850 °C, denoted by DMF-850 and TEA-850 respectively ........ 45

Figure 3.3 XPS results of N 1s of NCNTs synthesized using ACN precursor at various growth temperatures and comparison of different N contents in the synthesized NCNTs ........ 45

Figure 3.4 (a) Faradaic efficiency for CO versus potential on NCNTs synthesized using different precursors and growth temperatures. (b) Tafel plots for CO formation on NCNTs ........ 47

Figure 3.5 Dependence of electrocatalytic performance of NCNTs synthesized using acetonitrile (ACN) precursor at growth temperatures, i.e., 750, 850 and 950°C. (a) Faradaic efficiency for CO, (b) Faradaic efficiency for formate, (c) Partial current density for CO and (d) Partial current density for formate at different measured cell voltages .... 48

Figure 3.6 Electrocatalytic performance of NCNTs synthesized at 850°C using different precursors, i.e., acetonitrile (ACN), dimethylformamide (DMF) and triethylamine (TEA) in comparison to pristine CNTs (CNT). (a) Faradaic efficiency for CO, (b) Faradaic efficiency for formate, (c) Partial current density for CO and (d) Partial current density for formate at different measured cell voltages ................................................................49

Figure 3.7 Cyclic voltammograms of different electrodes studied in 0.1 M $Na_2SO_4$ at various scan rates for estimation of double layer capacitance. (a) Carbon gas diffusion layer (GDL) (b) Pristine CNTs (c) NCNTs synthesized using DMF precursor (NCNTs-DMF) (d) NCNTs synthesized using TEA precursor (NCNTs-TEA). The geometric area of all electrodes is 1 $cm^2$ ..........................................................................................50

Figure 3.8 Comparison of double layer capacitance values for different NCNT electrodes. The geometric area of all electrodes is 1 $cm^2$ ...................................................................53

Figure 3.9 (a) The onset potential and maximum Faradaic efficiency for CO formation as a function of N-content in the synthesized NCNTs (b) Schematic illustrating CO formation on the NCNTs and free energy diagram at equilibrium potential for $CO_2$ reduction on different N-defects, i.e. pyridinic, pyrrolic and graphitic N in comparsion to pristine CNTs. C, O and H atoms are represented by grey, red and white spheres, while pyridinic, pyrrolic and graphitic N defects are shown using blue, pink and green spheres respectively ...............................................................................................................54

Figure 4.1 Raman spectra of pristine graphene and N-doped graphene ............................66

Figure 4.2 Physical characterization of N-doped graphene foam. (a) A SEM image showing a representative graphene foam with an open frame structure. (b) High magnification SEM image of a NG-800 sheet. (c) TEM image of a NG-800 sheet. (d) High resolution TEM image of NG-800 sheet, and inset is the FFT pattern. (e) XPS of N 1s. (f) N content distribution as a function of different doping temperatures....................67

Figure 4.3 A representative XPS of NG-800. (a) Survey scan and (b) fine scan of C 1s ...............................................................................................................................68

Figure 4.4 Performance of NG-800 for $CO_2$ reduction over long-term operation. Total current density versus time (–, left axis) and FE for CO production versus time (•, right axis) in 0.1 M $KHCO_3$ (pH 6.8 after $CO_2$ saturation) at (a) -0.30, (b) -0.40, (c) -0.50 V and (d) -0.58 V versus RHE...........................................................................................68

Figure 4.5 Comparison of the electrocatalytic activities of nitrogen-doped graphene with doping temperature ranging from 700 to 1000 °C. (a) Faradaic efficiency of CO vs potential. (b) Faradaic efficiency of $HCOO^-$ vs potential. (c) Maximum Faradaic efficiency of CO and its corresponding potential versus N functionality content .............72

Figure 4.6 Tafel plots of NG electrodes for $CO_2$ reduction ..............................................72

Figure 4.7 DFT modeling of $CO_2$ electrocatalysis on NG. (a) Free energy diagram of electrochemical reduction of $CO_2$ to CO on NG and (b) schematic of N configuration and $CO_2$ reduction pathway ......75

Figure 5.1 The Keeling curve, carbon dioxide concentrations at the Mauna Loa Observatory ......81

Figure 5.2 A schematic of the full electrochemical cell featuring a buffer layer circulating a liquid-electrolyte ......83

Figure 5.3 Performance of full electrochemical cell with and without a buffer layer ......83

Figure 5.4 Variations in concentration of $CO_2$, $HCO_3^-$ and $CO_3^{2-}$ with pH of the aqueous medium. DIC = 2.1 mmol/kg, Salinity, S = 35 and T = 25 °C. ($K_1^* = K_1$; $K_2^* = K_2$) ......88

Figure 5.5 Illustration of the effect of temperature, pressure and salinity (ionic strength) on the concentration of $CO_2$, $HCO_3^-$ and $CO_3^{2-}$ species. ($K_1^* = K_1$; $K_2^* = K_2$) ......90

Figure 5.6 Diffusion coefficients of $CO_2$ in ultra-pure DI water at different temperatures and pressures ......92

Figure 5.7 Calculated NEXAFS carbon K-edge spectra for various species (Adapted) ...94

Figure 5.8 Pair correlation function between water and carbon dioxide. a) C atom in $CO_2$ b) O atom in $CO_2$. Solid and dashed lines refer to O and H sites in water respectively....95

Figure 5.9 Structures of $CO_2$-$H_2O$ complex in a T and H-type configuration ......95

Figure 5.10 Optimized structure of $CO_2$-$H_2O$ dimer ......97

Figure 5.11 Optimized structure of $CO_2$-$H_2O$ trimer ......97

Figure 5.12 Gibbs free energy change with temperature for $CO_2$-($H_2O$) n, n=1,2,..,8 ......99

Figure 5.13 Schematic illustration of processes in the double layer that play a role in the kinetics of $CO_2$ to CO conversion on a Ag cathode when using (a) KOH or (b) KCl as the electrolyte ......102

Figure 5.14 Nyquist plot for different electrolytes obtained via electrochemical impedance spectroscopy at a cell potential of -2.25 V ......102

Figure 5.15 Optimized structure of complex formed during $CO_2$ and DME interaction ......105

Figure 5.16 Optimized structure of the acetaldehyde-$CO_2$ complex ......106

Figure 5.17 Raman spectra of acetaldehyde (A) the carbonyl stretch region in He (black) and $CO_2$ (red). (B) the aldehydic C-H stretch in He (black) and $CO_2$ (blue). Insets show the intensity changes upon complexation ........................................................................107

Figure 5.18 A schematic of how the free energy of the system changes during the reaction $CO_2 + 2H^+ + 2e^- \rightleftharpoons CO + H_2O$ in water or acetonitrile (solid line) or EMIM-$BF_4$ (dashed line) ........................................................................................................................109

Figure 5.19 Structure of [emim] cation in an ionic liquid ..............................................110

Figure 5.20 Correlation between gas-phase cation-anion interaction energy and the experimental $CO_2$ solubility at 1 bar and 298 K for four ionic liquids with the same [emim] cation but different anions (Top). Correlation between the gas-phase $CO_2$ anion interaction energy and the experimental $CO_2$ solubility at 1 bar and 298 K for four ionic liquids with the same [emim] cation but different anions (Bottom)................................111

Figure 5.21 The spatial radial distribution function of $CO_2$ (yellow) around $B(CN)_4$ (left) and emim (right) ..........................................................................................................114

Figure 5.22 Raman spectra of [bmim][$PF_6$]-$CO_2$ system at 313 K. From top to bottom 1) [bmim][$PF_6$]-$CO_2$ at 140 bar. 2) [bmim][$PF_6$] without $CO_2$. 3) Pure $CO_2$. Arrows indicate bands of pure $CO_2$..........................................................................................................115

Figure 5.23 Reaction Pathways for the Electrochemical Reduction of $CO_2$ in the (A) Absence and (B, C) Presence of [emim][$Tf_2N$] at a Pb Electrode in acetonitrile...........117

# LIST OF SYMBOLS

| | |
|---|---|
| $\Delta G$ | Gibbs free energy of reaction |
| $E^0$ | Equilibrium potential |
| $\eta$ | Overpotential for an electrochemical reaction |
| $\mu$ | Chemical potential of a species |
| $k$ | Boltzmann’s constant |
| $K$ | Equilibrium constant for a reaction |
| $R$ | Universal gas constant |
| $S$ | Entropy |
| $T$ | Absolute temperature |
| $D$ | Diffusivity |
| $H$ | Henry’s constant |

# LIST OF ABBREVIATIONS

| | |
|---|---|
| ACN | Acetonitrile |
| AES | Auger Electron Spectroscopy |
| CHE | Computational Hydrogen Electrode |
| CNTs | Pristine Carbon Nanotubes |
| CRR | Carbon Dioxide Reduction Reaction |
| CVD | Chemical Vapor Deposition |
| DMF | Dimethyl Formamide |
| DFT | Density Functional Theory |
| DOS | Density of States |
| ECSA | Electrochemical Surface Area |
| EELS | Electron Energy Loss Spectroscopy |
| EIS | Electrochemical Impedance Spectroscopy |
| FE | Faradaic Efficiency |
| FEG | Field Emission Gun |
| GC | Gas Chromatography |
| GDE | Gas Diffusion Electrode |
| GDL | Gas Diffusion Layer |
| HER | Hydrogen Evolution Reaction |
| HRTEM | High Resolution Transmission Electron Microscopy |
| NCNTs | N-doped Carbon Nanotubes |
| NG | N-doped Graphene |

| | |
|---|---|
| NMR | Nuclear Magnetic Resonance |
| OER | Oxygen Evolution Reaction |
| ORR | Oxygen Reduction Reaction |
| PEMFC | Proton Exchange Membrane Fuel Cell |
| SCE | Saturated Calomel Electrode |
| SEM | Scanning Electron Microscopy |
| TEA | Triethylamine |
| TEM | Transmission Electron Microscopy |
| TSP | Sodium 3-(trimethylsilyl) Proportionate 2, 2, 3, 3-d (4) |
| XPS | X-ray Photoelectron Spectroscopy |
| XRD | X-ray Diffraction |

# Chapter 1

# Introduction and Thesis Objectives

## 1.1 Rising $CO_2$ Levels

The current global power consumption is ~ 15 TW, which is projected to double by 2050 and then to more than triple by the end of the century.[1] A statistical review done by British Petroleum in 2015 shows that 86% of our energy needs are met from fossil fuels, i.e. coal, oil and natural gas (**Figure 1.1**). There are, however, major drawbacks of using fossil fuels as energy sources such as its limited availability and environmental concerns. $CO_2$ is the chief greenhouse gas generated by the combustion of fossil fuels and its concentration in atmosphere has increased tremendously from 320 ppm in 1960 to ~ 400 ppm in March, 2015 (www.CO2now.org). If the concentration of $CO_2$ is allowed to increase further, it might lead to an increase in global temperatures and considerable changes in global climate.[2, 3, 4, 5, 6] Hence, it is of paramount importance to reduce $CO_2$ emission and develop means to capture and utilize $CO_2$, thereby decreasing its accumulation in the atmosphere. A possible way of recycling $CO_2$ from the atmosphere is to make useful fuels or industrial chemicals by reducing it using electricity generated from renewable energy sources, such as solar and/or wind energy, resulting in a carbon-neutral energy cycle.[7, 8, 9]

## 1.2 Electrochemical Reduction of $CO_2$

A number of reviews are available that summarize the literature on the electrochemical $CO_2$ reduction.[10, 11, 12, 13] Electrochemical reduction of $CO_2$ coupled with renewable energy sources can potentially offer a synthetic route to generate carbon neutral fuels or industrial chemicals that are conventionally derived from petroleum. The thermodynamic stability of $CO_2$, however, makes the activation of $CO_2$ difficult and an input electrical energy is needed to drive the $CO_2$ reduction process. Electrolyzers can be employed by applying a potential difference between two electrodes (anode and cathode), thereby allowing electrochemical reduction of $CO_2$ at cathode.[14, 15] In this regard, solid oxide electrolysis cells can be used at high temperatures (750-900°C) at high current densities, however, only CO can be produced at these process conditions.[15] On the other hand, low temperature $CO_2$ electrolysis (25-100°C) might offer a cost-effective method capable of producing various hydrocarbons, alcohols, formic acid etc., from $CO_2$ reduction.[16, 17, 18, 19, 20]

## 1.3 Thermodynamic Aspects: $CO_2$ Electro-reduction

The equilibrium reduction potentials vs. RHE for the formation of various products from $CO_2$ at pH 0 ($[H^+] = 1$ M) are listed in **Table 1.1**. These energy barriers can be further reduced by decreasing the pH, however, as it can be seen because of the involvement of protons that $CO_2$ reduction reaction competes with concurrent hydrogen evolution reaction (HER). The equilibrium reduction potential for hydrogen evolution ($2H^+ + 2e^- = H_2$) is 0 V vs. RHE at pH 0.

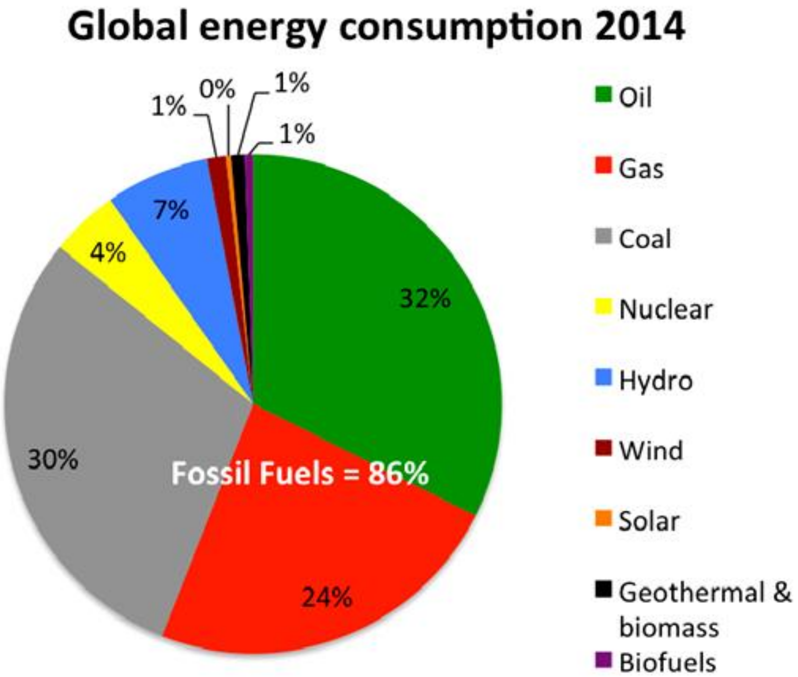

**Figure 1.1.** Global energy consumption in 2014 showing dependency on fossil fuels (British Petroleum Statistical Review, 2015)

**Table 1.1.** Equilibrium standard reduction potentials for conversion of $CO_2$ to various products

| | |
|---|---|
| $CO_2 + 4H^+ + 4e^- = C + 2H_2O$ | $E^{eq} = 0.21$ V |
| $CO_2 + 2H^+ + 2e^- = CO + H_2O$ | $E^{eq} = -0.10$ V |
| $CO_2 + 2H^+ + 2e^- = HCOOH$ | $E^{eq} = -0.20$ V |
| $2CO_2 + 2H^+ + 2e^- = H_2C_2O_4$ | $E^{eq} = -0.50$ V |
| $CO_2 + 4H^+ + 4e^- = CH_2O + H_2O$ | $E^{eq} = -0.07$ V |
| $CO_2 + 6H^+ + 6e^- = CH_3OH + H_2O$ | $E^{eq} = 0.02$ V |
| $CO_2 + 8H^+ + 8e^- = CH_4 + 2H_2O$ | $E^{eq} = 0.17$ V |
| $2CO_2 + 12H^+ + 12e^- = C_2H_4 + 4H_2O$ | $E^{eq} = 0.06$ V |
| $2CO_2 + 12H^+ + 12e^- = C_2H_5OH + 3H_2O$ | $E^{eq} = 0.084$ V |

## 1.4 Kinetic Aspects: $CO_2$ Electro-reduction

The electrochemical reduction of $CO_2$ proceeds through four principal pathways[21] (**Figure 1.2**). (1) a reaction between $CO_2^-$ (ad) and $CO_2$ (g) giving CO (g) through disproportionation; (2) formation of a $\bullet CO_2^-$ radical, with the end product dependent upon the nature of the electrolyte; (3) formation of a •COOH (ad) species leading to the formation of formate; and (4) formation of a range of adsorbed reduced $CO_2$ (i.e., $CO_x^{y-}$) species, giving yields of CO, hydrocarbons and alcohols.[21] The involvement of multiple proton-electron transfer in $CO_2$ reduction tends to make it sluggish and therefore, a catalyst is needed to improve its kinetics.[22, 23, 24, 25] In general, an underlying requirement for a desirable electrocatalyst for $CO_2$ reduction is its capability of mediating multiple electron and proton transfers at relatively low overpotentials while suppressing the competing hydrogen evolution reaction.[26, 27, 28] Metals have been extensively studied as electrocatalysts for this purpose in both aqueous and non-aqueous medium as detailed in the **Table 1.2**.[21] Out of these metals, Sn[17, 29, 30, 31, 32, 33, 34] and Cu[35, 36, 37] and are considered as promising electrocatalysts for $CO_2$ conversion to fuels because of their low cost, easy availability and reasonable overall Faradaic efficiency towards $CO_2$ reduction. Cu is particularly interesting because of its unique ability to form hydrocarbons and alcohols at high reaction rates from $CO_2$ reduction.[16, 38, 39, 40, 41] The stability of both these catalysts, however, is a concern as the catalytic activity degrades within few hours.[18, 34] Therefore, a catalyst capable of reducing $CO_2$ with high energy efficiency (> 60%) and selectivity (Faradaic efficiency > 90%), in a long-term operation at high current densities (> 250 mA/cm$^2$) remains elusive.

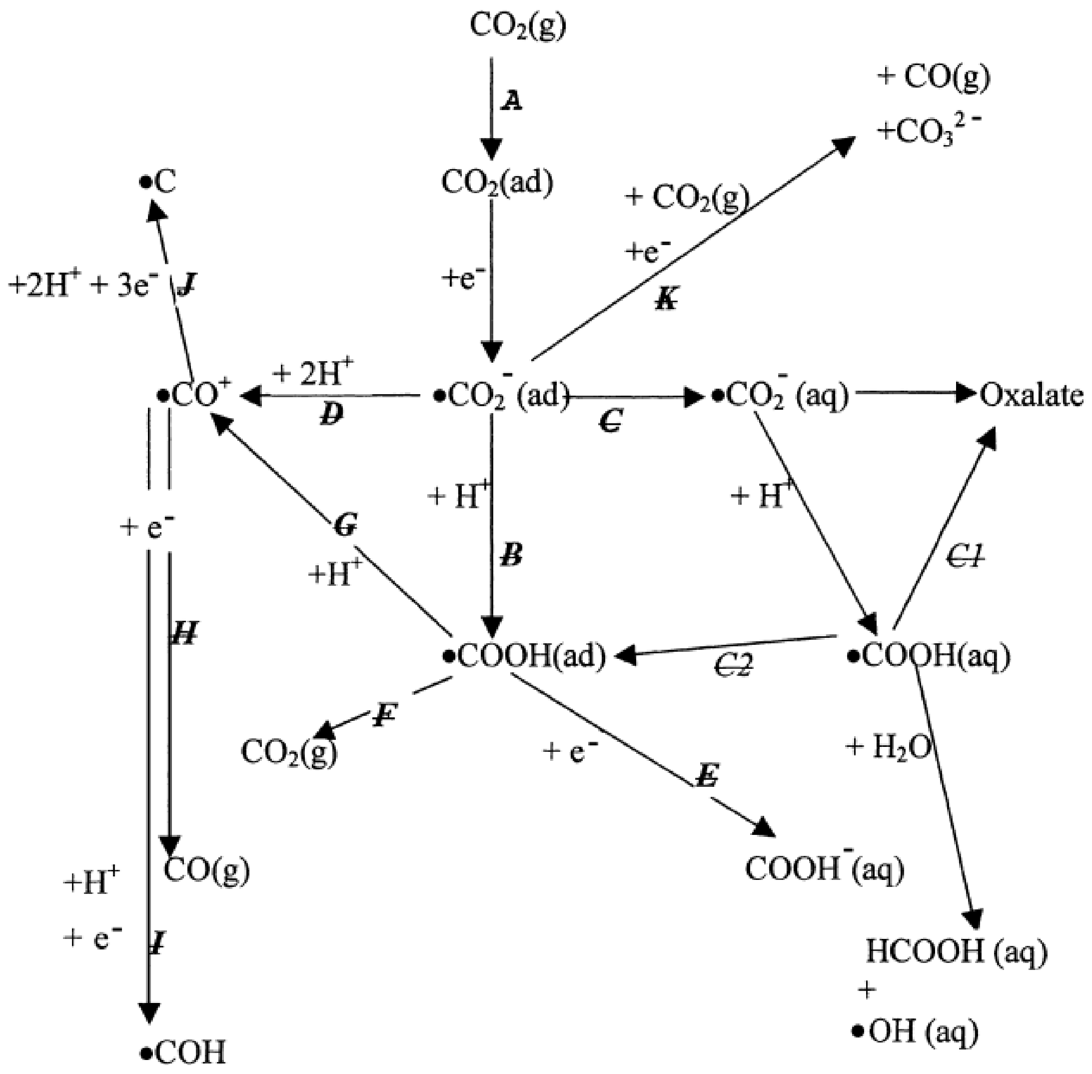

**Figure 1.2.** Commonly proposed $CO_2$ reduction routes in aqueous acidic medium[21]

Non-metallic catalysts for electrochemical $CO_2$ reduction, on the other hand, have received little attention. Oxide-derived catalysts, specifically, Au and Cu have been demonstrated to achieve a higher catalytic activity than the respective polycrystalline metal electrodes.[12, 18, 19, 42] The difference in catalytic activity of these electrodes stems from high density of step defects[18, 43, 44, 45] or presence of grain boundaries on the catalyst surface.[19, 35, 46, 47] Recently, doped carbon nanofibers have also been successfully employed for efficient and selective $CO_2$ reduction to CO[48] and formate[49]; however, the dependency of electrocatalytic activity on different defect structures remains unknown.

**Table 1.2.** Products from $CO_2$ reduction at different metal electrodes under various conditions

| **Metals** | **Valence Electron Configuration** | **Electrolyte (Aqueous/Non-aqueous)** | **Major Products** | **Selectivity (Maximum Faradaic efficiency, %)** | **Reference** |
|---|---|---|---|---|---|
| Pb, Hg, Sn, In, Bi | s/sp | Aqueous | HCOOH (all) | 90 | 17 |
| | | Non-aqueous<br>(Propylene carbonate) | $(COOH)_2$ for Pb, Hg | 80 | 50 |
| | | Non-aqueous<br>(Methanol) | CO (disproportionation) for Sn | 72 | 51 |
| Cu | $4s^1$/d group | Aqueous | CO | 30 | 10 |
| | | | HCOOH | 35 | |
| | | | $CH_4$ | 40 | |
| | | | $C_2H_4$ | 20 | |
| | | | $C_2H_5OH$ | 22 | 52 |
| | | Non-aqueous<br>(Propylene carbonate) | $CO/(COOH)_2$ | 70 | 53 |
| | | Non-aquoeus<br>(Methanol) | HCOOH | 17 | 54 |
| | | | $CH_4$ | 22 | |
| | | | $C_2H_4$ | 20 | |
| Ni, | Fully filled d- | Aqueous | CO (all) | < 10 | 50 |

| | | | | | |
|---|---|---|---|---|---|
| Pd,Pt | orbital | | HCOOH for Pd | 100 | 55 |
| | | Non-aqueous (Propylene carbonate) | CO/(COOH)$_2$ | 60 | 53 |
| Fe, Co, Rh, W, Ir, Re | Partly filled d-orbital | Aqueous | $H_2$ (all) | 100 | 56 |
| | | Non-aqueous (Methanol) | CO/(COOH)$_2$ for Re | 87 | 57 |
| Zn, Ag, Au, Cd | s only/s$^1$ | Aqueous | CO (disproportionation) for Zn, Ag, Au | 94 | 58 |
| | | Non-aqueous (Methanol) | CO for Zn, Ag, Au | 70 | 51 |
| | | Non-aqueous (1-Ethyl-3-methylimidazolium tetrafluoroborate) | CO for Ag | 100 | 59 |

## 1.5 Thesis Objectives

With this given background, this thesis focuses on the development of metal free electrocatalysts for $CO_2$ reduction. In this regard, N-doped carbon nanotubes (NCNTs) **(Chapter 2)** were studied as electrocatalysts for $CO_2$ reduction and their catalytic activity was demonstrated. The origin of activity towards $CO_2$ reduction in these materials was also explored. After demonstrating the superior catalytic activity of NCNTs towards the electrochemical reduction of $CO_2$ in comparison to expensive noble metals, i.e., Ag & Au, the role of precursors and growth temperatures on the defect structure and consequently the catalytic activity was studied systematically **(Chapter 3)**. Finally, to unravel the role of morphology on the catalytic activity of the NCNTs, N-doped graphene as electrocatalyst was investigated for $CO_2$ reduction **(Chapter 4)**.

## References

1. Lewis NS, Nocera DG. Powering the planet: Chemical challenges in solar energy utilization. *Proceedings of the National Academy of Sciences* **103**, 15729-15735 (2006).

2. Hansen J, *et al.* Ice melt, sea level rise and superstorms: evidence from paleoclimate data, climate modeling, and modern observations that 2 °C global warming is highly dangerous. *Atmos Chem Phys Discuss* **15**, 20059-20179 (2015).

3. McGlade C, Ekins P. The geographical distribution of fossil fuels unused when limiting global warming to 2 [deg]C. *Nature* **517**, 187-190 (2015).

4. Jenkinson DS, Adams DE, Wild A. Model estimates of $CO_2$ emissions from soil in response to global warming. *Nature* **351**, 304-306 (1991).

5. Norby RJ, Luo Y. Evaluating ecosystem responses to rising atmospheric $CO_2$ and global warming in a multi-factor world. *New Phytologist* **162**, 281-293 (2004).

6. Joos F, Plattner G-K, Stocker TF, Marchal O, Schmittner A. Global Warming and Marine Carbon Cycle Feedbacks on Future Atmospheric $CO_2$. *Science* **284**, 464-467 (1999).

7. Olah GA, Prakash GKS, Goeppert A. Anthropogenic Chemical Carbon Cycle for a Sustainable Future. *Journal of the American Chemical Society* **133**, 12881-12898 (2011).

8. Olah GA, Goeppert A, Prakash GKS. Chemical Recycling of Carbon Dioxide to Methanol and Dimethyl Ether: From Greenhouse Gas to Renewable, Environmentally Carbon Neutral Fuels and Synthetic Hydrocarbons. *The Journal of Organic Chemistry* **74**, 487-498 (2009).

9. Lackner KS. A Guide to $CO_2$ Sequestration. *Science* **300**, 1677-1678 (2003).

10. Hori Y, Vayenas CG, White RE, Gamboa-Aldeco ME. *Modern Aspects of Electrochemistry* (2008).

11. Gattrell M, Gupta N, Co A. *J Electroanal Chem* **594**, 1 (2006).

12. Jhong H-RM, Ma S, Kenis PJA. Electrochemical conversion of $CO_2$ to useful chemicals: current status, remaining challenges, and future opportunities. *Current Opinion in Chemical Engineering* **2**, 191-199 (2013).

13. Qiao J, Liu Y, Hong F, Zhang J. A review of catalysts for the electroreduction of carbon dioxide to produce low-carbon fuels. *Chemical Society Reviews* **43**, 631-675 (2014).

14. Delacourt C, Ridgway PL, Kerr JB, Newman J. Design of an Electrochemical Cell Making Syngas ( $CO + H_2$ ) from $CO_2$ and $H_2O$ Reduction at Room Temperature. *Journal of The Electrochemical Society* **155**, B42-B49 (2008).

15. Ebbesen SD, Mogensen M. Electrolysis of carbon dioxide in Solid Oxide Electrolysis Cells. *Journal of Power Sources* **193**, 349-358 (2009).

16. Kuhl KP, Cave ER, Abram DN, Jaramillo TF. New insights into the electrochemical reduction of carbon dioxide on metallic copper surfaces. *Energy & Environmental Science* **5**, 7050-7059 (2012).

17. Wu J, Risalvato FG, Sharma PP, Pellechia PJ, Ke F-S, Zhou X-D. Electrochemical Reduction of Carbon Dioxide: II. Design, Assembly, and Performance of Low Temperature Full Electrochemical Cells. *Journal of The Electrochemical Society* **160**, F953-F957 (2013).

18. Li CW, Kanan MW. $CO_2$ Reduction at Low Overpotential on Cu Electrodes Resulting from the Reduction of Thick $Cu_2O$ Films. *Journal of the American Chemical Society* **134**, 7231-7234 (2012).

19. Chen Y, Li CW, Kanan MW. Aqueous $CO_2$ Reduction at Very Low Overpotential on Oxide-Derived Au Nanoparticles. *Journal of the American Chemical Society* **134**, 19969-19972 (2012).

20. Chen Y, Kanan MW. Tin Oxide Dependence of the $CO_2$ Reduction Efficiency on Tin Electrodes and Enhanced Activity for Tin/Tin Oxide Thin-Film Catalysts. *Journal of the American Chemical Society* **134**, 1986-1989 (2012).

21. Chaplin RPS, Wragg AA. Effects of process conditions and electrode material on reaction pathways for carbon dioxide electroreduction with particular reference to formate formation. *J Appl Electrochem* **33**, 1107-1123 (2003).

22. Kortlever R, Shen J, Schouten KJP, Calle-Vallejo F, Koper MTM. Catalysts and Reaction Pathways for the Electrochemical Reduction of Carbon Dioxide. *The Journal of Physical Chemistry Letters* **6**, 4073-4082 (2015).

23. Studt F, *et al.* Discovery of a Ni-Ga catalyst for carbon dioxide reduction to methanol. *Nat Chem* **6**, 320-324 (2014).

24. Kumar B, *et al.* New trends in the development of heterogeneous catalysts for electrochemical $CO_2$ reduction. *Catalysis Today*.

25. Lim RJ, *et al.* A review on the electrochemical reduction of $CO_2$ in fuel cells, metal electrodes and molecular catalysts. *Catalysis Today* **233**, 169-180 (2014).

26. Jones J-P, Prakash GKS, Olah GA. Electrochemical $CO_2$ Reduction: Recent Advances and Current Trends. *Israel Journal of Chemistry* **54**, 1451-1466 (2014).

27. Shen J, *et al.* Electrocatalytic reduction of carbon dioxide to carbon monoxide and methane at an immobilized cobalt protoporphyrin. *Nat Commun* **6**, (2015).

28. Schneider J, Jia H, Muckerman JT, Fujita E. Thermodynamics and kinetics of $CO_2$, CO, and H+ binding to the metal centre of $CO_2$ reductioncatalysts. *Chemical Society Reviews* **41**, 2036-2051 (2012).

29. Zhang S, Kang P, Meyer TJ. Nanostructured Tin Catalysts for Selective Electrochemical Reduction of Carbon Dioxide to Formate. *Journal of the American Chemical Society* **136**, 1734-1737 (2014).

30. Choi SY, Jeong SK, Kim HJ, Baek I-H, Park KT. Electrochemical Reduction of Carbon Dioxide to Formate on Tin–Lead Alloys. *ACS Sustainable Chemistry & Engineering* **4**, 1311-1318 (2016).

31. Yadav RM, *et al.* Carbon Nitrogen Nanotubes as Efficient Bifunctional Electrocatalysts for Oxygen Reduction and Evolution Reactions. *ACS Applied Materials & Interfaces*, (2015).

32. Wu J, Sharma PP, Harris BH, Zhou X-D. Electrochemical reduction of carbon dioxide: IV dependence of the Faradaic efficiency and current density on the microstructure and thickness of tin electrode. *Journal of Power Sources* **258**, 189-194 (2014).

33. Wu J, Risalvato FG, Ma S, Zhou X-D. Electrochemical reduction of carbon dioxide III. The role of oxide layer thickness on the performance of Sn electrode in a full electrochemical cell. *Journal of Materials Chemistry A* **2**, 1647-1651 (2014).

34. Wu J, Risalvato FG, Ke F-S, Pellechia PJ, Zhou X-D. Electrochemical Reduction of Carbon Dioxide I. Effects of the Electrolyte on the Selectivity and Activity with Sn Electrode. *Journal of The Electrochemical Society* **159**, F353-F359 (2012).

35. Feng X, Jiang K, Fan S, Kanan MW. A Direct Grain-Boundary-Activity Correlation for CO Electroreduction on Cu Nanoparticles. *ACS Central Science* **2**, 169-174 (2016).

36. Verdaguer-Casadevall A, *et al.* Probing the Active Surface Sites for CO Reduction on Oxide-Derived Copper Electrocatalysts. *Journal of the American Chemical Society* **137**, 9808-9811 (2015).

37. Li CW, Ciston J, Kanan MW. Electroreduction of carbon monoxide to liquid fuel on oxide-derived nanocrystalline copper. *Nature* **508**, 504-507 (2014).

38. Sen S, Liu D, Palmore GTR. Electrochemical Reduction of $CO_2$ at Copper Nanofoams. *ACS Catalysis* **4**, 3091-3095 (2014).

39. Kas R, Kortlever R, Milbrat A, Koper MTM, Mul G, Baltrusaitis J. Electrochemical $CO_2$ reduction on $Cu_2O$-derived copper nanoparticles: controlling the catalytic selectivity of hydrocarbons. *Physical Chemistry Chemical Physics* **16**, 12194-12201 (2014).

40. Durand WJ, Peterson AA, Studt F, Abild-Pedersen F, Nørskov JK. Structure effects on the energetics of the electrochemical reduction of $CO_2$ by copper surfaces. *Surface Science* **605**, 1354-1359 (2011).

41. Nie X, Esopi MR, Janik MJ, Asthagiri A. Selectivity of $CO_2$ Reduction on Copper Electrodes: The Role of the Kinetics of Elementary Steps. *Angewandte Chemie International Edition* **52**, 2459-2462 (2013).

42. Lu Q, *et al.* A selective and efficient electrocatalyst for carbon dioxide reduction. *Nat Commun* **5**, (2014).

43. Kas R, Kortlever R, Yılmaz H, Koper MTM, Mul G. Manipulating the Hydrocarbon Selectivity of Copper Nanoparticles in $CO_2$ Electroreduction by Process Conditions. *ChemElectroChem* **2**, 354-358 (2015).

44. Peterson AA, Abild-Pedersen F, Studt F, Rossmeisl J, Norskov JK. How copper catalyzes the electroreduction of carbon dioxide into hydrocarbon fuels. *Energy & Environmental Science* **3**, 1311-1315 (2010).

45. Xie J-F, Huang Y-X, Li W-W, Song X-N, Xiong L, Yu H-Q. Efficient electrochemical $CO_2$ reduction on a unique chrysanthemum-like Cu nanoflower electrode and direct observation of carbon deposite. *Electrochimica Acta* **139**, 137-144 (2014).

46. Nursanto EB*, et al.* Gold catalyst reactivity for $CO_2$ electro-reduction: From nano particle to layer. *Catalysis Today*.

47. Won DH, Choi CH, Chung J, Chung MW, Kim E-H, Woo SI. Rational Design of a Hierarchical Tin Dendrite Electrode for Efficient Electrochemical Reduction of $CO_2$. *ChemSusChem* **8**, 3092-3098 (2015).

48. Kumar B*, et al.* Renewable and metal-free carbon nanofibre catalysts for carbon dioxide reduction. *Nat Commun* **4**, (2013).

49. Zhang S, *et al.* Polyethylenimine-Enhanced Electrocatalytic Reduction of $CO_2$ to Formate at Nitrogen-Doped Carbon Nanomaterials. *Journal of the American Chemical Society* **136**, 7845-7848 (2014).

50. Jitaru M, Lowy DA, Toma M, Toma BC, Oniciu L. Electrochemical reduction of carbon dioxide on flat metallic cathodes. *J Appl Electrochem* **27**, 875-889.

51. Ohta K, Kawamoto M, Mizuno T, Lowy AD. Electrochemical reduction of carbon dioxide in methanol at ambient temperature and pressure. *J Appl Electrochem* **28**, 717-724.

52. Hori Y, Murata A, Takahashi R. Formation of hydrocarbons in the electrochemical reduction of carbon dioxide at a copper electrode in aqueous solution. *Journal of the Chemical Society, Faraday Transactions 1: Physical Chemistry in Condensed Phases* **85**, 2309-2326 (1989).

53. Ikeda S, Takagi T, Ito K. Selective Formation of Formic Acid, Oxalic Acid, and Carbon Monoxide by Electrochemical Reduction of Carbon Dioxide. *Bulletin of the Chemical Society of Japan* **60**, 2517-2522 (1987).

54. Kaneco S, Iiba K, Ohta K, Mizuno T. Electrochemical reduction of carbon dioxide on copper in methanol with various potassium supporting electrolytes at low temperature. *J Solid State Electrochem* **3**, 424-428.

55. Podlovchenko BI, Kolyadko EA, Lu S. Electroreduction of carbon dioxide on palladium electrodes at potentials higher than the reversible hydrogen potential. *Journal of Electroanalytical Chemistry* **373**, 185-187 (1994).

56. Azuma M, Hashimoto K, Hiramoto M, Watanabe M, Sakata T. Electrochemical Reduction of Carbon Dioxide on Various Metal Electrodes in Low-Temperature Aqueous $KHCO_3$ Media. *Journal of The Electrochemical Society* **137**, 1772-1778 (1990).

57. Schrebler R, Cury P, Herrera F, Gómez H, Córdova R. Study of the electrochemical reduction of $CO_2$ on electrodeposited rhenium electrodes in methanol media. *Journal of Electroanalytical Chemistry* **516**, 23-30 (2001).

58. Ohmori T, Nakayama A, Mametsuka H, Suzuki E. Influence of sputtering parameters on electrochemical $CO_2$ reduction in sputtered Au electrode. *Journal of Electroanalytical Chemistry* **514**, 51-55 (2001).

59. Rosen BA, *et al.* Ionic Liquid–Mediated Selective Conversion of $CO_2$ to CO at Low Overpotentials. *Science* **334**, 643-644 (2011).

# Chapter 2

# Achieving Highly Efficient, Selective and Stable $CO_2$ Reduction on Nitrogen-doped Carbon Nanotubes

## 2.1 Introduction

Mastery of the electrochemical conversion of carbon dioxide and water to fuels using renewable electricity has the potential to shed light on understanding the nature of artificial photosynthesis and offer an approach to mitigate the negative impact of anthropogenic carbon dioxide emissions on the planet.[1, 2, 3, 4] The field, however, has not substantially advanced in the last 30 years primarily because of the challenge of discovery of chemically active and structurally stable electrocatalysts and membrane architectures. An ideal catalyst for the electroreduction of $CO_2$, e.g. $CO_2 + 2H^+ + 2e^- \rightarrow CO + H_2O$, is capable of mediating proton-coupled electron transfer, possessing a low overpotential for $CO_2$ activation while being sluggish towards hydrogen evolution, exhibiting a preferable selectivity towards a target product, and retaining structural integrity over a long operation. Significant progress has been made since 2011,[2, 5, 6] addressing the chemical activity originated from oxide scale or tuned ionic-liquid/catalyst interfaces. Silver and gold can selectively convert $CO_2$ to CO, a feedstock for the synthesis of methanol in the Fischer-Tropsch process,[1, 5] while the ionic liquid can function as a co-catalyst to lower the overpotential and subsequently improve the reaction kinetics. Copper and tin are known non-precious metallic catalysts. Copper is found to be active towards the formation of hydrogen carbon and alcohols.[7, 8, 9, 10] Tin exhibits a superior selectivity towards the formation of formate with a Faradaic efficiency up to 98%.[3] A rapid performance degradation was observed in both Sn- and Cu-based electrode after approximately 1 h from the start of $CO_2$ electrolysis.[11, 12, 13, 14] As a result, it is compelling to search for efficient, durable and inexpensive alternatives to metal electrocatalysts for $CO_2$ conversion.

Nitrogen-doped carbon nanotubes (NCNTs) are known to be an effective electrocatalyst for oxygen reduction. The activity of NCNT catalyst is originated from its both local defects that mediate the electronic structure,[15, 16] and its surface morphology that regulates atomic arrangement and coordination.[16] So far there are very limited reports on the use of CNTs or NCNTs as the catalyst for the electroreduction of $CO_2$. CNTs have been applied as the support for the catalytically active species rather than a catalyst itself.[17, 18] NCNTs with a modification of polyethyleneimine was ever found to function as a catalyst to reduce $CO_2$ to formate but at a high overpotential.[19] The activity of NCNTs towards the reduction of $CO_2$ remains largely unknown. The aim of this chapter is to report the recent investigation on the use of NCNTs as the catalysts for the direct conversion of $CO_2$ to fuel with an unprecedented low overpotential (0.18 V), high selectivity (80%), and durability.

## 2.2 Experimental Methods

**Material Synthesis:** The NCNTs were synthesized by liquid chemical vapor deposition (CVD) method injecting liquid precursor acetonitrile with ferrocene in $Ar/H_2$ atmosphere at 850 $^{o}$C. The concentration of ferrocene in precursors kept at 5 mg $ml^{-1}$.

The quartz tube with diameter 5 cm and length 1 m was placed in a three zone horizontal furnace with the heating zone of 81 cm. The furnace was heated to desired temperature from the room temperature under the argon ambience. When the optimum temperature reached, the precursors were injected by the syringe pump in the quartz tube with the flow rate of 12 ml $hr^{-1}$ in $Ar/H_2$ (80:20) atmosphere with a flow rate of 1000 SCCM. After the experiment the furnace was cooled down in Ar atmosphere. The pristine CNT arrays were synthesized by injecting benzene and ferrocene solution under similar growth conditions to NCNTs. The details about the experimental procedure are given elsewhere.[20, 21] $KHCO_3$ (99.7%), Nafion perfluorinated resin solution (5 wt.%) and isopropanol (99.5%) were purchased from Sigma-Aldrich; hydrogen (99.999%), argon (99.999%), helium (99.999%), and carbon dioxide (99.999%) were purchased from Airgas; Nafion 212 membrane was purchased from Dupont; Pt/C (60%) was obtained from Johnson Matthey; Ag powder (APS 20- 40 nm), Au powder (ASP 500-800 nm), Cu powder (APS 200-300nm) and Zn powder (6 µm) were purchased from Alfa Aesar. The graphite gas diffusion layer (GDL 10 BC) was ordered from SGL group. All chemicals were used without further purification. Electrolyte solutions were prepared with DI water (Siemens, Labstar).

**Catalyst Characterization:** The morphology of the materials were characterized by scanning electron microscope (SEM, FEI Quanta 400 FEG ESEM) and high resolution field emission gun transmission electron microscope (TEM, JEOL 2100 FEG TEM). The crystallinity was measured by powder X-ray diffraction (XRD) collected by Rigaku D/Max Ultima II. The microstructure was studied by Raman spectra using Renishaw inVia Raman microscope with 514 nm laser excitation. The chemical composition was investigated by X-ray photoelectron spectroscopy (XPS, PHI Quantera XPS) on PHI-5000C ESCA system with Al Ka x-ray as an excitation source.

**Electrochemical Measurements:** The N-doped carbon nanotubes (NCNTs) gas diffusion electrodes (NCNTs GDEs) were prepared from the NCNT arrays. In short, a suspension of NCNTs array particles and Nafion perfluorinated resin solution along with a 50/50 mixture of water and isopropanol were formed by ultrasonicating for at least 30 min before being sprayed onto GDLs to form GDEs with a NCNTs loading of 0.3~0.5 mg $cm^{-2}$. The NCNTs GDEs were then heat-treated at 130 °C for 30 min in the vacuum oven and allowed to cool slowly back to room temperature before testing. The other metals (Cu, Zn, Au and Ag) based GDEs followed the same preparation procedure and their loadings were ~ 1.5 mg $cm^{-2}$. The anode, Pt GDE, with a Pt loading of 0.3 mg $cm^{-2}$ was made as the similar procedure as NCNTs GDE. The Pt GDE was hot-pressed at 130 °C and 50 PSI for 5 min with a Nafion 212 membrane which prevents CO diffusing to Pt anode. The geometric surface area of GDE was 3.8 $cm^2$. The electrochemical test was carried out in a custom-designed full electrochemical cell with NCNTs GDE as the cathode electrode, Pt GDE as the anode electrode and 0.1 M $KHCO_3$ as the electrolyte. The cell runs at room temperature and ambient pressure. The cyclic voltammetry was carried out in the potential range of 0.15 ~ -1.0 V. The $CO_2$ reduction was conducted under potentiostatic mode for 30 min at each potential by employing potentiostat/galvanostat (Solartron 1470E). All the cell potentials were corrected by the IR drop. The ohmic resistance of the full electrochemical cell was measured from the electrochemical impedance spectroscopy at open circuit voltage, with an amplitude of 5 mV and frequency range from 100 kHz to 0.1 Hz.

**Product Quantification:** Gas products from the outlet of the cathodic compartment were vented directly into the gas-sampling loop of the gas chromatography (GC, Inficon Micro 3000 GC). A GC run was initiated every 10 minutes. The gas concentration was averaged over three measurements. Liquid products were identified using 1D $^1H$ nuclear magnetic resonance (NMR) spectroscopy (Varian Mercury/VX 400 MHz spectrometer) using the WET solvent suppression pulse sequence. The sodium 3-(trimethylsilyl) propionate 2, 2, 3, 3-d (4) (TSP) was used as the internal standard to quantify the liquid product concentration.

## 2.3 Results & Discussion

**Structural Characterization:** The NCNTs were synthesized by liquid chemical vapor deposition (CVD) method injecting liquid precursor acetonitrile and dicyandiamide with ferrocene in $Ar/H_2$ atmosphere at 850 $^oC$. Spraying of the precursor solution leads to a homogeneous NCNT deposition along the heating zone inside the quartz tube. The SEM investigation reveals the formation of well aligned NCNT arrays (**Figures 2.1a & b**). TEM analysis explores the details of microstructure that the NCNTs are multiwalled with a bamboo- shaped morphology due to nitrogen incorporation and free from amorphous and vitreous carbon (**Figure 2.1c & inset**). The electron energy loss spectroscopy (EELS) elemental mapping shows homogeneous N distribution in the single NCNT (**Figure 2.1d**). In addition to morphology the structural characterizations were performed by XRD and Raman spectroscopy. The sharpness of the (002) peak shows the high crystallinity and graphitic nature of NCNTs (**Figure 2.1e**). Raman spectrum shows a strong G-band at around 1584 $cm^{-1}$ and D-band at around 1355 $cm^{-1}$ (**Figure 2.1f**). The intensity ratio of the D to G modes ($I_d/I_g$) for the NCNTs is 0.87, which increases as compared to that of pristine CNT ($I_d/I_g = 0.58$) due to nitrogen incorporation.[27]

The doping of nitrogen in carbon nanotubes leads to local distortion in graphitic sheets due to differences in atomic masses and chemical bond lengths of carbon and nitrogen and thus responsible for increase in $I_d/I_g$ ratio for NCNTs as compared to pristine CNTs. The atomic configuration and stoichiometric composition of NCNTs were analyzed by XPS. The total N atomic content [N/(C+N)] in the NCNTs calculated from integrated peak area under C1s and N1s signal divided by their atomic sensitivity factor, comes around 5.0 at.%. The high resolution N1s spectra as shown in **Figure 2.1g** deconvolutes into sub-peaks at around 398.5, 400.8 and 401.5 eV, revealing three N configurations in the carbon $sp^2$ network corresponding to pyridinic, pyrrolic and graphitic N, respectively as shown in the schematic (**Figure 2.1i**). The graphitic N has the highest relative concentration followed by pyridinic and pyrrolic N. The individual atomic content for pyridinic, pyrrolic and graphitic N is 1.5 at.%, 1.1 at.% and 2.4 at.%, respectively (**Figure 2.1h**).

**Electrocatalytic Activity:** The activity of NCNTs towards the electrocatalytic reduction of $CO_2$ was evaluated in a full electrochemical cell employing a circulating electrolyte of 0.1 M $KHCO_3$ as shown in the previous work.[28] A catalyst ink was prepared from the NCNTs mixing with Nafion dispersion, isopropanol and deionized water and then sprayed onto carbon paper with a diffusion layer, to form a gas diffusion electrode (GDE). The NCNT GDE was inserted into the full electrochemical cell and served as the cathodic electrode for $CO_2$ reduction. The cyclic voltammetry (CV) curves of NCNTs acquired in Ar saturated 0.1 M $KHCO_3$ show the onset potential of -0.82 V for hydrogen

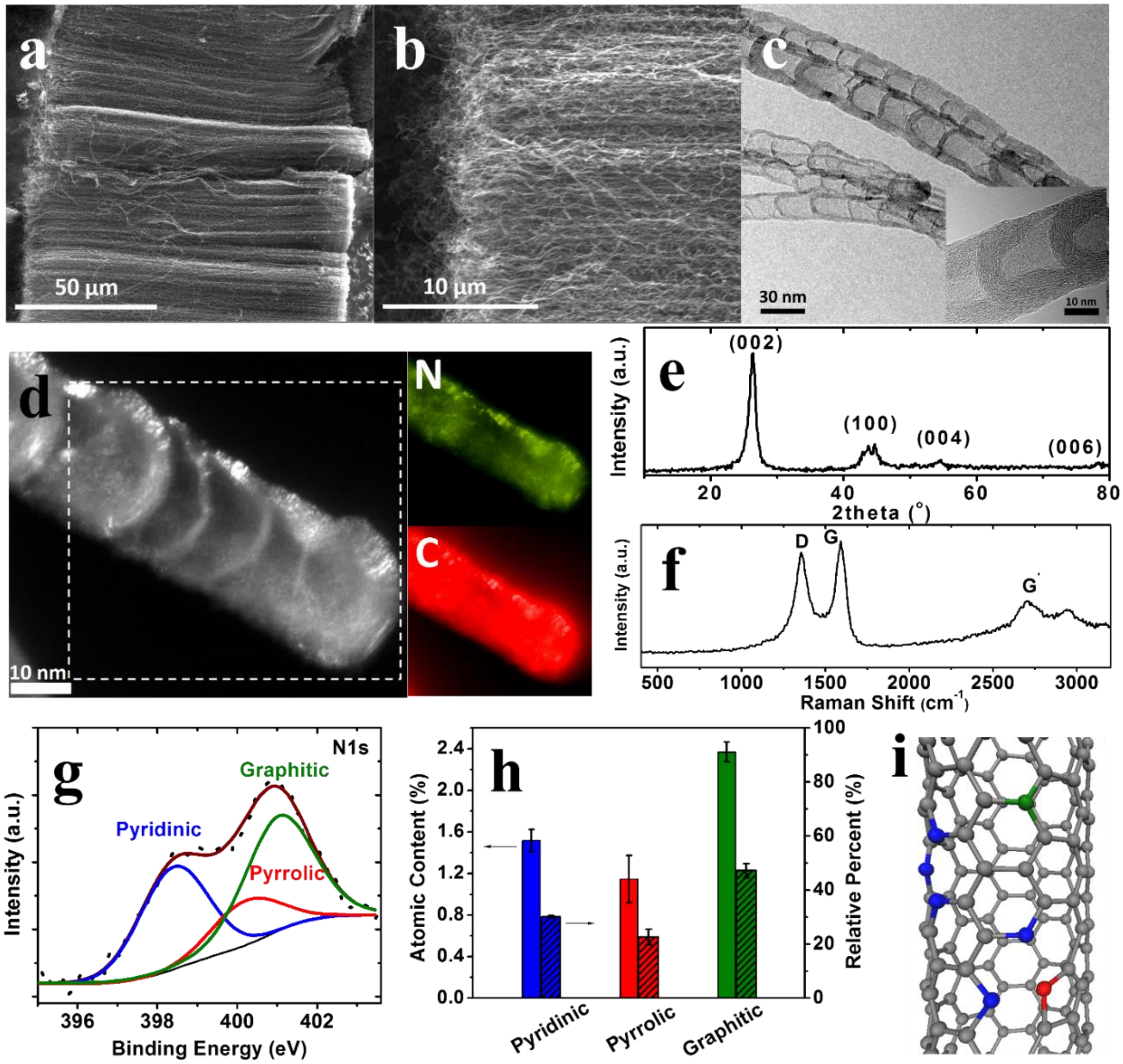

**Figure 2.1.** Physical characterization of NCNTs. (a) and (b) SEM images of NCNTs at low and high magnification, respectively. (c)TEM images of NCNTs, inset showing a single multi-wall NCNT. (d) EELS element mapping of N and C. (e) XRD pattern. (f) Raman spectrum. (g) A representative XPS of N 1s for NCNTs. The N1s is deconvoluted into three peaks representing three different N functionalities. (h) Statistic N atomic content and relative percent. (i) A schematic of graphitic, pyrrolic and pyridinic N configuration.

evolution reaction (HER) which indicates high overpotential (-0.41 V) with reference to the apparent standard cell potential (-0.41 V under pH = 7 for 0.1 M KOH) for HER (**Figure 2.6a**). The suppression of HER on NCNTs is beneficial for $CO_2$ reduction. When the gas supply is replaced with $CO_2$, the reduction current increased significantly.

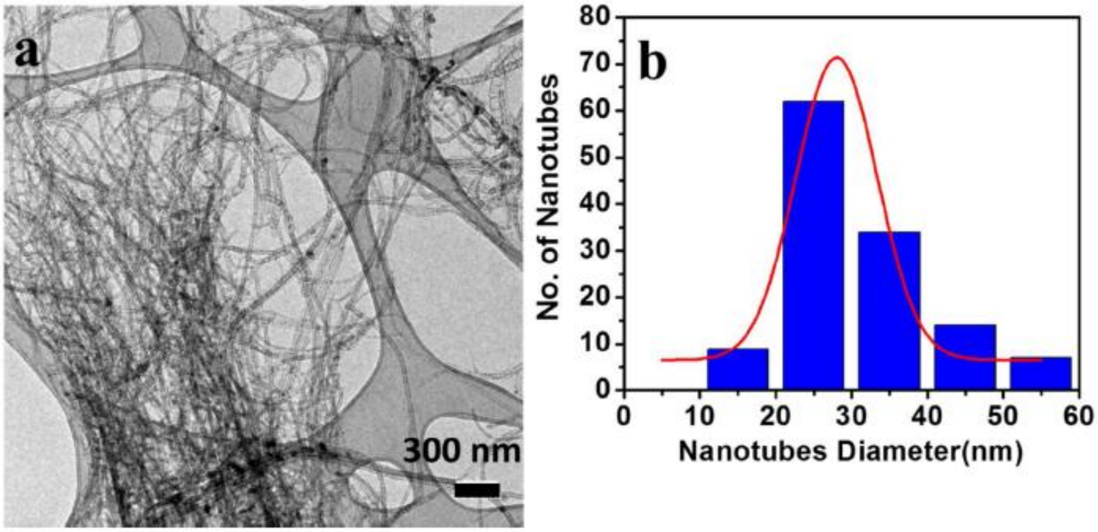

**Figure 2.2.** TEM characterization of NCNTs. (a) Low magnification images of NCNTs and (b) the corresponding tube diameter distribution

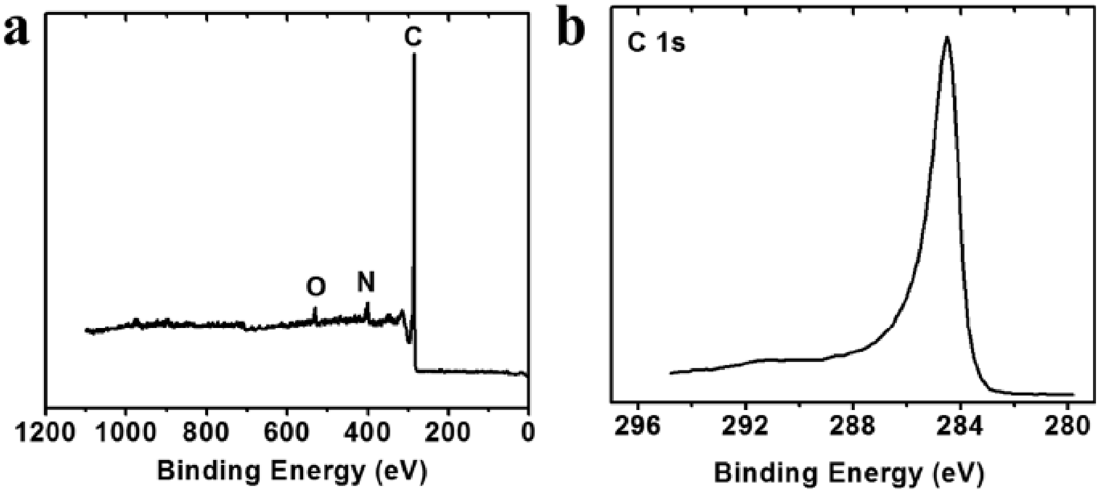

**Figure 2.3.** XPS characterization of NCNTs. (a) Survey scan of NCNTs showing C, N and O elements. (b) Fine scan of C 1s.

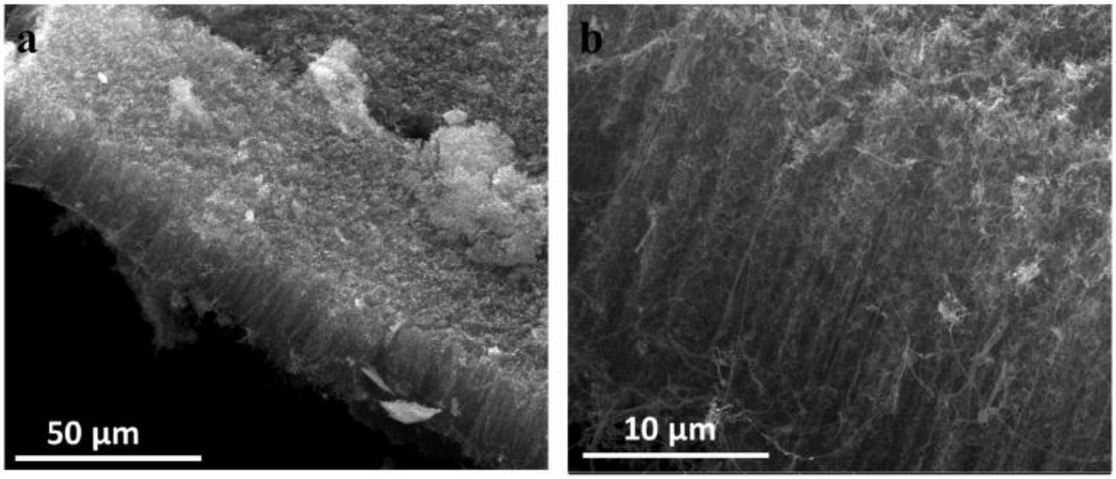

**Figure 2.4.** SEM images of pure CNTs. (a) A low magnification image showing the CNT arrays. (b) A high magnification image.

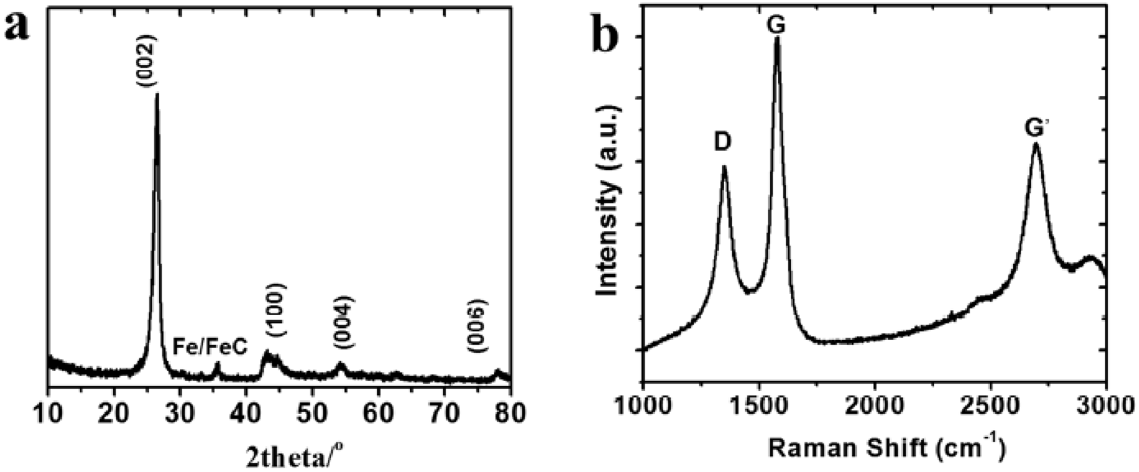

**Figure 2.5.** Microstructural characterization of pure CNTs. (a) XRD showing the same peak diffraction as NCNTs. A small diffraction peak assigned to iron species was observed. (b) Raman spectrum. The $I_D/I_G$ is 0.58.

This increment in reduction current indicates some $CO_2$ reduction reaction in addition to the HER. The change in reduction current, however, is not a conclusive evidence for $CO_2$ reduction since the hydrogen evolution and $CO_2$ reduction are often interconnected and $CO_2$ dissolving in the electrolyte will in turn lower the pH to further enhance the HER.

Consequently, the reduction products were monitored under potentiostatic electrolysis to further confirm the occurrence of $CO_2$ reduction. During the electrolysis of $CO_2$, the cathodic compartment of the cell was continuously purged with $CO_2$ gas and vented directly into the sampling loop of a GC to enable the quantification of the gas phase products. The liquid-phase products were measured by $^1$H NMR after electrolysis at each potential. NCNTs exhibit activity to the exclusive formation of CO while no liquid product is detected by NMR throughout the applied cell potential range. The CO starts to be formed with a Faradaic efficiency (FE) of 37% at an applied cell potential as low as -0.70 V which corresponds to an overpotential of -0.18 V with respect to the apparent standard cell potential of -0.52 V for $CO_2$ reduction to CO in the electrolyte of 0.1 M $KHCO_3$ (**Figure 2.6b**).[28] NCNTs display lower onset overpotential and higher correspondent FE of CO than that for Ag nanoparticles (-0.27 V with FE of CO 17%) and Au powder (-0.27 V with FE of CO 12%) under the identical testing conditions. This onset overpotential is also lower than that recently reported using carbon nanofibers (-0.23 V) mediated by ionic liquid of EMIM-$BF_4$.[29] The maximum FE of CO reaches around 80% at -0.78 V which also corresponds to a low overpotential of -0.26 V.

The achievable maximum FE of CO for NCNTs is comparable to that for Ag nanoparticles and Au powder; however, the overpotential to reach this highest FE of CO is far lower for NCNTs compared to noble metal Ag and Au catalysts, which means more energy efficient for NCNTs than Ag and Au. The least overpotential required for Ag and Au catalysts in the literatures was compared to reach the comparable FE of CO of around 80% with that of NCNTs (**Figure 2.9**). The overpotentials for the highest FE of CO for

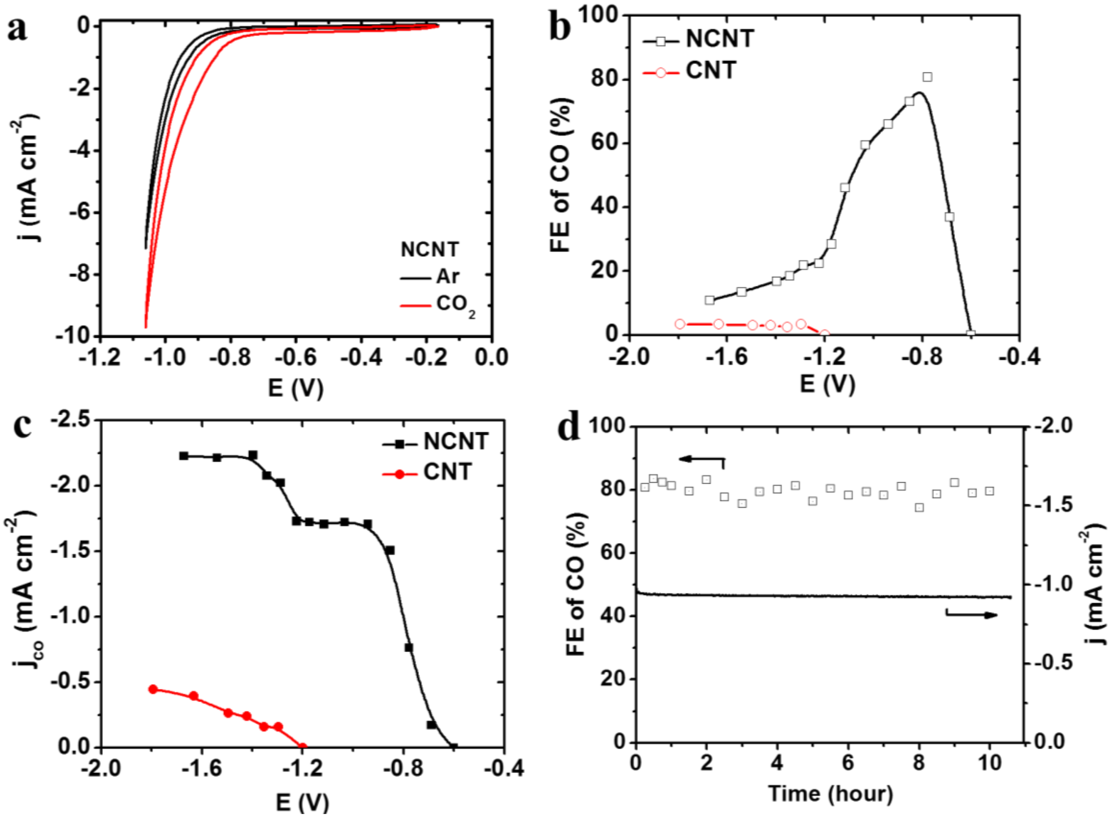

**Figure 2.6.** Performance of NCNTs for selectively electrochemical reduction of $CO_2$ to CO. (a) CVs for NCNTs in Ar and $CO_2$ saturated 0.1 M $KHCO_3$ electrolyte, 50 mV $s^{-1}$. (b) Dependence of FE of CO on applied cell potential during electrocatalysis of $CO_2$ reduction for both NCNTs and CNTs catalysts. (c) Partial current density of CO versus applied cell potential for NCNTs and CNTs catalysts. (d) Stability of performance of NCNTs for $CO_2$ reduction operated at potentiostatic mode of -0.8 V for 10 h. Both current density and FE of CO maintain steady over the duration of test.

metal catalysts such as Sn, Zn and Cu are also included in the **Figure 2.9** for comparison. To reach 80% FE of CO, NCNTs show much lower overpotential than most of the Ag and Au electrodes except oxide-derived Au nanoparticles and ionic liquid mediated Ag powder.[1, 5] These two cases are distinct from conventional polycrystalline metal catalysts with aqueous electrolyte. Oxide derived Au electrode comprised of 20-40 nm Au nanoparticles exhibits enhanced $CO_2$ reduction activity compared to polycrystalline Au electrode possibly due to the presence of highly active sites on its grain boundary surfaces as similar as oxide derived Cu electrodes.[30] The enhancement of activity for Ag powder is attributed to the presence of ionic liquid 1-ethyl-3- methylimidazolium tetrafluoroborate (EMIM-$BF_4$) that complexes with the $(CO_2)^-$ intermediate to lower the initial reduction barrier.[5]

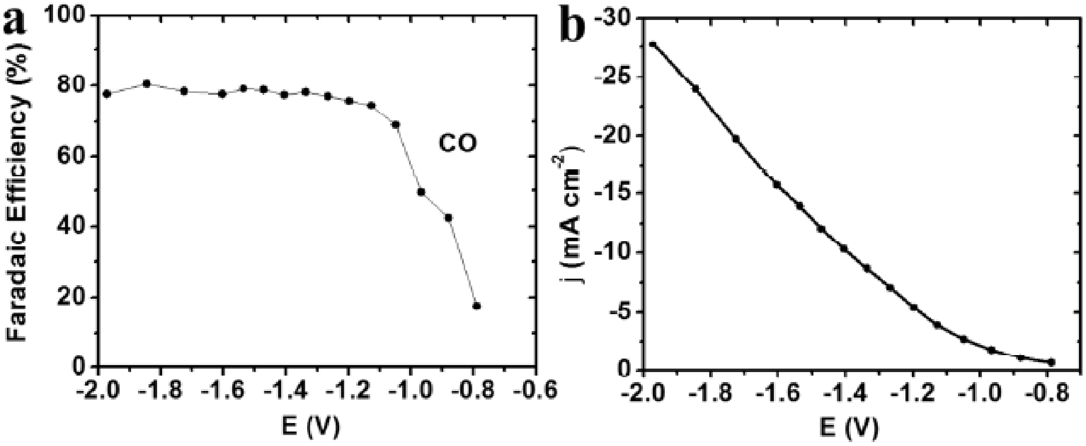

**Figure 2.7.** Electrochemical activity of Ag nanoparticles for $CO_2$ reduction. (a) Faradaic efficiency for CO, and (b) total current density at each tested cell voltage.

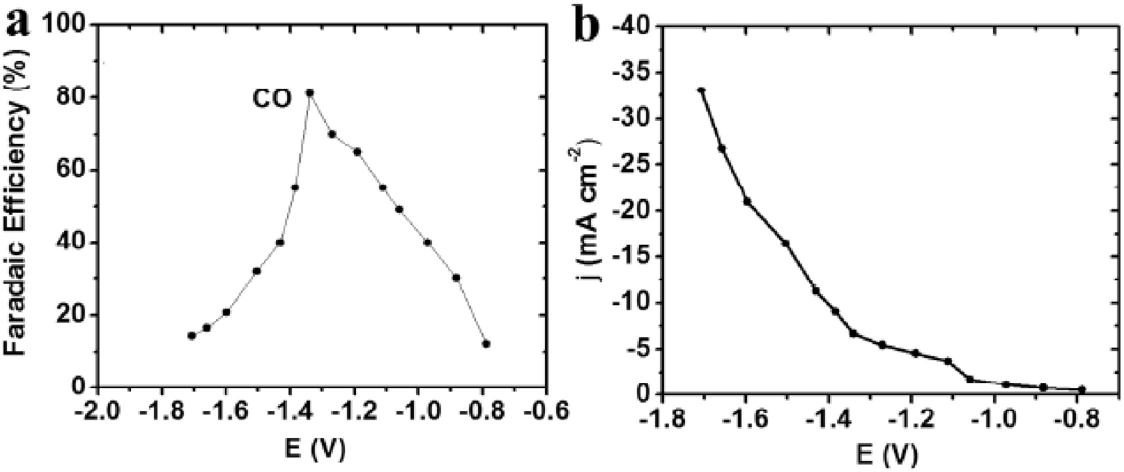

**Figure 2.8.** Electrochemical activity of Au powder for $CO_2$ reduction. (a) Faradaic efficiency of CO, and (b) total current density at each tested cell voltage.

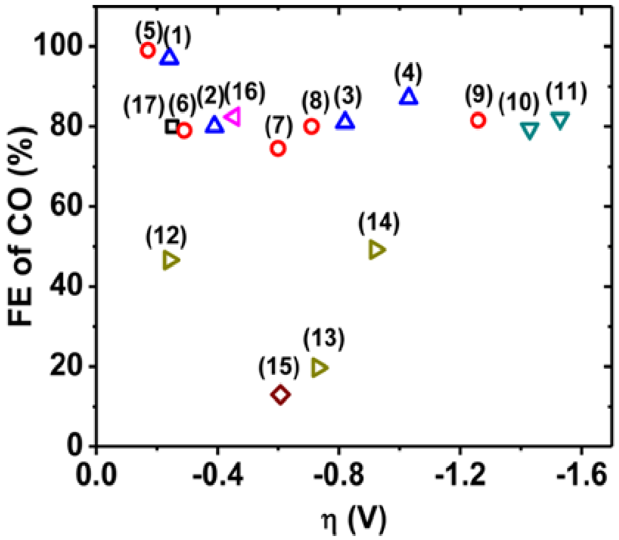

| No. | Symbol | Catalyst | Electrolyte |
|---|---|---|---|
| 1 | △ | Oxide-derived Au | 0.5 $NaKCO_3$ |
| 2 | △ | Polycrystalline Au foil | 0.5 $NaKCO_3$ |
| 3 | △ | Au powder (800 nm) | 0.1 $KHCO_3$ |
| 4 | △ | Polycrystalline Au foil | 0.1 $KHCO_3$ |
| 5 | ○ | Ag powder (100 nm) | EMIMBF4 |
| 6 | ○ | Nanoporous Ag | 0.5 $KHCO_3$ |
| 7 | ○ | Ag particles (20-40 nm) | 0.1 $KHCO_3$ |
| 8 | ○ | Ag powder (1 μm) | 0.1 $KHCO_3$ |
| 9 | ○ | Polycrystalline Ag foil | 0.1 $KHCO_3$ |
| 10 | ▽ | Zn powder (100 nm) | 0.1 $KHCO_3$ |
| 11 | ▽ | Polycrystalline Zn foil | 0.1 $KHCO_3$ |
| 12 | ▷ | Oxide-derived Cu | 0.5 $NaHCO_3$ |
| 13 | ▷ | Polycrystalline Cu foil | 0.5 $NaHCO_3$ |
| 14 | ▷ | Cu powder (200-300 nm) | 0.1 $KHCO_3$ |
| 15 | ◇ | Sn powder (100 nm) | 0.1 $KHCO_3$ |
| 16 | ◁ | $MoS_2$ powder | $EMIMBF_4$ |
| 17 | □ | NCNTs | 0.1 $KHCO_3$ |

**Figure 2.9.** Comparison of overpotential and yield of CO of NCNTs with metal catalysts. For Au, Ag, and $MoS_2$ catalyst, the lowest overpotential is chosen to reach a comparable FE of CO of around 80%. For Zn, Cu, and Sn catalyst, the overpotential for the maximum FE of CO is used.

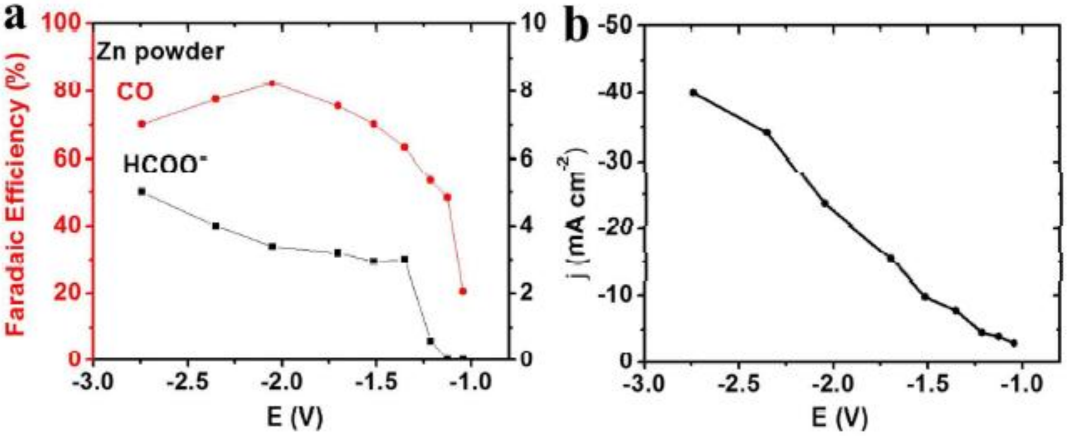

**Figure 2.10.** Electrochemical activity of Zn powder for $CO_2$ reduction. (a) Faradaic efficiency of CO and formate, and (b) total current density at each tested cell voltage.

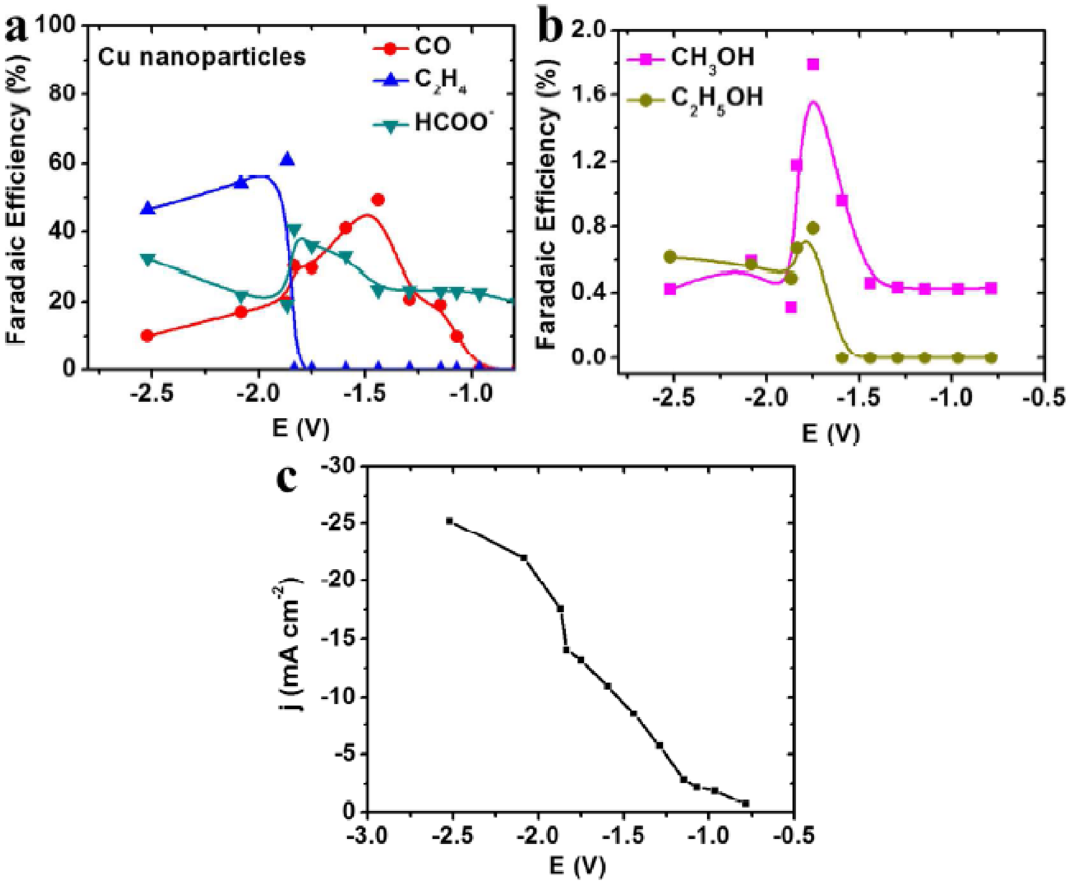

**Figure 2.11.** Electrochemical activity of Cu nanoparticles for $CO_2$ reduction. (a) Faradaic efficiency for CO, formate and $C_2H_4$, (b) Faradaic efficiency for $CH_3OH$ and $C_2H_5OH$, and (b) total current density at each tested cell voltage.

As a benchmark, $CO_2$ reduction was also performed on pristine CNT arrays. These CNTs show poor activity towards $CO_2$ reduction. The formation of CO starts at a cell potential of -1.38 V that is more negative than that for NCNTs. Moreover, the FE of CO is around 3.5% at this potential, much lower than that for NCNTs (**Figure 2.6b**). In addition to CO, formate is detected for $CO_2$ reduction on CNTs but has a low yield as similar as CO with a FE around 2.0-3.5% in the applied potential range of -1.38 ~ -2.10 V. The effect of trace metal (i.e. Fe in this case) on the catalytic activity towards ORR is an issue under debate. Actually, Fe has been proven to have no activity towards $CO_2$ reduction, resulting in $H_2$ evolution of ~100% in Faradaic efficiency.[31] The CNTs sample containing relatively higher Fe residuals than NCNTs were chosen intentionally, as evidenced by the higher current density of Fe residual redox peaks in the CV performed in a glassy carbon electrode (**Figure 2.12**). The much lower activity of CNTs than NCNTs suggests the active sites are mainly attributed to N-doping rather than the Fe residuals.

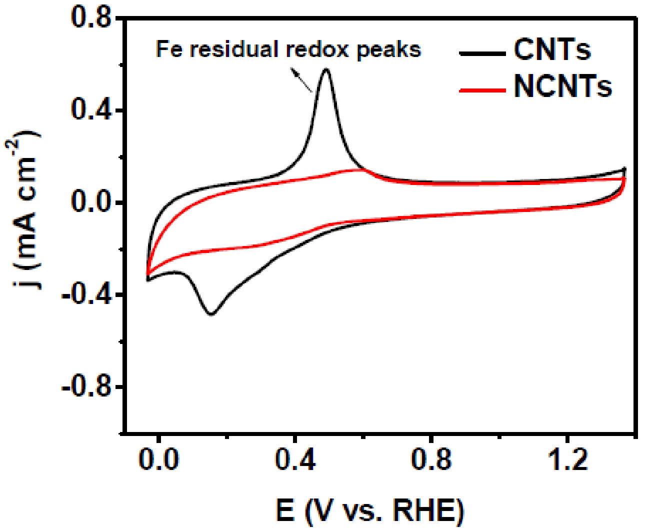

**Figure 2.12.** Cyclic voltammetry of NCNTs and CNTs in the electrolyte of 0.1 M KOH saturated with Ar. Scan rate: 50 mV/s.

Partial current density for CO production ($j_{CO}$) as a function of potential was extracted from data for the constant potential electrolyses (**Figure 2.6c**). The $j_{CO}$ for NCNTs is one order of magnitude higher than that for CNTs. The huge difference in activity between CNTs and NCNTs indicates the significant role of N dopant playing in the electrocatalysis process. The $CO_2$ reduction kinetics is facilitated as the cell potential sweeps cathodically leading to the increase of $j_{CO}$ for NCNTs. The $j_{CO}$ for NCNTs undergoes a plateau as the cell potential shifts more negatively beyond overpotential -0.41 V, reflecting mass transport limitation of $CO_2$ to the electrodes (**Figure 2.6c**). The FE of CO decreases after the achievement of mass transport limitation because more electrons are consumed by HER than $CO_2$ reduction reaction (**Figure 2.6b**).

**Post-electrolysis characterization:**

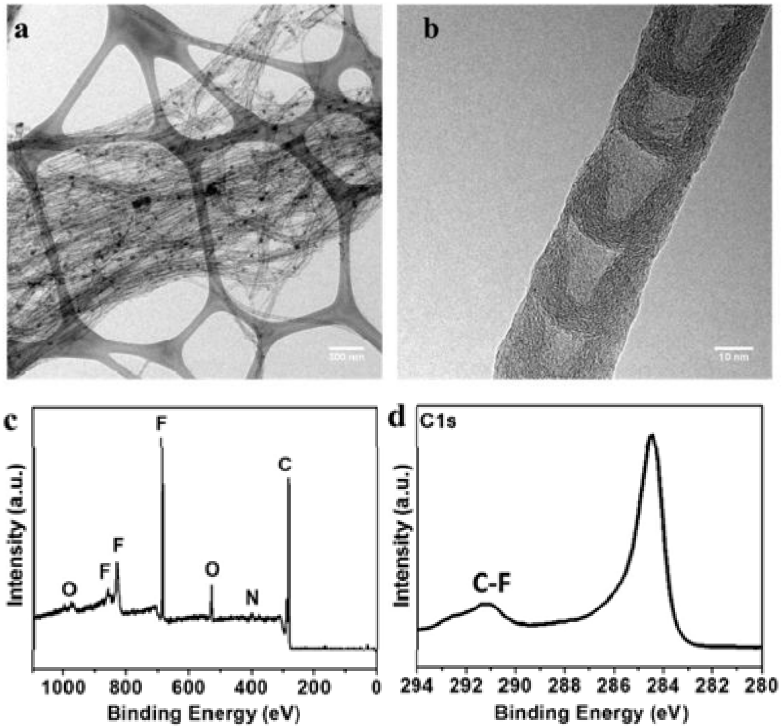

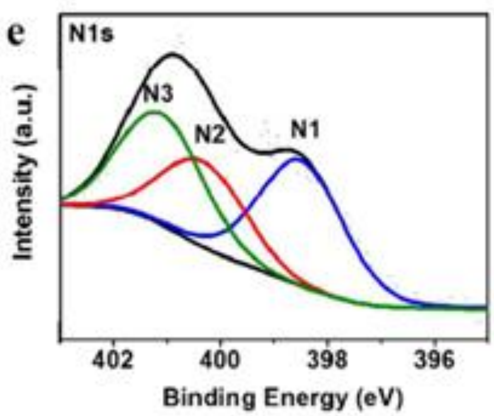

**Figure 2.13.** Physical characterization of NCNTs after long term operation. (a) Low magnification TEM images, (b) a high magnification TEM image of a single NCNT, (c) the survey spectrum of XPS, the F coming from the Nafion binder, (d) and (e) fine scans of C1s and N1s respectively.

The stability is equally important to the activity when developing catalysts for $CO_2$ reduction. Severe degradation occurs to the metal catalysts, like Cu and Au, and so far the mechanism is still obscure.[1, 2, 32] Thus, the long-term performance of NCNTs catalysts was tested at constant cell potential of -0.8 V for 10 hours. The current density maintains a steady value at around -1.0 mA $cm^{-2}$ throughout the duration of the test. Moreover, the FE of CO only fluctuates slightly around 80% over the test duration. After the long-term running, the morphology was analyzed and surface chemistry of the NCNTs electrode. The NCNTs keep the bamboo morphology after electrolysis of 10 h. In the electrolyzed electrode, the respective concentration for pyridinic, pyrrolic and graphitic N is 1.4%, 1.3% and 2.0%, which falls into the statistic region of N composition for the fresh electrodes, showing the robustness of NCNTs electrodes under reduction condition (**Figure 2.13**). These results clearly reveal that NCNTs act as highly active and durable catalysts for the electrochemical conversion of $CO_2$ to CO.

**Mechanistic Insights:** In order to understand the mechanism of electrocatalytic $CO_2$ reduction to CO with such a superior activity for NCNTs in terms of high efficiency and selectivity, the following three questions are open to be answered. (1) Why does the pathway only produce CO, without any hydrocarbons and alcohols? (2) Why is such a small overpotential in electrocatalysis of $CO_2$ reduction to CO possible? (3) Why do the NCNTs reduce $CO_2$ to CO with high yield/Faradaic efficiency? A mechanism was proposed to address the above three questions based on computational hydrogen electrode (CHE) model [26] and density functional theory (DFT) simulations implemented in Vienna Ab-initio Simulation Package (VASP) [33]. The answers to these questions should also shed light on modification of carbon nanostructures to further improve the activity.

The reaction mechanism of electroreduction of $CO_2$ to CO was considered on pristine CNTs and NCNTs surface through the adsorbed intermediates COOH* and CO*. Similar intermediates have been proposed for the electroreduction of $CO_2$ on late transition metals like Au, Pt and Cu.[26, 34] The elemental reaction steps for the $CO_2$ electrocatalytic reduction to CO are shown in Eqs. (1-3).[34]

$$\mathrm{CO_2(g)} + * + \mathrm{H^+(aq)} + \mathrm{e^-} \leftrightarrow \mathrm{COOH}* \qquad (1)$$

$$\mathrm{COOH}* + \mathrm{H^+(aq)} + \mathrm{e^-} \leftrightarrow \mathrm{CO}* + \mathrm{H_2O(l)} \qquad (2)$$

$$\mathrm{CO}* \leftrightarrow \mathrm{CO(g)} + * \qquad (3)$$

where * denotes a free step site. This reaction mechanism involves two coupled electron-proton transfer reaction steps (Eq. 1 and 2) and one non-electrochemical step, CO desorption (Eq. 3). The overpotential strongly depends on free energies of the first two electrochemical steps. For NCNTs, the activation of $CO_2$ to form adsorbed COOH* is associated with an uphill process of the first electron-proton pair transfer at 0 V vs. RHE. After the adsorption of COOH, the free-energy pathway becomes thermodynamically downhill to transfer the second electron-proton pair to form adsorbed CO. This CO is weakly bound to NCNTs surface, leading to the production of CO gas. The potential-limiting step is the formation of adsorbed COOH*, requiring an onset potential of -0.30 V vs. RHE at which the step becomes exergonic (downhill in free energy) at the pyridinic N site. It implies an existence of limiting (least-negative) overpotential of -0.20 V which is close to the experimental observation as shown in **Figure 2.6b**. The calculated limiting overpotential for pyridinic N is lower than theoretical values for Cu (-0.31 V), Au (-0.63 V) and Ag (-0.79 V).[26, 35] The most efficient N configuration is pyridinic N followed by pyrrolic and graphitic N. In the case of CNTs, the potential-limiting step is also the formation of adsorbed COOH*, but requiring an overpotential of -1.9 V, much higher than that for NCNTs, which is in agreement with the experimental data as seen in **Figure 2.6b**.Moreover, in order to elucidate the high selectivity of NCNTs towards CO production, the kinetic activity towards CO production was correlated with the adsorption energies of COOH ($E_{B[COOH]}$) and CO ($E_{B[CO]}$).[34, 35] Essentially, a highly selective catalyst for $CO_2$ reduction to CO is required to possess the capability of immobilizing COOH but loosening CO at the same time. In other words, it requires strong COOH binding but a weak CO adsorption.

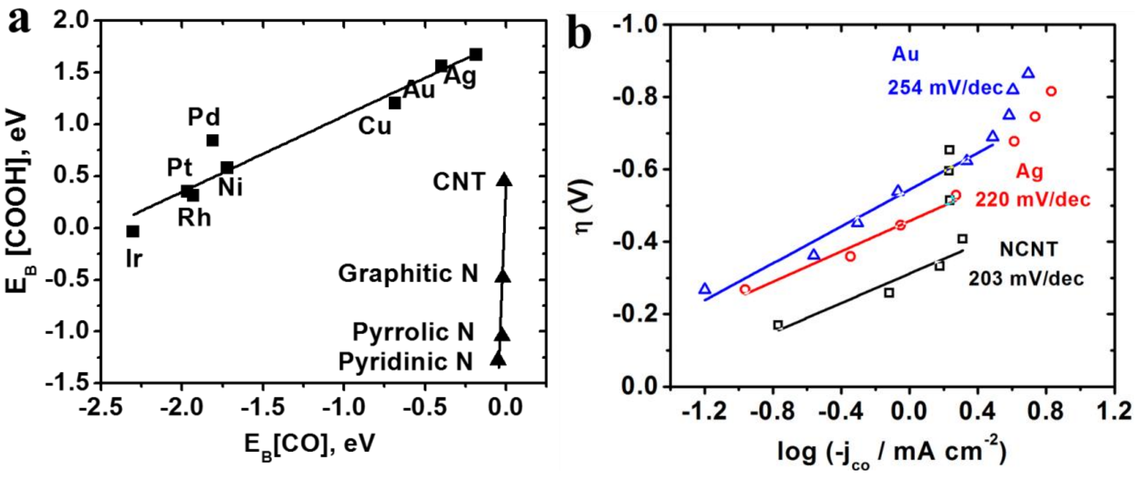

**Figure 2.14.** Kinetic activity of NCNTs and metal catalysts. (a) The correlation of calculated adsorption energies of the key bound intermediates of COOH* and CO*. The binding energy data for lattice surface (211) of metals are adopted from Ref. 35. DFT calculations were done by Mingjie Liu at Rice University. (b) The experimental Tafel plots of NCNTs, Au and Ag electrodes.

The $E_{B[COOH]}$ and $E_{B[CO]}$ for pristine and different N functionalities doped CNTs were calculated, and the results are shown in **Figure 2.14a**. The data of metal catalysts from ref. [35] are also included in Fig. 6a. For the elemental metal catalysts, the $E_{B[COOH]}$ and $E_{B[CO]}$ are linearly correlated with a small positive slope less than one (around 0.73), which suggests that increasing the bonding strength of COOH to the metal surface is accompanied by a sharp increase of CO adsorption energy. Therefore, all elemental metals are off the maximum of kinetic activity to electroreduce $CO_2$ to CO. For the CNTs materials, the $\Delta E_{COOH}$ versus $\Delta E_{CO}$ is also positively linear. However, the slope for the linear relationship has a much larger magnitude of around 37, and thus a significant increase of $E_{B[COOH]}$ only causes a slight increase of $E_{B[CO]}$ in NCNTs, which fulfills the essential requirement for highly selective catalysts for CO evolution. The binding energy profile indicates the highest selective site towards CO production is pyridinic N followed by pyrrolic and graphitic N.

**Table 2.1.** Kinetic data of NCNTs, Au and Ag for electroreduction of $CO_2$ to CO. $j_0$ denotes the exchange current density

| **Material** | **Tafel Slope (mV/dec)** | **$j_0$ (mA/cm$^2$)** |
|---|---|---|
| NCNTs | 203 | 2.9E-02 |
| Au powder | 254 | 7.3E-03 |
| Ag nanoparticles | 220 | 9.7E-03 |

The pyridinic N has very negative value of $E_{B[COOH]}$ as reactive metals like Pt and N so that COOH can bind tightly. On the other hand, it owns a weak $E_{B[CO]}$ similar with Au and Ag which renders the feasible desorption of adsorbed CO*. Both pyrrolic and graphitic N are also calculated to have stronger $E_{B[COOH]}$ and weaker $E_{B[CO]}$ than the most CO selective elemental metal catalysts like Au and Ag. As a result, gas product of CO is favorably produced on NCNTs instead of hydrocarbons and alcohols, as CO is released easily from active N sites on NCNTs before it can be further reduced by the successive electrons. The binding energy profile of COOH and CO for the three N configurations provides insight into the high FE of CO up to 80% for NCNTs in these measurements. For the CNTs, although the binding energy for both COOH and CO is reasonable for selective CO production, the free energy barrier for the first electron-proton pair transfer is too high resulting in a very high onset overpotential at which the HER is also promoted and predominates over $CO_2$ reduction. Therefore, CNTs exhibit a low yield of CO. In order to further verify the validation of the adsorption energy plot, a comparison of the kinetic data extracted from the Tafel plots, log($j_{CO}$) versus overpotential ($\eta$), was made among NCNTs, Au and Ag (**Figure 2.14b**). The NCNTs show the smallest Tafel slopes (~200 mV/dec) compared to Au and Ag in the low overpotential regime of -0.17 V to -0.41 V. Additionally, the NCNTs possess exchange current density for CO production, obtained from the extrapolation of the Tafel region to reversible potential, three times as big as Au and Ag. The experimental kinetic data match well with the theoretical prediction of superior activity of NCNTs towards CO formation over metals Au and Ag.

## 2.4 Conclusions

In summary, nitrogen doped carbon nanotube arrays with total N content of 5 at.% were synthesized by liquid CVD method. The NCNT array acts as highly active, selective and stable catalysts for electrocatalytic reduction of $CO_2$ to CO. Compared to noble metals Au and Ag, these NCNTs exhibit lower overpotentials to achieve the similar selectivity towards the production of CO. The maximum FE of CO reaches around 80% at a low overpotential of -0.26 V. As a contrast, pristine CNTs show poor activity and selectivity towards electroreduction of $CO_2$. The superior activity for NCNTs is mainly attributed to a low free energy barrier for the potential-limiting step to form adsorbed COOH. Moreover, the suitable binding energy of the key intermediates enables strong COOH adsorption and feasible CO desorption that contributes to the high selectivity towards CO formation. The economical NCNTs are proposed as successful alternatives to expensive noble metal electrocatalysts for commercial $CO_2$ reduction application, with the promise of more efficiency and higher selectivity.

## References

1. Chen Y, Li CW, Kanan MW. Aqueous $CO_2$ Reduction at Very Low Overpotential on Oxide-Derived Au Nanoparticles. *J Am Chem Soc* **134**, 19969-19972 (2012).

2. Li CW, Kanan MW. $CO_2$ Reduction at Low Overpotential on Cu Electrodes Resulting from the Reduction of Thick $Cu_2O$ Films. *J Am Chem Soc* **134**, 7231-7234 (2012).

3. Wu JJ, Risalvato FG, Ke FS, Pellechia PJ, Zhou XD. Electrochemical Reduction of Carbon Dioxide I. Effects of the Electrolyte on the Selectivity and Activity with Sn Electrode. *Journal of the Electrochemical Society* **159**, F353-F359 (2012).

4. Zhang S, Kang P, Meyer TJ. Nanostructured Tin Catalysts for Selective Electrochemical Reduction of Carbon Dioxide to Formate. *Journal of the American Chemical Society* **136**, 1734-1737 (2014).

5. Rosen BA, *et al.* Ionic Liquid–Mediated Selective Conversion of $CO_2$ to CO at Low Overpotentials. *Science* **334**, 643-644 (2011).

6. Chen Z, Kang P, Zhang M-T, Stoner BR, Meyer TJ. Cu(ii)/Cu(0) electrocatalyzed $CO_2$ and $H_2O$ splitting. *Energy & Environmental Science* **6**, 813-817 (2013).

7. Jermann B, Augustynski J. Long-term activation of the copper cathode in the course of $CO_2$ reduction. *Electrochimica Acta* **39**, 1891-1896 (1994).

8. Voiry D, *et al.* Conducting $MoS_2$ Nanosheets as Catalysts for Hydrogen Evolution Reaction. *Nano Lett* **13**, 6222-6227 (2013).

9. DeWulf DW, Jin T, Bard AJ. Electrochemical and Surface Studies of Carbon Dioxide Reduction to Methane and Ethylene at Copper Electrodes in Aqueous Solutions. *Journal of The Electrochemical Society* **136**, 1686-1691 (1989).

10. Fan MY, Bai ZY, Zhang Q, Ma CY, Zhou XD, Qiao JL. Aqueous $CO_2$ reduction on morphology controlled $Cu_xO$ nanocatalysts at low overpotential. *Rsc Advances* **4**, 44583-44591 (2014).

11. Kedzierzawski P, Augustynski J. Poisoning and Activation of the Gold Cathode During Electroreduction of $CO_2$. *Journal of the Electrochemical Society* **141**, L58-L60 (1994).

12. Delacourt C, Ridgway PL, Kerr JB, Newman J. Design of an electrochemical cell making syngas ($CO+H_2$) from $CO_2$ and $H_2O$ reduction at room temperature. *Journal of The Electrochemical Society* **155**, B42-B49 (2008).

13. Li H, Oloman C. The electro-reduction of carbon dioxide in a continuous reactor. *Journal of Applied Electrochemistry* **35**, 955-965 (2005).

14. Koleli F, Atilan T, Palamut N, Gizir AM, Aydin R, Hamann CH. Electrochemical reduction of $CO_2$ at Pb- and Sn-electrodes in a fixed-bed reactor in aqueous $K_2CO_3$ and $KHCO_3$ media. *Journal of Applied Electrochemistry* **33**, 447-450 (2003).

15. Gong K, Du F, Xia Z, Durstock M, Dai L. Nitrogen-Doped Carbon Nanotube Arrays with High Electrocatalytic Activity for Oxygen Reduction. *Science* **323**, 760-764 (2009).

16. Li Y*, et al.* An oxygen reduction electrocatalyst based on carbon nanotube-graphene complexes. *Nat Nano* **7**, 394-400 (2012).

17. Kang P, Zhang S, Meyer TJ, Brookhart M. Rapid Selective Electrocatalytic Reduction of Carbon Dioxide to Formate by an Iridium Pincer Catalyst Immobilized on Carbon Nanotube Electrodes. *Angewandte Chemie* **126**, 8853-8857 (2014).

18. Zhao H, Zhang Y, Zhao B, Chang Y, Li Z. Electrochemical Reduction of Carbon Dioxide in an MFC–MEC System with a Layer-by-Layer Self-Assembly Carbon Nanotube/Cobalt Phthalocyanine Modified Electrode. *Environmental Science & Technology* **46**, 5198-5204 (2012).

19. Zhang S*, et al.* Polyethylenimine-Enhanced Electrocatalytic Reduction of $CO_2$ to Formate at Nitrogen-Doped Carbon Nanomaterials. *J Am Chem Soc* **136**, 7845-7848 (2014).

20. Yadav R, Dobal P, Shripathi T, Katiyar R, Srivastava O. Effect of Growth Temperature on Bamboo-shaped Carbon-Nitrogen (C-N) Nanotubes Synthesized Using Ferrocene Acetonitrile Precursor. *Nanoscale Research Letters* **4**, 197 - 203 (2008).

21. Srivastava A, Srivastava ON, Talapatra S, Vajtai R, Ajayan PM. Carbon nanotube filters. *Nat Mater* **3**, 610-614 (2004).

22. Kresse G, Hafner J. \textit{Ab initio} molecular dynamics for liquid metals. *Physical Review B* **47**, 558-561 (1993).

23. Kresse G, Furthmüller J. Efficient iterative schemes for \textit{ab initio} total-energy calculations using a plane-wave basis set. *Physical Review B* **54**, 11169-11186 (1996).

24. Perdew JP, Burke K, Ernzerhof M. Generalized Gradient Approximation Made Simple. *Physical Review Letters* **77**, 3865-3868 (1996).

25. Nørskov JK, *et al.* Origin of the Overpotential for Oxygen Reduction at a Fuel-Cell Cathode. *The Journal of Physical Chemistry B* **108**, 17886-17892 (2004).

26. Peterson AA, Abild-Pedersen F, Studt F, Rossmeisl J, Norskov JK. How copper catalyzes the electroreduction of carbon dioxide into hydrocarbon fuels. *Energy & Environmental Science* **3**, 1311-1315 (2010).

27. Dresselhaus MS, Jorio A, Hofmann M, Dresselhaus G, Saito R. Perspectives on Carbon Nanotubes and Graphene Raman Spectroscopy. *Nano Lett* **10**, 751-758 (2010).

28. Wu J, Risalvato FG, Sharma PP, Pellechia PJ, Ke F-S, Zhou X-D. Electrochemical Reduction of Carbon Dioxide II. Design, Assembly, and Performance of Low Temperature Full Electrochemical Cells. *J Electrochem Soc* **160**, F953-F957 (2013).

29. Kumar B, *et al.* Renewable and metal-free carbon nanofibre catalysts for carbon dioxide reduction. *Nat Commun* **4**,  (2013).

30. Li CW, Ciston J, Kanan MW. Electroreduction of carbon monoxide to liquid fuel on oxide-derived nanocrystalline copper. *Nature* **508**, 504-507 (2014).

31. Azuma M, Hashimoto K, Hiramoto M, Watanabe M, Sakata T. Electrochemical Reduction of Carbon Dioxide on Various Metal Electrodes in Low-Temperature Aqueous $KHCO_3$ Media. *J Electrochem Soc* **137**, 1772-1778 (1990).

32. Hori Y, *et al.* "Deactivation of copper electrode" in electrochemical reduction of $CO_2$. *Electrochimica Acta* **50**, 5354-5369 (2005).

33. Kresse G, Furthmüller J. Efficient iterative schemes for ab initio total-energy calculations using a plane-wave basis set. *Phys Rev B* **54**, 11169-11186 (1996).

34. Hansen HA, Varley JB, Peterson AA, Nørskov JK. Understanding Trends in the Electrocatalytic Activity of Metals and Enzymes for $CO_2$ Reduction to CO. *J Phys Chem Lett* **4**, 388-392 (2013).

35. Peterson AA, Nørskov JK. Activity Descriptors for $CO_2$ Electroreduction to Methane on Transition-Metal Catalysts. *J Phys Chem Lett* **3**, 251-258 (2012).

# Chapter 3

# Nitrogen Doped Carbon Nanotube Arrays for High Efficiency Electrochemical Reduction of $CO_2$: On the Understanding of Defects, Defect Density, and Selectivity

## 3.1 Introduction

A recent report by an international team led by Pierre Friedlingstein[1] estimated that global $CO_2$ discharge from fossil fuel combustion and cement production would continuously rise in 2014 to a level of ~ 65% above emissions in 1990, the base year adopted in the Kyoto Protocol. Meanwhile, the daily mean concentration of carbon dioxide in the atmosphere measured at the Mauna Loa Observatory in Hawaii was recorded above 400 parts per million for the first time on May 9th, 2013. The rapid increase in the $CO_2$ in ambient air may cause irreversible damage, resulting in uninhabitable planet for future generations. A carbon neutral cycle, if realized, can potentially address these issues by capturing and converting $CO_2$ to various liquid or gaseous fuels when coupled together with renewable energy sources.[2, 3] The main hurdle for this technology is the availability of efficient and robust catalysts that can catalyze the multiple proton-electron transfer reactions involved in $CO_2$ reduction.[4] Presently, metallic electrocatalysts including Sn, Cu, Au, and Ag have been extensively investigated.

However, high overpotentials, poor stability, and inferior selectivity remain major challenges yet to be tackled.[5, 6, 7] Nitrogen-doped carbon nanotubes (NCNTs) have gained much attention as electrocatalysts for the oxygen reduction reaction (ORR) and oxygen evolution reaction (OER) because of their unique electronic[8] and geometric features.[8, 9, 10, 11, 12] The catalytic activity most likely originates from the nitrogen defects in the hexagonal graphitic network.[13, 14, 15] Unlike ORR, reports of the application of NCNTs as catalysts for the electrochemical reduction of $CO_2$ are limited. Direct conversion of $CO_2$ to CO using a nitrogen-doped carbon nanofiber catalyst [16] in an ionic liquid based environment were reported, with the ionic liquid acting as a possible co-catalyst[17]. In addition to the unknown reaction mechanism in doped carbon fibers, the high cost of ionic liquids makes this approach economically challenging. NCNTs have also been employed for $CO_2$ reduction to formate using polyethyleneimine as a co-catalyst, stabilizing the $CO_2^{-*}$ intermediate.[18] However, high overpotentials (> 0.6 V) were needed to catalyze this reaction. Recently, the superior catalytic activity of NCNTs to noble metal catalysts, including Ag and Au, towards CO formation was demonstrated.[19] Here, the extensive study on the role of different NCNT nitrogen functionalities, i.e., graphitic, pyridinic and pyrrolic nitrogen sites, on the direct conversion of $CO_2$ to CO without the use of a metal catalyst, is reported.

## 3.2 Experimental Methods

### Materials

$KHCO_3$ (99.7%), Nafion perfluorinated resin solution (5 wt.%) and isopropanol (99.5%) were purchased from Sigma-Aldrich; hydrogen (99.999%), argon (99.999%), helium (99.999%), and carbon dioxide (99.999%) were purchased from Airgas; Nafion® 212 membrane was purchased from DuPont; Pt/C (60%) was obtained from Johnson Matthey; the graphite gas diffusion layer (GDL 10 BC) was ordered from SGL group. All chemicals were used without further purification. Electrolyte solutions were prepared with DI water (Siemens, Labstar).

**N-doped Carbon Nanotubes (NCNTs) Synthesis & Characterization**

Liquid chemical vapor deposition technique was employed to synthesize NCNTs by injecting nitrogen containing hydrocarbons as C/N precursor and ferrocene as the C/Fe precursor at high temperatures (≥ 750°C) in quartz tube. Ar/$H_2$ atmosphere (80:20) with flow rate of 1000 SCCM was used for entire synthesis. A composition of 90 wt.% acetonitrile (ACN) and 10 wt.% dicyandiamide was used for synthesizing NCNTs with ACN precursor at various growth temperatures. The furnace was heated to desired temperature from room temperature under argon ambience. The precursor solution was injected at a rate of 12 ml/hr by a syringe pump in the quartz tube. The NCNT samples were collected after cooling the furnace in Ar atmosphere. The pristine CNT arrays were synthesized by injecting benzene and ferrocene solution under similar growth conditions to NCNTs. The details about the experimental procedure have been described elsewhere.[20, 21] The microstructure of the synthesized materials was characterized by scanning electron microscope (FEI Quanta 400 FEG ESEM) and high resolution field emission gun transmission electron microscope (JEOL 2100 FEG TEM). Raman spectra of the synthesized NCNTs were recorded using Renishaw inVia *Raman microscope with 514 nm laser excitation.* The surface composition and chemical bonding states of nitrogen in the as-synthesized NCNTs were investigated by X-ray photoelectron spectrometer (XPS, PHI Quantera XPS) on PHI-5000C ESCA system with Al $K_\alpha$ x-ray as an excitation source.

**Electrochemical Measurements & Product Quantification**

Gas diffusion electrodes (GDEs) of different carbon nanomaterials were prepared by spraying the catalyst ink over a carbon gas diffusion layer (GDL), as described in the previous reports.[22, 23] The geometric surface area of GDE was 3.8 $cm^2$. The loading of NCNTs was ~ 0.5 $mg/cm^2$. The electrochemical test was carried out in a custom-designed full electrochemical cell with NCNTs GDE as the cathode electrode, Pt GDE as the anode electrode and 0.1 M $KHCO_3$ as the electrolyte. The cell was tested at room temperature and ambient pressure conditions. The $CO_2$ reduction was conducted under potentiostatic mode for 30 min at each potential by employing potentiostat/galvanostat (Solartron 1470E). All the cell potentials were corrected by the iR drop. The ohmic resistance of the full electrochemical cell was measured from the electrochemical impedance spectroscopy at open circuit voltage, with an amplitude of 5 mV and frequency range from 100 kHz to 0.1 Hz. Gas products from the outlet of the cathodic compartment were vented directly into the gas-sampling loop of the gas chromatography (GC, Inficon Micro 3000 GC). A GC run was initiated every 10 minutes. The gas concentration was averaged over three measurements. Liquid products were indentified using 1D $^1H$ nuclear magnetic resonance (NMR) spectroscopy (Varian Mercury/VX 400 MHz spectrometer) using the WET solvent suppression pulse sequence. The sodium 3-(trimethylsilyl) propionate 2, 2, 3, 3-d (4) (TSP) was used as the internal standard to quantify the liquid product concentration.

## 3.3 Results & Discussion

**Structural Characterization:** Initial research focused on tuning the nitrogen bonding configuration and content in CNTs by using three different precursors: acetonitrile (ACN), dimethlyformamide (DMF) and triethylamine (TEA), and various growth temperatures: 750, 850 and 950 °C. **Figures 3.1 a and b** show the representative SEM images of as-synthesized NCNTs indicating the formation of well aligned NCNT arrays with an average length ~ 100 μm. The TEM image (**Figure 3.1c**) shows the bamboo-shaped morphology and multi-walled nature of the synthesized NCNTs. The bamboo-like structure is a characteristic feature of resident nitrogen atom defects in CNTs, which originates from the formation of a positive curvature surface during substitution of nitrogen atoms into the graphitic structure.[25] The local disorder and crystallinity were studied using Raman spectroscopy. **Figure 3.1d** shows the characteristic D and G-bands found in graphitic materials at ~ 1400 and 1600 $cm^{-1}$ respectively. The D-band arises from the disordered $sp^2$ hybridized carbon, while G-band is associated with the C-C tangential stretching mode and indicates the presence of crystalline graphitic carbon.[15] The D- to G-band intensity ratio ($I_D/I_G$) is sensitive to structural defects, increasing with higher nitrogen content. The full width at half maximum (FWHM), however, depends on both structural defects[15] and tube diameter.[26] The NCNTs synthesized using the ACN precursor at 850 ºC (NCNTs-ACN-850) exhibited the highest $I_D/I_G$ ratio because of the maximum nitrogen content. The diameter of NCNTs depends upon nitrogen content, which in turn is influenced by synthesis conditions.[27, 28] The $FWHM_D/FWHM_G$ ratio, however, decreased with increasing tube diameter and total nitrogen content, accounting for both structural defect density and curvature-induced strain in the NCNTs.[26]

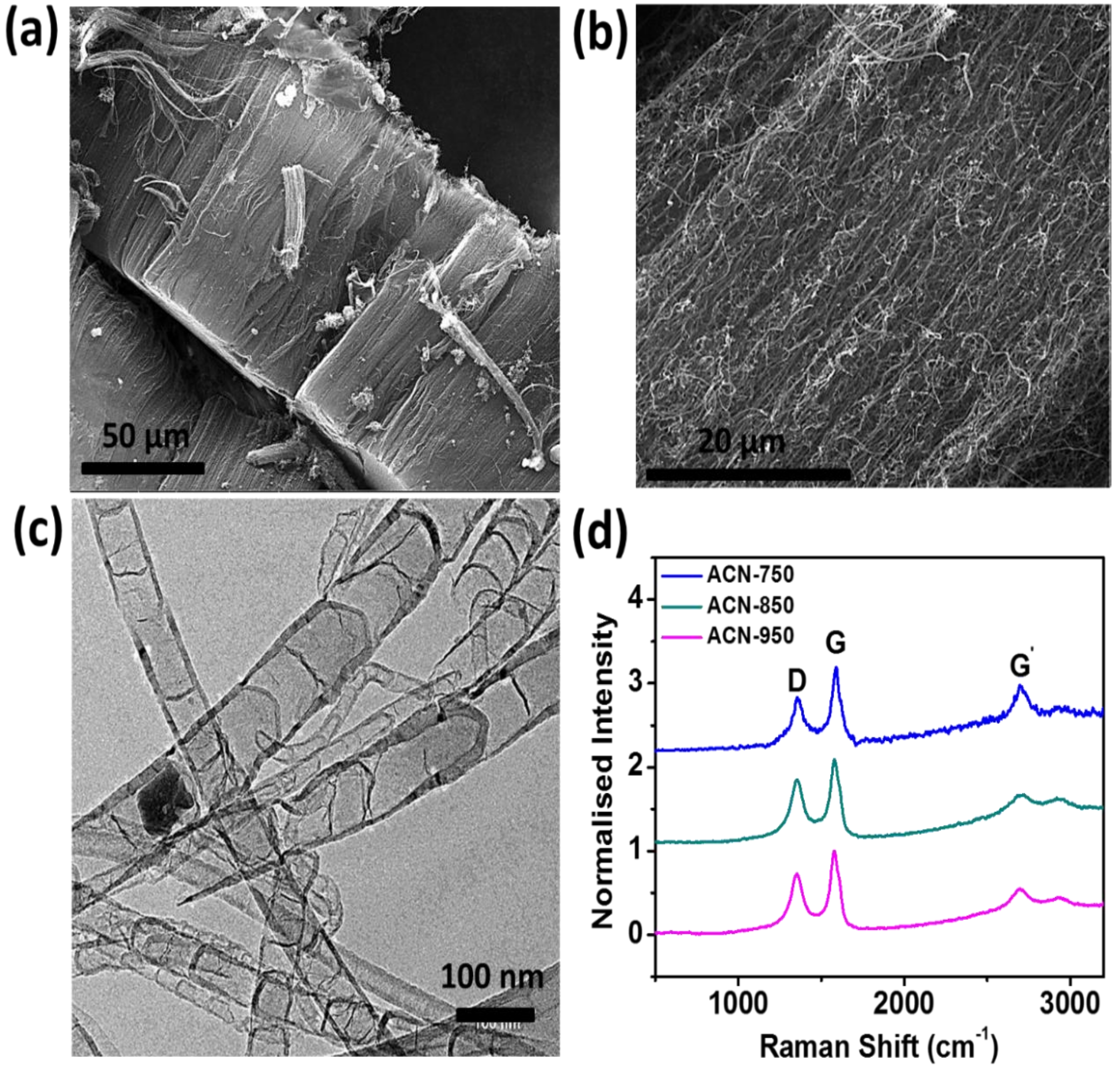

**Figure 3.1.** Physical characterization of as-synthesized NCNTs (a, b) Cross-sectional SEM images, (c) TEM image, (d) Raman spectra of NCNTs synthesized using ACN precursor at various temperatures.

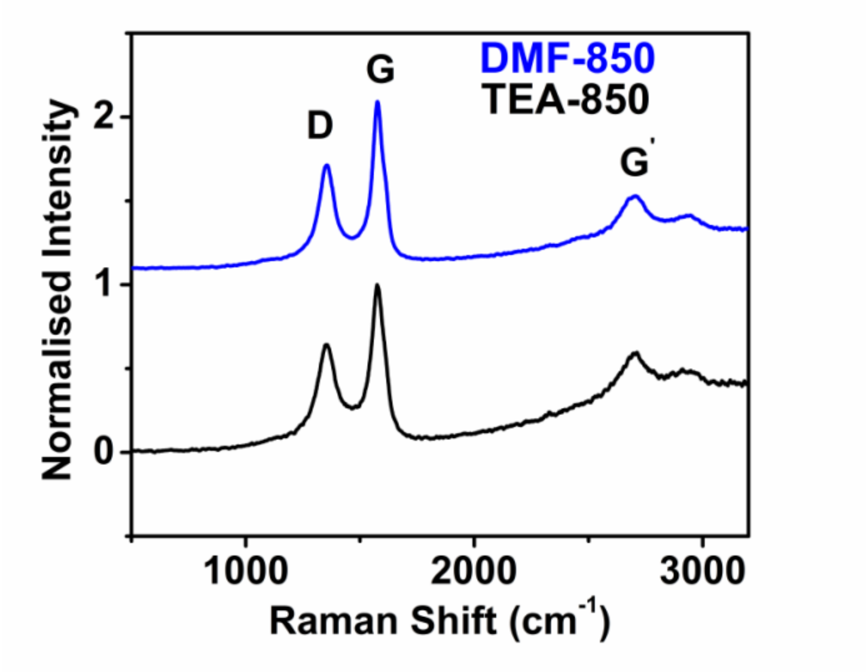

**Figure 3.2.** Raman spectra of NCNTs synthesized using dimethylformamide (DMF) and triethylamine (TEA) precursors at 850 °C, denoted by DMF-850 and TEA-850 respectively.

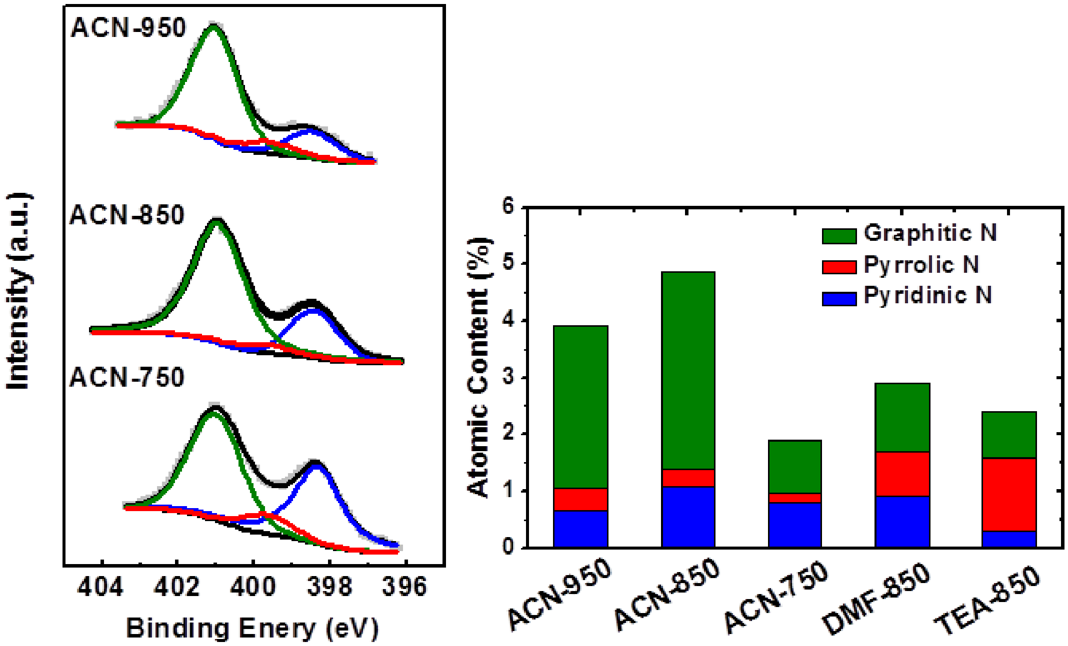

**Figure 3.3.** XPS results of N 1s of NCNTs synthesized using ACN precursor at various growth temperatures and comparison of different N contents in the synthesized NCNTs

**Electrocatalytic Activity:** The NCNT gas diffusion electrodes were assembled in a full electrochemical cell[29] to examine their catalytic activity towards $CO_2$ reduction reaction (CRR). CO and $HCOO^-$ were observed as gas and liquid products respectively, with CO as the major product. The trends in Faradaic efficiency (FE) for CO vs. potential on various NCNT electrodes are shown in **Figure 3.4a**. NCNTs-ACN-850 exhibited the highest catalytic activity, with the highest maximum FE and lowest onset potential for CO formation. NCNTs-ACN-850 catalyzed CO formation at a potential as low as -0.7 V, reaching the maximum FE of ~ 80% at -1.05 V, followed by a decreasing trend at more negative potentials. The decrease in FE at higher negative potentials stems from the dominance of the hydrogen evolution reaction (HER) over the CRR.[19] The onset potential for CO formation over a NCNTs-ACN-850 electrode was also more anodic the onset potentials observed for NCNTs-DMF-850 and NCNTs-TEA-850 -0.8 V and -1.0 V, respectively**.** In addition, the maximum FE for CO reached ~ 80% on the NCNTs-ACN-850 electrode compared to ~ 25% and 40% for TEA and DMF derived NCNTs, respectively. In order to compare the kinetics of CRR on various NCNTs, Tafel analysis was performed on the CO partial current density. A lower magnitude of Tafel slope is desirable,[30, 31] since this would indicate faster kinetics for CO formation. The Tafel slope for CO formation yielded the lowest value of 0.16 V/dec with NCNTs-ACN-850 **(Figure 3.4b)**. A change in the Tafel slope with overpotential was observed for NCNTs-DMF-850 and NCNTs-TEA-850 electrodes. The Tafel slope increased from 0.23 to 1.67 V/dec as the magnitude of overpotential was increased from 0.25 to 1 V on NCNTs-DMF-850. On a similar trend, for the NCNTs-TEA-850, Tafel slope increased from 0.46 to 0.78 V/dec as the magnitude of overpotential was increased from 0.6 to 1.4 V. A change in surface coverage of adsorbed species could cause this change in the Tafel slope.[32, 33, 34, 35, 36] In addition, at higher applied cathode potentials, the presence of more water molecules inside the electrical double layer can hinder electron transfer to reactant species,[33] resulting in higher values of Tafel slopes.

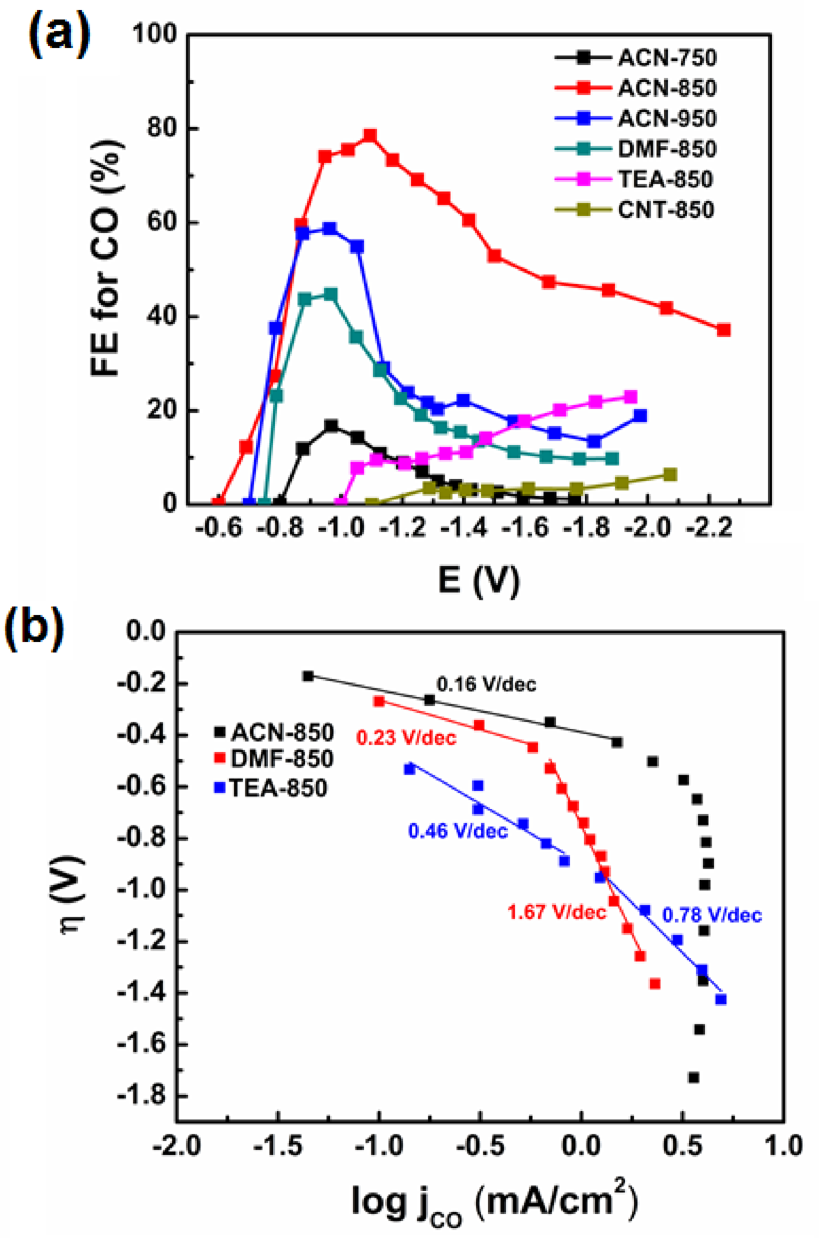

**Figure 3.4.** (a) Faradaic efficiency for CO versus potential on NCNTs synthesized using different precursors and growth temperatures. (b) Tafel plots for CO formation on NCNTs.

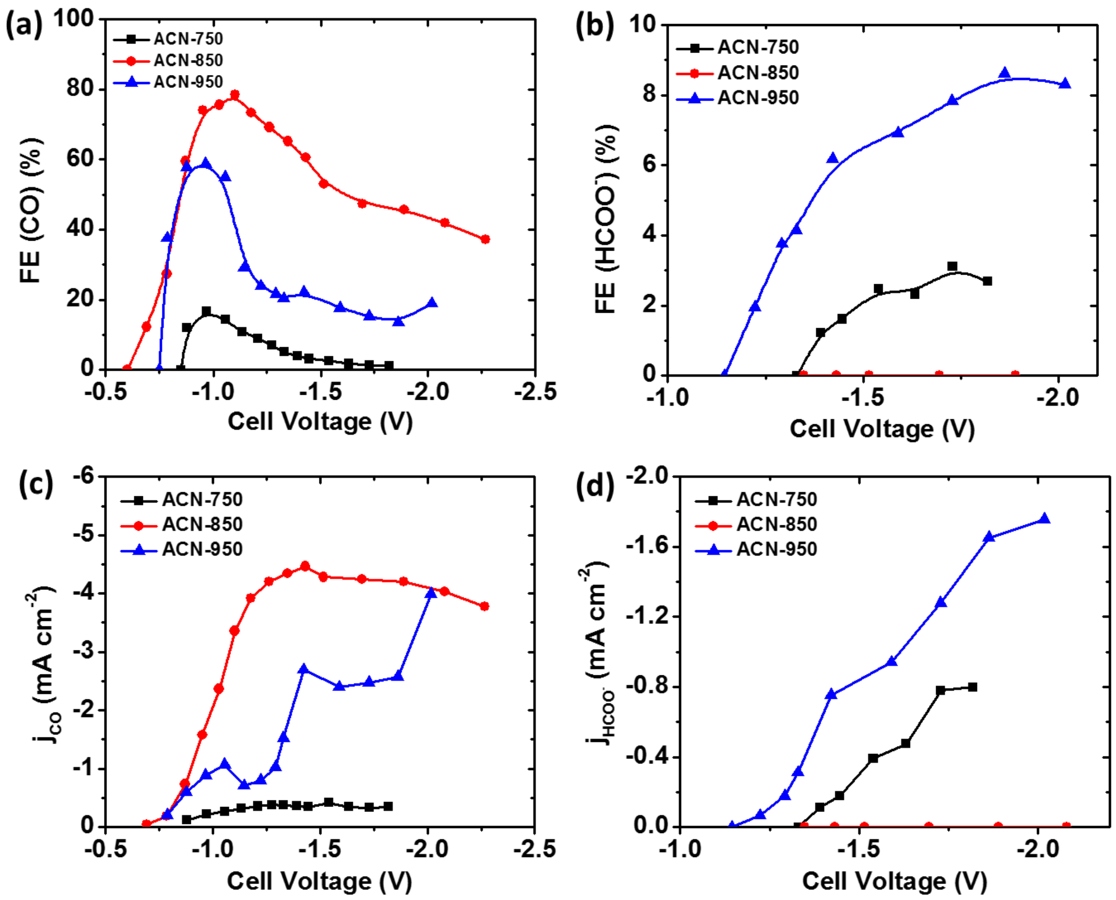

**Figure 3.5.** Dependence of electrocatalytic performance of NCNTs synthesized using acetonitrile (ACN) precursor at growth temperatures, i.e., 750, 850 and 950°C. (a) Faradaic efficiency for CO, (b) Faradaic efficiency for formate, (c) Partial current density for CO and (d) Partial current density for formate at different measured cell voltages.

**Figures 3.5 and 3.6** illustrate the trend in Faradaic efficiency towards CO and $HCOO^-$ formation as a function of applied cell voltage on different NCNTs, synthesized using various precursors at different growth temperatures. The reaction mechanism for formate formation is similar to that of CO through COOH* intermediate. However, the difference in selective protonation of oxygen atom over carbon atom can result in higher selectivity towards CO formation.

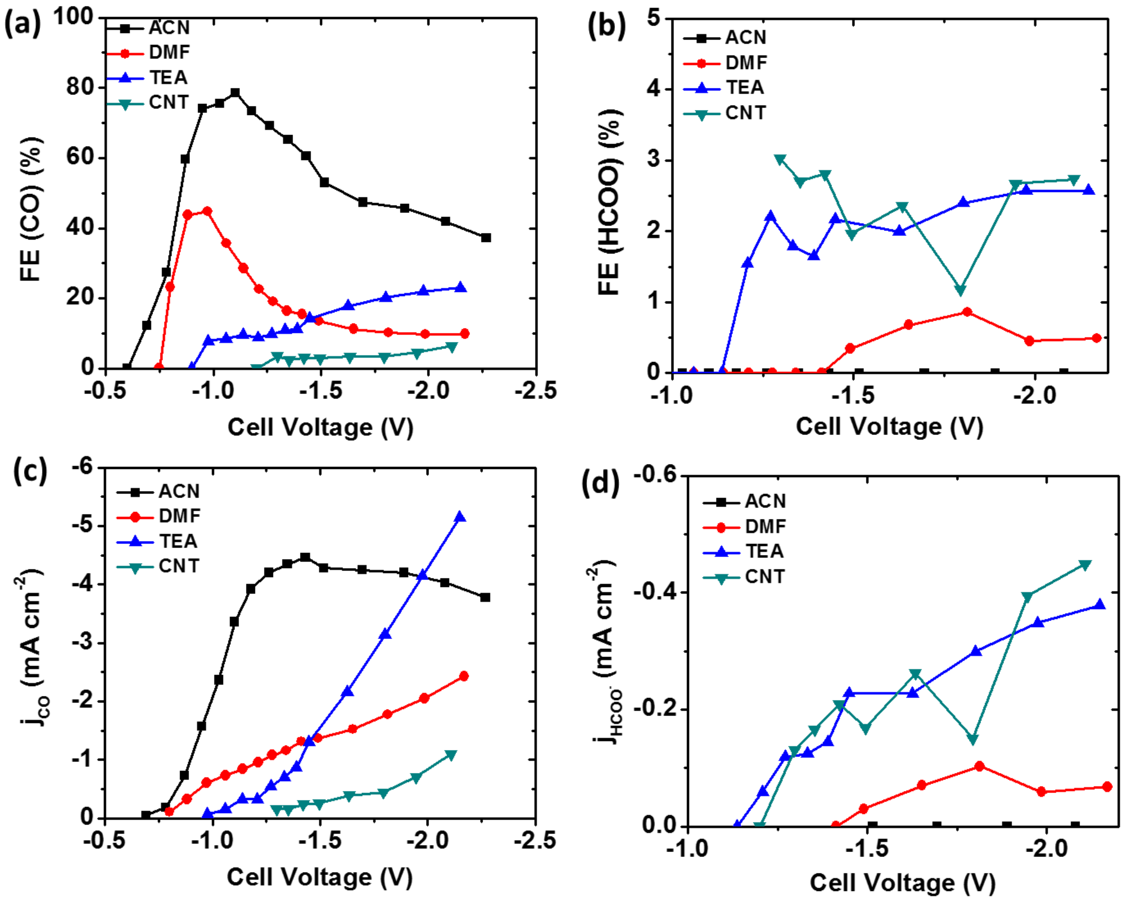

**Figure 3.6.** Electrocatalytic performance of NCNTs synthesized at 850°C using different precursors, i.e., acetonitrile (ACN), dimethylformamide (DMF) and triethylamine (TEA) in comparison to pristine CNTs (CNT). (a) Faradaic efficiency for CO, (b) Faradaic efficiency for formate, (c) Partial current density for CO and (d) Partial current density for formate at different measured cell voltages

**Defect Structure – Activity Relationship:** Despite the similar total nitrogen content in NCNTs-DMF-850 and NCNTs-TEA-850, the catalysts had remarkably different activities. The difference in nitrogen moieties between the NCNTs was hypothesized for the origin of the disparity in the catalytic activity. The first verification of this hypothesis can be deduced from the comparison of activity between pristine CNTs and NCNTs electrodes. The selectivity (Faradaic efficiency) and overpotential in this work shows the independence on the electrochemical active surface area. The CNTs exhibit a much lower selectivity and larger overpotential than NCNTs despite a greater electrochemical surface area listed in **Table 3.1.** The relationship between the nitrogen functionality content in NCNTs and the associated CRR activity is illustrated in **Figure 3.9a**. The figure shows that the catalytic activity descriptor of NCNTs, i.e., the onset potential for CO formation has a positive correlation with the pyridinic and graphitic-nitrogen contents. As the pyridinic and graphitic nitrogen contents increased in NCNTs from 0.3 to 1.1 at.% and from 0.8 to 3.5 at.%, respectively, the onset potential became more anodic, decreasing from -1.05 to -0.7 V. Following a similar trend, the maximum achievable FE for CO increased from ~ 14 to 80% as both pyridinic and graphitic N contents increased. This observation provides direct evidence that both pyridinic and graphitic N defects are active sites for CRR, eventually leading to the formation of CO.

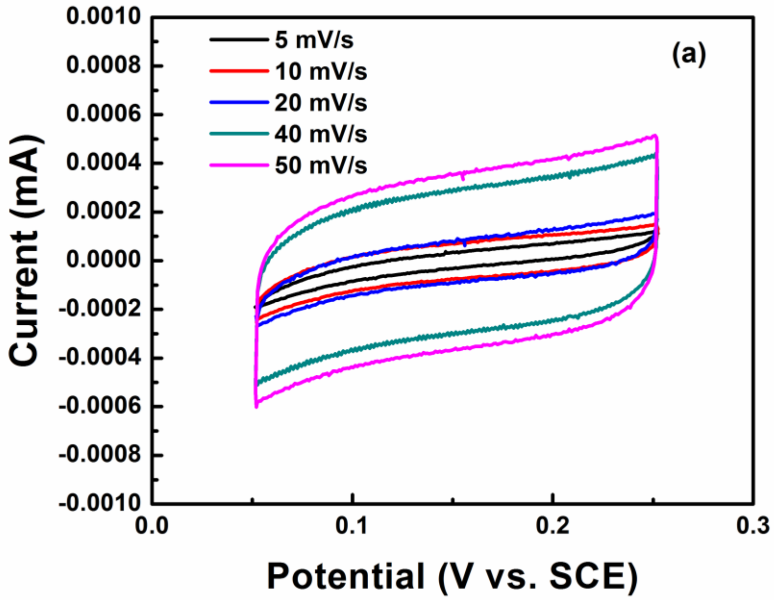

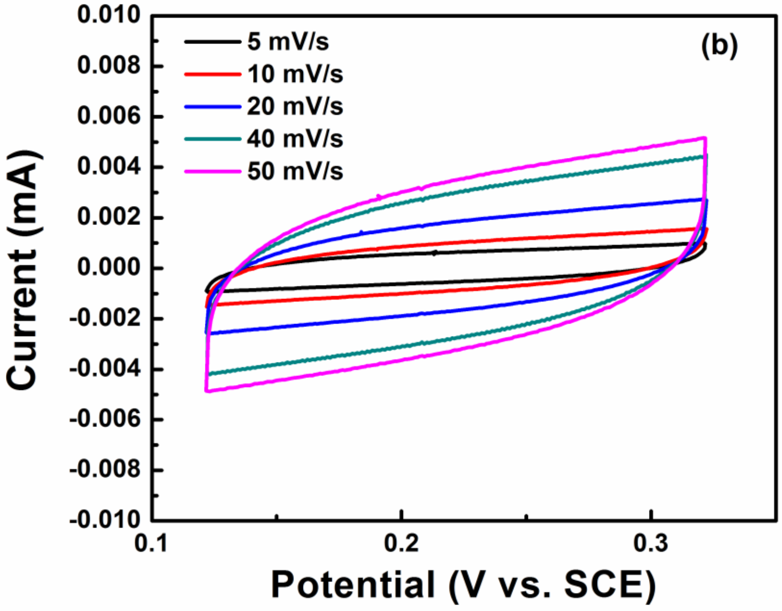

0.010
0.008
0.006
0.004
0.002
0.000
-0.002
-0.004
-0.006
-0.008
-0.010
Current (mA)
0.1
0.2
0.3
Potential (V vs. SCE)
5 mV/s
10 mV/s
20 mV/s
40 mV/s
50 mV/s
(b)

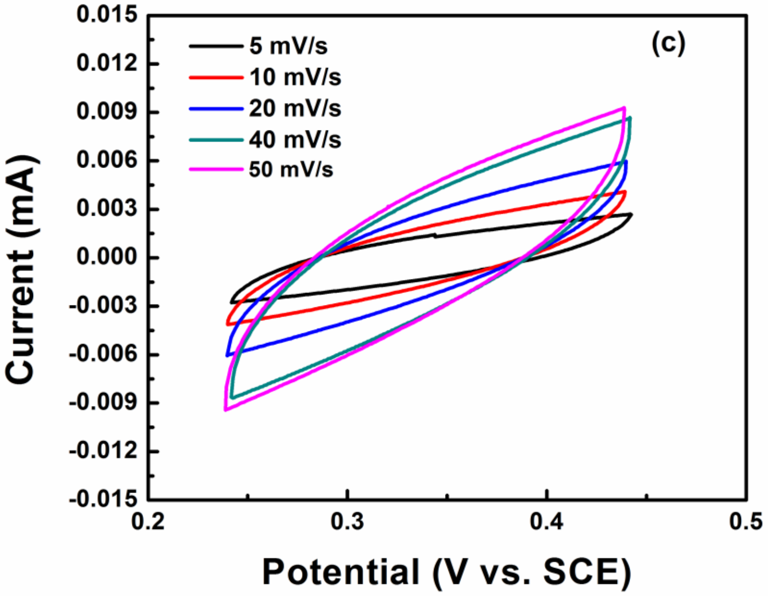

0.015
0.012
0.009
0.006
0.003
0.000
-0.003
-0.006
-0.009
-0.012
-0.015
Current (mA)
0.2
0.3
0.4
0.5
Potential (V vs. SCE)
5 mV/s
10 mV/s
20 mV/s
40 mV/s
50 mV/s
(c)

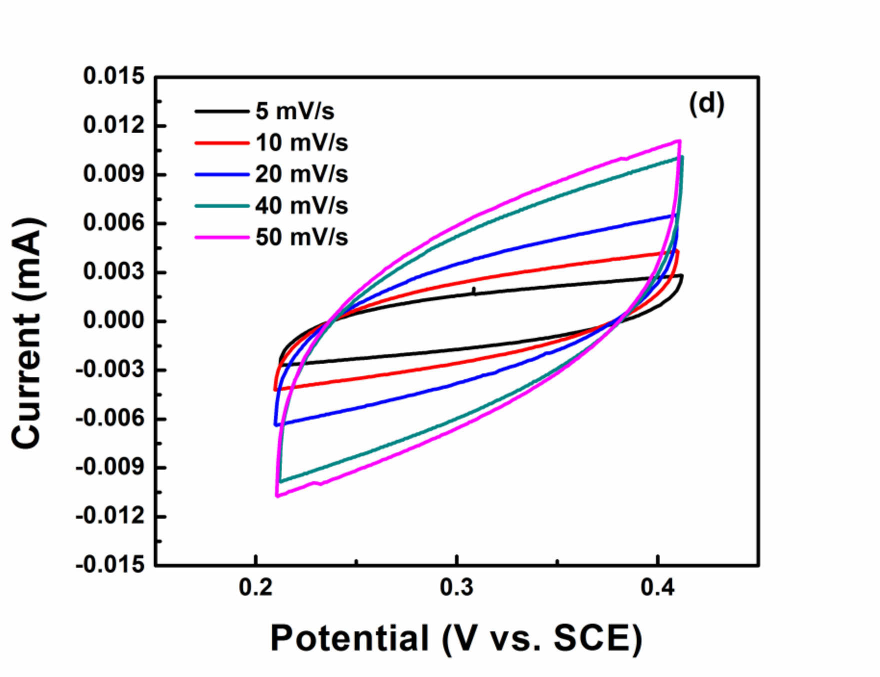

**Figure 3.7.** Cyclic voltammograms of different electrodes studied in 0.1 M $Na_2SO_4$ (a) Carbon gas diffusion layer (GDL) (b) Pristine CNTs (c) NCNTs synthesized using DMF precursor (NCNTs-DMF) (d) NCNTs synthesized using TEA precursor (NCNTs-TEA). The geometric area of all electrodes is 1 $cm^2$.

**Table 3.1.** Double layer capacitance for various electrodes. The geometric area of all electrodes is 1 $cm^2$.

| Electrode | Capacitance (µF) |
|---|---|
| Carbon gas diffusion layer | 10 |
| Pristine CNTs | 130 |
| NCNTs-DMF | 100 |
| NCNTs-TEA | 200 |

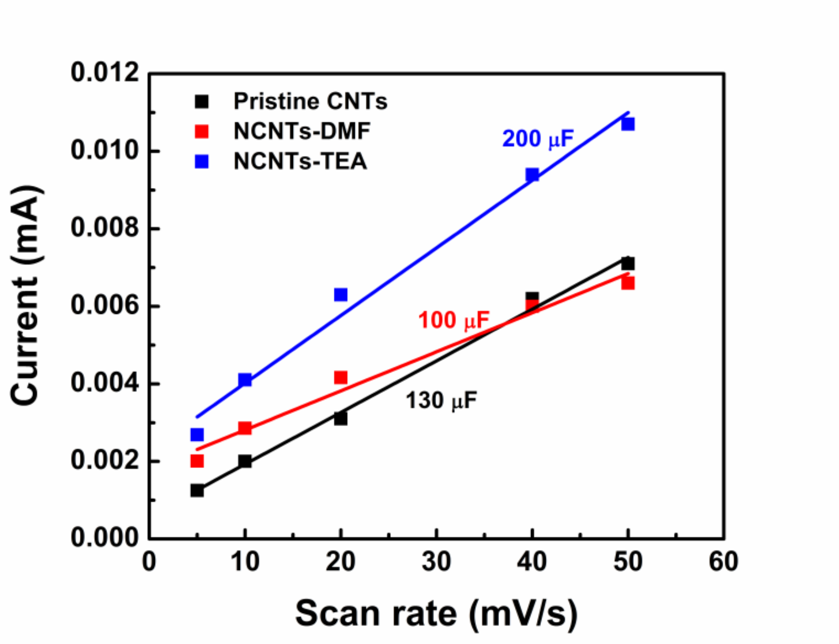

**Figure 3.8.** Comparison of double layer capacitance values for different NCNT electrodes. The geometric area of all electrodes is 1 $cm^2$.

The catalytic activity of pyridinic or graphitic-nitrogen site alone, however, cannot be distinguished based on the experimental data. This is also true for the case of ORR, where the active site remains obscure between pyridinic and graphitic N defects.[15, 37, 38, 39] However, an increase in pyrrolic N content from 0.78 to 1.3 at.% resulted in more cathodic onset potentials from -0.78 to -1.05 V. This cathodic shift in the onset potentials was also accompanied by a decrease in maximum achievable FE for CO from ~ 40 to 25% upon increasing the pyrrolic N content, indicating a low activity for CRR at pyrrolic N defects. The higher catalytic activity of NCNTs-DMF-850 compared to NCNTs-TEA-850 can be understood by the relatively higher pyridinic N content of ~ 0.9 at.% in the NCNTs-DMF-850 to only ~ 0.3 at.% pyridinic N in the NCNTs-TEA-850.

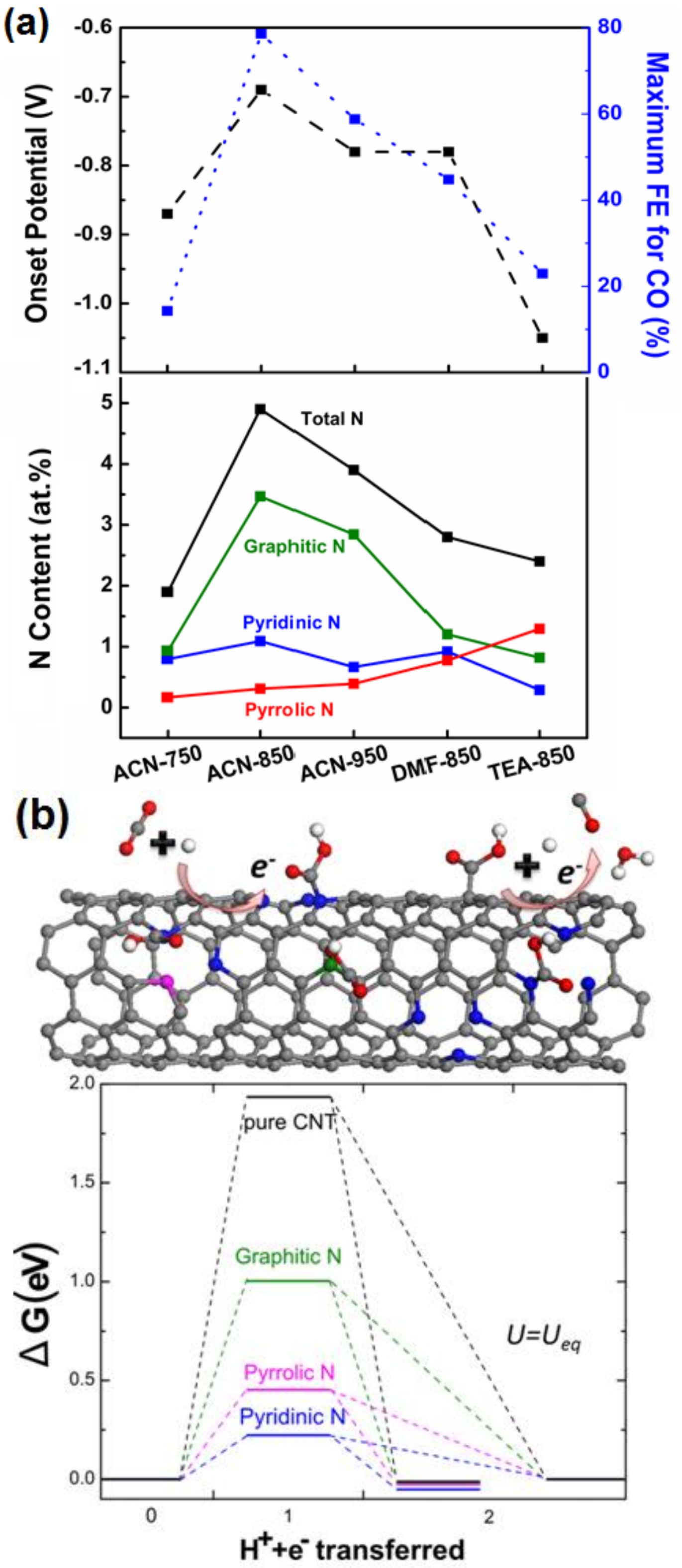

**Figure 3.9.** (a) The onset potential and maximum Faradaic efficiency for CO formation as a function of N-content in the synthesized NCNTs (b) Schematic illustrating CO formation on the NCNTs and free energy diagram at equilibrium potential for $CO_2$

reduction on different N-defects, i.e. pyridinic, pyrrolic and graphitic N in comparsion to pristine CNTs. C, O and H atoms are represented by grey, red and white spheres, while pyridinic, pyrrolic and graphitic N defects are shown using blue, pink and green spheres respectively. DFT calculations were done by Mingjie Liu at Rice University.

The N-defect sites inside the graphitic carbon network facilitate the proton-electron pair transfers resulting in CO formation as shown in **Figure 3.9b**. DFT calculations predict the lowest absolute overpotential of ~ 0.20 V for COOH*, an intermediate formed by the first coupled proton- electron transfer to $CO_2$ at a pyridinic N site, which eventually leads to CO formation.[19] Excess negative charge in the graphite basal plane is localized at the nitrogen atoms in the pyridine-like structure, resulting in its higher catalytic activity. Previous DFT work examining the ORR activity of NCNTs, has shown the wide disparity between the electronic density of states (DOS) for different nitrogen defect moieties. The DOS studies show that pyridinic defects retain a lone pair of electrons, which could bind $CO_2$. However, for graphitic-like nitrogen, electrons are located in the π*anti-bonding orbital, making them less accessible for $CO_2$ binding.[40] Although graphitic N exhibits a ~ 1 eV higher barrier, than pyridinic N for $COOH^*$ formation (**Figure 3.9b**), it still lowers the overpotential by ~ 1 V in comparison to pristine CNTs, thus demonstrating significant activity. While pyrrolic defects have nitrogen based lone pair, the geometry of the defect moves the nitrogen atom towards the center of the tube making these electrons harder to access for $CO_2$ binding.[19] Furthermore, a careful inspection reveals that $COOH^*$ tends to bind to the adjacent pyridinic-like N site, instead of the pyrrolic N, during the reduction process. Therefore, CRR isn't promoted by only increasing pyrrolic N content, supporting the experimental observations.

## 3.4 Conclusions

In summary, NCNTs were synthesized with various surface structures and nitrogen contents by choosing different precursors (ACN, DMF and TEA) and controlling the growth temperature. The catalytic activity of these NCNTs was found to depend upon the nature of nitrogen defects and defect density. The presence of graphitic and pyridinic N defects significantly decreases the absolute overpotential and increases the selectivity towards CO formation in comparison to pristine CNTs. NCNTs-ACN-850 exhibited the highest catalytic activity, i.e. the lowest overpotential (~ -0.18 V) and maximum selectivity (~ 80% FE) owing to the highest pyridinic (~ 1.1 at.%) and graphitic N (~ 3.5 at.%) content. Furthermore, pyrrolic N defects seem to have little or no impact on CRR activity, which is in congruent with DFT calculations.

## References

1. Friedlingstein P, *et al.* Persistent growth of $CO_2$ emissions and implications for reaching climate targets. *Nature Geosci* **7**, 709-715 (2014).

2. Olah GA, Prakash GKS, Goeppert A. Anthropogenic Chemical Carbon Cycle for a Sustainable Future. *Journal of the American Chemical Society* **133**, 12881-12898 (2011).

3. Arakawa H, *et al.* Catalysis Research of Relevance to Carbon Management: Progress, Challenges, and Opportunities. *Chemical Reviews* **101**, 953-996 (2001).

4. Whipple DT, Kenis PJA. Prospects of $CO_2$ Utilization via Direct Heterogeneous Electrochemical Reduction. *The Journal of Physical Chemistry Letters* **1**, 3451-3458 (2010).

5. Hori Y, Wakebe H, Tsukamoto T, Koga O. Electrocatalytic process of CO selectivity in electrochemical reduction of $CO_2$ at metal electrodes in aqueous media. *Electrochimica Acta* **39**, 1833-1839 (1994).

6. Noda H, Ikeda S, Oda Y, Imai K, Maeda M, Ito K. Electrochemical Reduction of Carbon Dioxide at Various Metal Electrodes in Aqueous Potassium Hydrogen Carbonate Solution. *Bulletin of the Chemical Society of Japan* **63**, 2459-2462 (1990).

7. Augustynski J, Kedzierzawski P, Jermann B. Electrochemical reduction of $CO_2$ at metallic electrodes. In: *Studies in Surface Science and Catalysis* (ed^(eds T. Inui MAKISY, Yamaguchi T). Elsevier (1998).

8. Gong K, Du F, Xia Z, Durstock M, Dai L. Nitrogen-Doped Carbon Nanotube Arrays with High Electrocatalytic Activity for Oxygen Reduction. *Science* **323**, 760-764 (2009).

9. Zheng Y, *et al.* Nanoporous Graphitic-$C_3N_4$@Carbon Metal-Free Electrocatalysts for Highly Efficient Oxygen Reduction. *Journal of the American Chemical Society* **133**, 20116-20119 (2011).

10. Liu R, Wu D, Feng X, Müllen K. Nitrogen-Doped Ordered Mesoporous Graphitic Arrays with High Electrocatalytic Activity for Oxygen Reduction. *Angewandte Chemie International Edition* **49**, 2565-2569 (2010).

11. Li Y, *et al.* An oxygen reduction electrocatalyst based on carbon nanotube-graphene complexes. *Nat Nano* **7**, 394-400 (2012).

12. Wang S, Yu D, Dai L. Polyelectrolyte Functionalized Carbon Nanotubes as Efficient Metal-free Electrocatalysts for Oxygen Reduction. *Journal of the American Chemical Society* **133**, 5182-5185 (2011).

13. Kundu S, *et al.* Electrocatalytic Activity and Stability of Nitrogen-Containing Carbon Nanotubes in the Oxygen Reduction Reaction. *The Journal of Physical Chemistry C* **113**, 14302-14310 (2009).

14. Mo Z, Liao S, Zheng Y, Fu Z. Preparation of nitrogen-doped carbon nanotube arrays and their catalysis towards cathodic oxygen reduction in acidic and alkaline media. *Carbon* **50**, 2620-2627 (2012).

15. Rao CV, Cabrera CR, Ishikawa Y. In Search of the Active Site in Nitrogen-Doped Carbon Nanotube Electrodes for the Oxygen Reduction Reaction. *The Journal of Physical Chemistry Letters* **1**, 2622-2627 (2010).

16. Kumar B, *et al.* Renewable and metal-free carbon nanofibre catalysts for carbon dioxide reduction. *Nat Commun* **4**, (2013).

17. Rosen BA, *et al.* Ionic Liquid–Mediated Selective Conversion of $CO_2$ to CO at Low Overpotentials. *Science* **334**, 643-644 (2011).

18. Zhang S, *et al.* Polyethylenimine-Enhanced Electrocatalytic Reduction of $CO_2$ to Formate at Nitrogen-Doped Carbon Nanomaterials. *Journal of the American Chemical Society* **136**, 7845-7848 (2014).

19. Wu J, *et al.* Achieving Highly Efficient, Selective, and Stable $CO_2$ Reduction on Nitrogen-Doped Carbon Nanotubes. *ACS Nano*, (2015).

20. Srivastava A, Srivastava ON, Talapatra S, Vajtai R, Ajayan PM. Carbon nanotube filters. *Nat Mater* **3**, 610-614 (2004).

21. Yadav R, Dobal P, Shripathi T, Katiyar R, Srivastava O. Effect of Growth Temperature on Bamboo-shaped Carbon-Nitrogen (C-N) Nanotubes Synthesized Using Ferrocene Acetonitrile Precursor. *Nanoscale Research Letters* **4**, 197 - 203 (2008).

22. Wu J, Risalvato FG, Sharma PP, Pellechia PJ, Ke F-S, Zhou X-D. Electrochemical Reduction of Carbon Dioxide: II. Design, Assembly, and Performance of Low Temperature Full Electrochemical Cells. *Journal of The Electrochemical Society* **160**, F953-F957 (2013).

23. Wu J, Risalvato FG, Ma S, Zhou X-D. Electrochemical reduction of carbon dioxide III. The role of oxide layer thickness on the performance of Sn electrode in a full electrochemical cell. *Journal of Materials Chemistry A* **2**, 1647-1651 (2014).

24. Peterson AA, Abild-Pedersen F, Studt F, Rossmeisl J, Nørskov JK. How copper catalyzes the electroreduction of carbon dioxide into hydrocarbon fuels. *Energy & Environmental Science* **3**, 1311-1315 (2010).

25. Sumpter BG, *et al.* A theoretical and experimental study on manipulating the structure and properties of carbon nanotubes using substitutional dopants. *International Journal of Quantum Chemistry* **109**, 97-118 (2009).

26. Antunes EF, Lobo AO, Corat EJ, Trava-Airoldi VJ. Influence of diameter in the Raman spectra of aligned multi-walled carbon nanotubes. *Carbon* **45**, 913-921 (2007).

27. Koós AA, Dowling M, Jurkschat K, Crossley A, Grobert N. Effect of the experimental parameters on the structure of nitrogen-doped carbon nanotubes produced by aerosol chemical vapour deposition. *Carbon* **47**, 30-37 (2009).

28. Liu H, *et al.* Structural and morphological control of aligned nitrogen-doped carbon nanotubes. *Carbon* **48**, 1498-1507 (2010).

29. Wu J, Risalvato FG, Sharma PP, Pellechia PJ, Ke F-S, Zhou X-D. Electrochemical Reduction of Carbon Dioxide II. Design, Assembly, and Performance of Low Temperature Full Electrochemical Cells. *Journal of The Electrochemical Society* **160**, F953-F957 (2013).

30. Ma G, *et al.* Nitrogen-Doped Hollow Carbon Nanoparticles with Excellent Oxygen Reduction Performances and Their Electrocatalytic Kinetics. *The Journal of Physical Chemistry C* **115**, 25148-25154 (2011).

31. Zhong S, Zhou L, Wu L, Tang L, He Q, Ahmed J. Nitrogen- and boron-co-doped core–shell carbon nanoparticles as efficient metal-free catalysts for oxygen reduction reactions in microbial fuel cells. *Journal of Power Sources* **272**, 344-350 (2014).

32. King F, Quinn MJ, Litke CD. Oxygen reduction on copper in neutral NaCl solution. *Journal of Electroanalytical Chemistry* **385**, 45-55 (1995).

33. Chang CC, Wen TC. Kinetics of oxygen reduction at $RuO_2$-coated titanium electrode in alkaline solution. *Journal of Applied Electrochemistry* **27**, 355-363 (1997).

34. Jiang L, Hsu A, Chu D, Chen R. Ethanol electro-oxidation on Pt/C and PtSn/C catalysts in alkaline and acid solutions. *International Journal of Hydrogen Energy* **35**, 365-372 (2010).

35. Baranton S, Coutanceau C, Garnier E, Léger JM. How does α-FePc catalysts dispersed onto high specific surface carbon support work towards oxygen

reduction reaction (orr)? *Journal of Electroanalytical Chemistry* **590**, 100-110 (2006).

36. Wu G, Li L, Xu B-Q. Effect of electrochemical polarization of PtRu/C catalysts on methanol electrooxidation. *Electrochimica Acta* **50**, 1-10 (2004).

37. Deng D, *et al.* Toward N-Doped Graphene via Solvothermal Synthesis. *Chemistry of Materials* **23**, 1188-1193 (2011).

38. Lai L, *et al*. Exploration of the active center structure of nitrogen-doped graphene-based catalysts for oxygen reduction reaction. *Energy & Environmental Science* **5**, 7936-7942 (2012).

39. Chen Z, Higgins D, Tao H, Hsu RS, Chen Z. Highly Active Nitrogen-Doped Carbon Nanotubes for Oxygen Reduction Reaction in Fuel Cell Applications. *The Journal of Physical Chemistry C* **113**, 21008-21013 (2009).

40. Ni S, Li Z, Yang J. Oxygen molecule dissociation on carbon nanostructures with different types of nitrogen doping. *Nanoscale* **4**, 1184-1189 (2012).

# Chapter 4

# Incorporation of Nitrogen Defects for Efficient Reduction of $CO_2$ via Two-Electron Pathway on Three-Dimensional Graphene Foam

## 4.1 Introduction

The carbon-neutral fuel production from $CO_2$ reduction via electrolytic synthesis using renewable energy or photosynthesis is a promising route to close the anthropogenic carbon cycle. Achieving this goal largely relies on the development of catalysts, capable of mediating multi-proton-coupled electron transfers involved in $CO_2$ reduction. The direct conversion of $CO_2$ to hydrocarbons (e.g. methane, ethylene) and multi-carbon oxygenates (e.g. ethanol, acetate and n-propanol) remains a grand challenge due to lack of efficient and robust catalysts, coupled with limited understanding of the catalytic process. Copper-based electrocatalysts only have been demonstrated to convert $CO_2$ to hydrocarbons, methanol and multi-carbon oxygenates at a low yield.[1, 2, 3, 4] An alternative way for synthesizing these products could comprise two steps, first involving electrochemical $CO_2$ conversion to CO followed by further reduction of CO via heterogeneous catalysis (e.g. Fischer–Tropsch process). Indeed, to develop a catalyst for $CO_2$ reduction to CO with high energy efficiency, selectivity and durability is of paramount importance. Metallic catalysts such as Au and Ag offer good selectivity in this regard, but their limited availability and poor durability hinder the practical applications.[5, 6, 7, 8] Recently, carbon nanostructured materials have attracted attention as metal-free electrocatalysts for $CO_2$ reduction because of their low cost, high surface areas and adjustable doping of heteroatoms (e.g. nitrogen, boron etc). The nitrogen (N)-doped carbon nanofibres exhibited negligible overpotential (-0.17 V) for $CO_2$ reduction using ionic liquid as electrolyte and one order of magnitude higher current density compared with bulk Ag under similar experimental conditions.[9] N-doped carbon nanotubes (NCNTs) were employed to convert $CO_2$ to formate in an aqueous medium using polyethyleneimine as a co-catalyst, achieving a maximum Faradaic efficiency (FE) of ~ 60% at an overpotential of ~ -1.2 V.[10] Furthermore, $CO_2$ reduction to CO was reported on NCNTs arrays having total N content of ~ 5 atom% in aqueous electrolyte at a negligible onset overpotential (-0.18 V), and attaining a FE for CO ~ 80% at an overpotential lower than -0.3 V.[11] These results highlight the non-trivial role of resident N-defects in carbon lattice towards $CO_2$ reduction. Exploring the structure of active site (e.g., pyridinic, pyrrolic and graphitic N) for $CO_2$ reduction in NCNTs is, however, challenging due to additional curvature effects on catalytic activity. Graphene has similar chemical structure to CNTs, making it equally attractive for catalytic applications. In addition, graphene, because of its planar structure allows for a systematic study of catalytic activity on different N-defect structures inside carbon network.

Consequently, the electrocatalysis of $CO_2$ reduction is reported on N-doped three dimentional (3D) graphene foam synthesized by chemical vapor deposition (CVD). The 3D hierarchical structure enables the easy penetration of electrolyte, thus increasing the interfacial area between graphene foam and electrolyte. In addition, doping of nitrogen heteroatoms into graphene structure generates the active sites for $CO_2$ reduction with an unprecedented low overpotential, high selectivity and durability. The CVD method enables formation of graphene sheets without non-carbon functional groups and trace metal contamination, thereby allowing for the investigation of intrinsic catalytic activity resulting from the resident N-defects. A detailed experimental study was performed, in combination with density functional theory (DFT) modeling to understand the role of distinct nitrogen defects on electrocatalytic $CO_2$ reduction.

## 4.2 Experimental Methods

**Materials synthesis:** The three-dimensional (3D) graphene foam was synthesized by chemical vapor deposition (CVD) of dissociating methane to deposit on Ni foam at 1000 $^oC$ and ambient-pressure. $Ar/H_2$ is purging through the whole synthesis process. The graphene was collected by etching Ni substrate using concentrated HCl solution, followed by vacuum filtering and freezing dry. The as grown graphene foam is free of Ni contamination as evidenced in the previous report.[12] N-doped graphene (NG) was prepared by post-doping the graphene foam using a solid precursor of g-$C_3N_4$ at the temperature range of 700-1000 ºC to vary the N atomic concentration.

**Structural and microstructural characterizations:** The microstructures of NG were characterized by FEI Quanta 400 FEG scanning electron microscope and JEOL 2100 FEG transmission electron microscope. The structural disorder related to N doping was studied by the Raman spectra (Renishaw inVia *Raman microscope, 514.5 nm laser excitation).* The N content and boning state was analyzed by PHI Quantera X-ray photoelectron spectrometer.

**Electrode preparation and electrochemical measurement:** The NG gas diffusion electrodes (NG GDEs) were fabricated from the NG. The details of GDE preparation can be found in our previous work.[13] The GDEs electrode area is 3.8 $cm^2$ and have a NG loading between 0.3~0.5 mg $cm^{-2}$. The $CO_2$ reduction study was performance in a home-designed full electrochemical cell composed of NG GDEs s as the cathode and Pt GDE as the anode, and a Nafion membrane between cathode and anode for separation of gas reactant and product. The cathode was supplied with $CO_2$ at a rate of 45 SCCM while Pt anode is supplied with $H_2$ at a rate of 50 SCCM. The Pt GDE has Pt loading of 0.3 mg $cm^{-2}$. The overpotential of $H_2$ oxidation on Pt GDE is negligible[14], so the cathode potential is scaled to reversible hydrogen electrode after iR correction, $E_{RHE} = E_{cell} + iR + 0.0591pH$. The $CO_2$ reduction occurs in the electrolyte of 0.1 M $KHCO_3$ at room temperature and ambient pressure.[13] The $CO_2$ reduction was conducted under the potentiostatic mode for 30 min at each potential controlled by the potentiostat/galvanostat (Solartron 1470E). Electrochemical impedance spectroscopy was carried out to measure the Ohmic resistance of the full electrochemical cell at open circuit voltage, with an amplitude of 5 mV and frequency range from 100 kHz to 0.1 Hz.

**Product quantification:** The CO gas concentration was measured by directly venting the outlet of the cathodic compartment into the gas-sampling loop of the gas chromatography (GC, Inficon Micro 3000 GC). A GC run repeats every 10 minutes. The average value of three measurements was taken as the gas concentration for Faradaic efficiency calculation. Liquid products were identified using 1D $^1H$ NMR spectroscopy (Varian Mercury/VX 400 MHz spectrometer) in a self-programmed WET solvent suppression pulse sequence. The sodium 3-(trimethylsilyl) propionate 2, 2, 3, 3-d (4) (TSP) was used as the internal standard to quantify the liquid product concentration.[15]

## 4.3 Results & Discussion

**Structural Characterization:** The 3D graphene foam is grown by ambient-pressure CVD using methane as precursor on the template of Ni foam.[19] The as-grown graphene foam is then post-doped with a solid nitrogen rich precursor graphitic-$C_3N_4$ at different temperatures, creating resident N-defects. Finally, the N-doped 3D graphene foam (NG) is obtained by etching Ni skeletons with HCl solution followed by repeated water washes and freeze-drying. The scanning electron microscopy (SEM) image **(Figure 4.2a and b)** shows 3D micro-porous structure of the representative N-doped graphene doped at 800 $^{o}$C (denoted as NG-800). The transmission electron microscopy (TEM) study of folded edges and two sets of hexagonal diffraction spots in the fast Fourier transform (FFT) pattern show that NG sheets are composed of few layers **(Figure 4.2c and d)**. The peak intensity ratio of G to 2D band observed in the Raman spectra varies from 0.75-0.87, also suggesting the presence of 2-4 layers in the synthesized NGs **(Figure 4.1)**.[20, 21] Furthermore, the hexagonal diffraction pattern reveals that carbon $sp^2$ structure in graphene is maintained after incorporation of N heteroatoms, in agreement with the small value (0.1-0.2) of peak intensity ratio of D to G band **(Figure 4.1)**. The surface content and chemical states of nitrogen were analyzed using X-ray photoelectron spectroscopy. The deconvolution of N1s peak reveals three different bonding states of N atom at 398.5, 400.1, and 401.2 eV, corresponding to pyridinic, pyrrolic, and graphitic-N, respectively (Figure 1e).[22, 23]

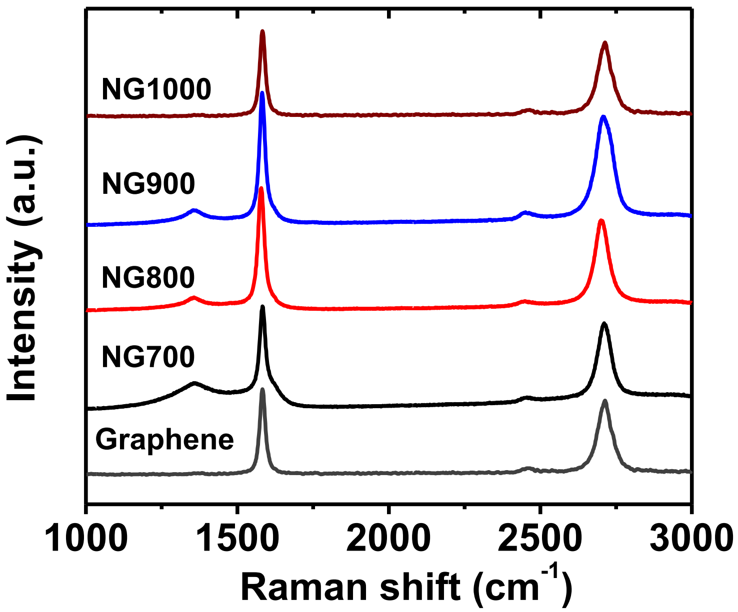

**Figure 4.1.** Raman spectra of pristine graphene and N-doped graphene

NG-800 possesses the highest total N content (~ 6.5 atom%) based on N/(N+C) atomic ratio followed by NG-700, NG-900 and NG-1000 **(Figure 4.2f)**. The decrease in N content with increase of temperature could be ascribed to the removal of some relatively unstable N functional groups such as pyridinic and pyrrolic-N at high temperature, consistent with previous findings.[23, 24, 25] Pyridinic-N predominates in all NGs, and the highest pyridinic-N reaches 4.1 atom% in NG-800 **(Figure 4.2f)**.

**Electrocatalytic Activity:** The NG-800 electrode was initially evaluated for $CO_2$ reduction in a custom-designed full electrochemical cell[13] because of its maximum N content. **Figure 4.4** shows the performance of NG-800 in a low-potential regime, i.e., -0.30 to -0.58 V versus the reversible hydrogen electrode (RHE; all potentials are referenced to this electrode), in terms of the total geometric current density (j) and FE for

CO versus time along with overall FE for $HCOO^-$. CO formation started at -0.30 V with a FE of ~25% and j of ~300 μA $cm^{-2}$ over an operation of 5 h (**Figure 4.4a**).

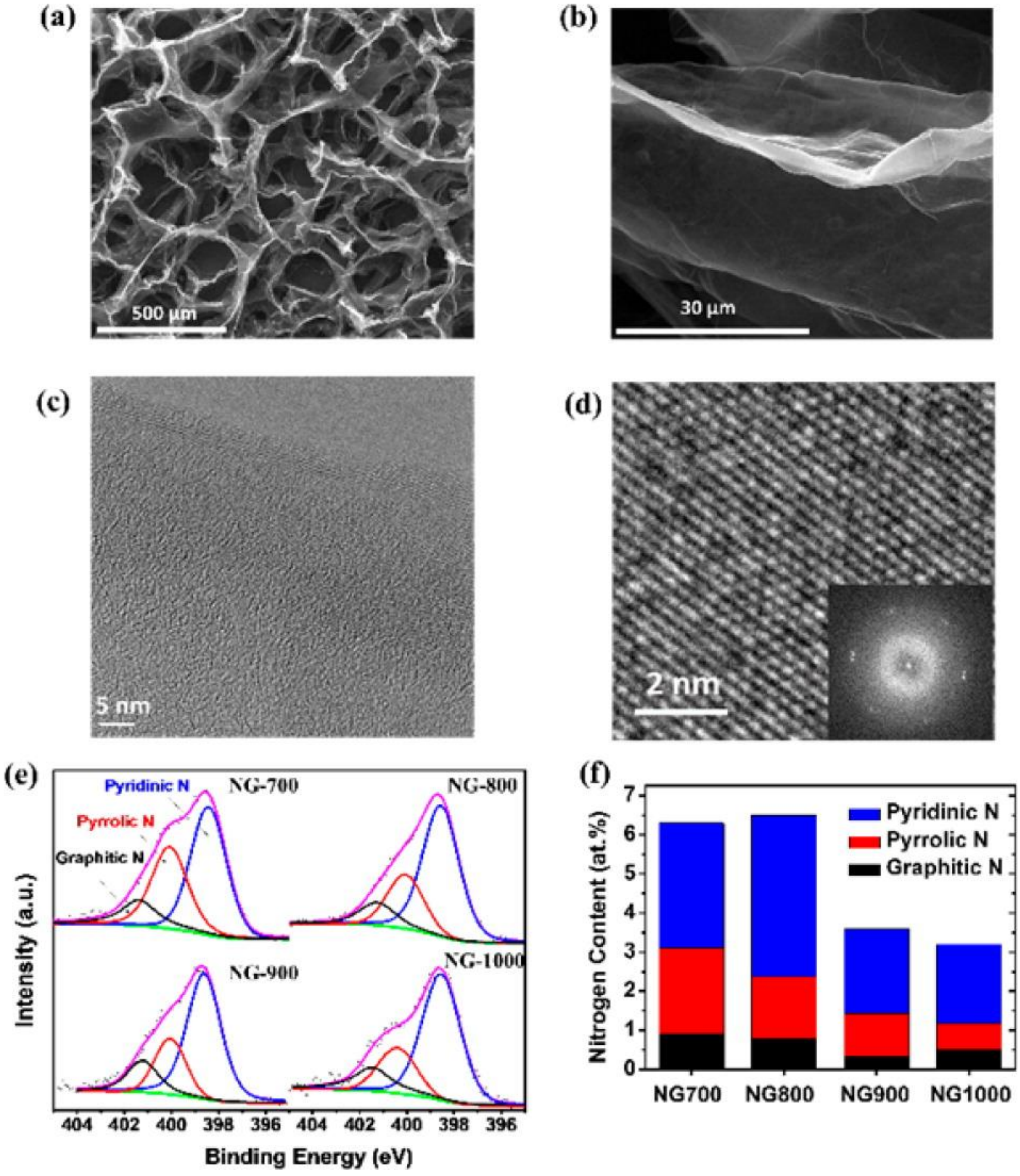

**Figure 4.2.** Physical characterization of N-doped graphene foam. (a) A SEM image showing a representative graphene foam with an open frame structure. (b) High magnification SEM image of a NG-800 sheet. (c) TEM image of a NG-800 sheet. (d) High resolution TEM image of NG-800 sheet, and inset is the FFT pattern. (e) XPS of N 1s. (f) N content distribution as a function of different doping temperatures.

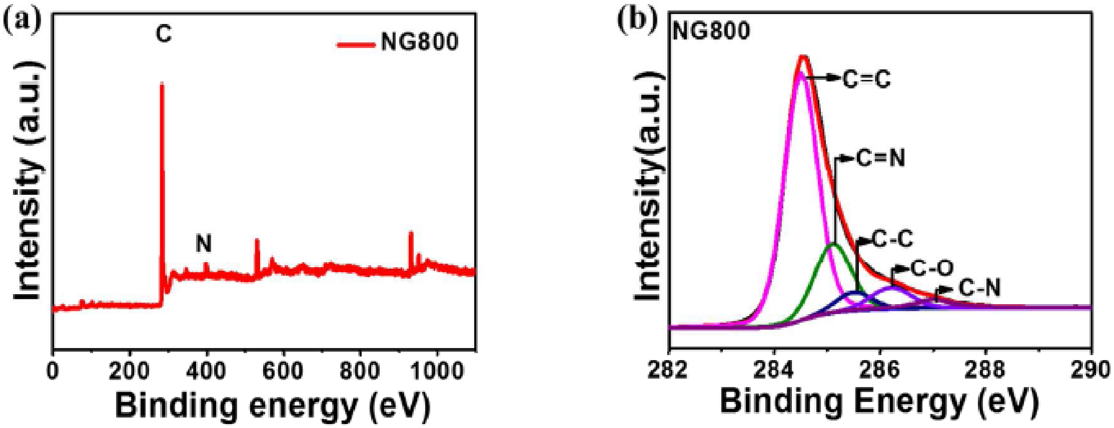

**Figure 4.3.** A representative XPS of NG-800. (a) Survey scan and (b) fine scan of C 1s.

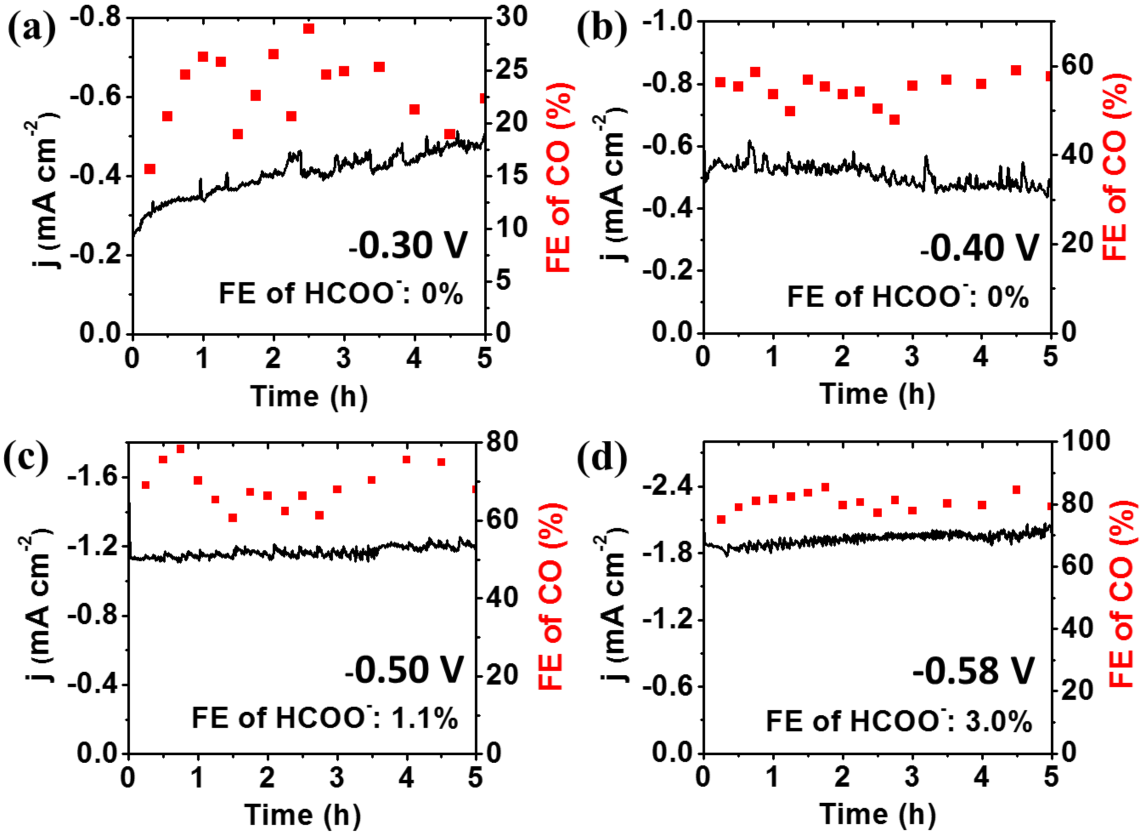

**Figure 4.4.** Performance of NG-800 for $CO_2$ reduction over long-term operation. Total current density versus time (–, left axis) and FE for CO production versus time (●, right axis) in 0.1 M $KHCO_3$ (pH 6.8 after $CO_2$ saturation) at (a) -0.30, (b) -0.40, (c) -0.50 V and (d) -0.58 V versus RHE.

The $CO_2$/CO equilibrium potential is −0.11 V versus RHE, and therefore, -0.3 V corresponds to an overpotential of -0.19 V for CO production. The FE for CO increases to ~ 60% with a cathodic shift of applied potential to -0.40 V, and further increases to ~70% at -0.50 V **(Figure 4.4b and c)**. The FE for CO reaches ~ 85% and j achieves a value ~ -1.8 mA $cm^{-2}$ at -0.58 V corresponding to an overpotential of -0.47 V **(Figure 4.4d)**. The NG-800 needs a smaller overpotential than the most selective polycrystalline metal catalysts, e.g. Au and Ag, for achieving the similar FE (~85%) for CO formation.[5, 7, 11, 26]

In addition, NG-800 exhibits stable performance towards CO production than polycrystalline metal catalysts.[5] $HCOO^-$ formation was observed at -0.50 V, with FE of only 1% **(Figure 4.4c)**, which slightly increased to ~ 3% at -0.58 V. The performance results clearly show that NG-800 enables $CO_2$ reduction via a two-electron path with a high selectivity towards CO formation. The comparison of catalytic activity towards $CO_2$ reduction among various NG catalysts synthesized at different temperatures is shown in **Figure 4.5**. A high selectivity towards CO production is also observed with other NG catalysts. NG-800 exhibits the highest activity towards $CO_2$ reduction, catalyzing CO formation at the lowest overpotential (-0.19 V) followed by NG-700 (-0.39 V), NG-900 (-0.47) and NG-1000 (-0.67 V). In addition, NG-800 displays a maximum FE for CO ~85% at a low overpotential -0.47 **(Figure 4.5a)**. The same trend is observed for the onset overpotential for $HCOO^-$ production. NG-800 shows the highest FE for $HCOO^-$ among all other NG catalysts **(Figure 4.5b)**.

**Table 4.1.** Apparent exchange current density of N-doped graphene, N-doped CNTs, and metal electrodes

| Electrode | Capacitance (μF) | $j_0$ normalized to geometric area (A/cm$^2$) | $j_0$ normalized to capacitance (A/F) |
|---|---|---|---|
| Carbon paper | 10 | - | - |
| Pristine graphene | 300 | - | - |
| NG-800 | 308 | 2.36E-05 | 0.29 |
| NG-700 | 299 | 2.05E-05 | 0.26 |
| NCNT | 190 | 1.33E-05 | 0.25 |
| Au powder | 152 | 1.05E-05 | 0.26 |
| Ag powder | 189 | 6.63E-06 | 0.13 |

As a benchmark, $CO_2$ reduction was performed on pristine 3D graphene foam under same conditions. Neither CO nor $HCOO^-$ is detected on a pristine graphene electrode, while exclusive $H_2$ evolution is observed in the same potential range. The kinetics for CO formation on these NG catalysts was examined using a Tafel plot (log $j_{CO}$ vs. η) analysis **(Figure 4.6)**. The NG-800 catalyst exhibits the lowest magnitude of Tafel slope ~222 mV/dec in a low overpotential regime of -0.17 V to -0.50 V, reflecting the fastest kinetics for CO formation. In addition, NG-800 possesses a Tafel slope similar with Au and Ag nanoparticles[11], suggesting an identical reaction mechanism for $CO_2$ reduction on these catalysts. The double layer capacitance was estimated from cyclic voltammogram under different scan rates to evaluate the electrochemical surface area of the electrodes. The NG-800 electrode exhibits a larger apparent exchange current density normalized to double layer capacitance (0.29 A/F) than Ag nanoparticles electrode (0.13 A/F), but comparable to Au particles electrode (0.26 A/F). In addition, with the comparable N distribution and content, the NG-800 electrode owns the similar apparent exchange current density to NCNTs electrode (**Table 4.1**).

**Defect Structure – Activity Relationship:** In order to understand the correlation between catalytic activity and N-defects, the trend in maximum FE for CO along with its corresponding potential versus concentrations of different N species in various NG catalysts is investigated **(Figure 4.5c)**. The maximum FE for CO increases and the corresponding potential shifts anodically as the pyridinic-N content increases, whereas no such a trend is observed for pyrrolic- and graphitic-N. These results suggest pyridinic-N is the most active site for $CO_2$ reduction though the contribution from other N-defects can't be completely ruled out. The determination of the most active site of pyridinic-N in NG is a further step forward compared to NCNTs where the highly active defect is not easily distinguishable between pyridinic- and graphitic-N due to the coupled effect of curvature or tube diameter.[27] It's worth pointing out that the selectivity towards target product of CO is independent on the electrochemical active surface area (ECSA), which is similar to the previous finding in the case of NCNTs.[27] The pristine NG, NG-700 and NG-800 electrodes have the similar ECSA indicated by the double layer capacitance (**Table 4.1**). In addition, they have identical gas permeability suggesting quite equivalent accessibility of gas reactant to the surface area (**Table 4.2**). However, pristine graphene electrode exclusively leads to off-pathway hydrogen evolution reaction (HER) in contrast to a highly selective to $CO_2$ reduction reaction (CRR) on NG electrodes. Moreover, NG-800 catalyzes CRR with higher selectivity to CO production and lower overpotential than NG-700, due largely to a higher pyridinic-N concentration. These comparisons further reveal that CRR activity depends on the N bonding type and the correspondent content.

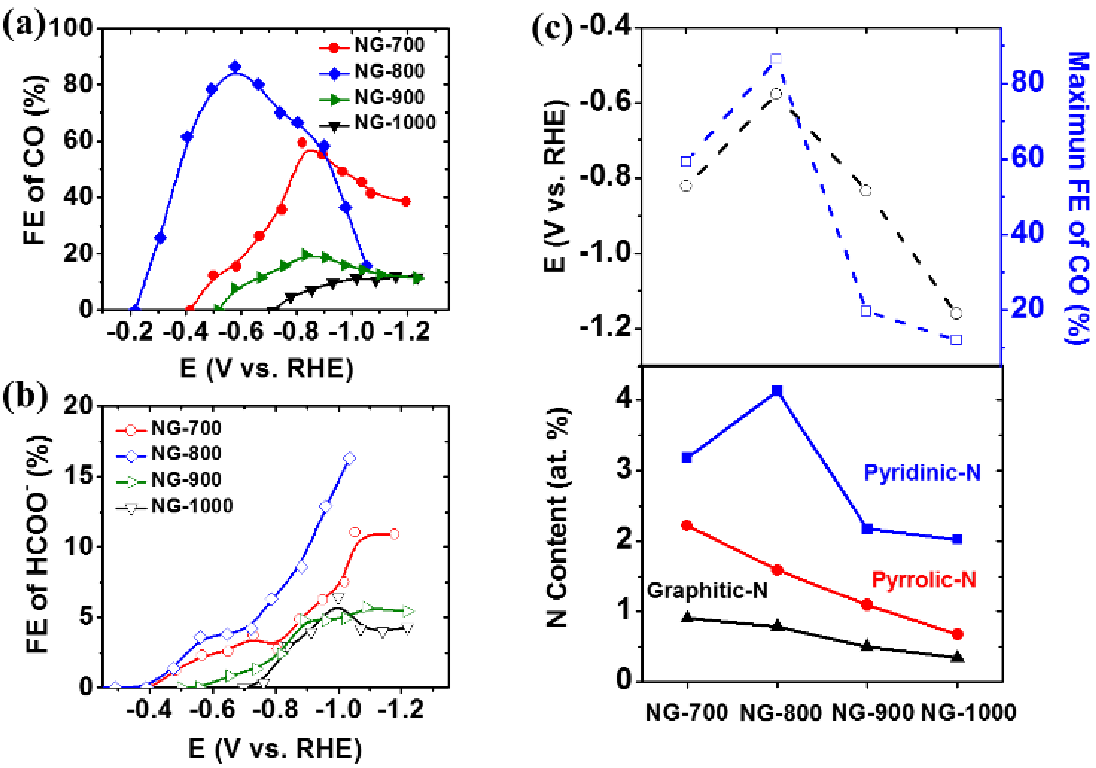

**Figure 4.5.** Comparison of the electrocatalytic activities of nitrogen-doped graphene with doping temperature ranging from 700 to 1000 °C. (a) Faradaic efficiency of CO vs potential. (b) Faradaic efficiency of HCOO$^-$ vs potential. (c) Maximum Faradaic efficiency of CO and its corresponding potential versus N functionality content.

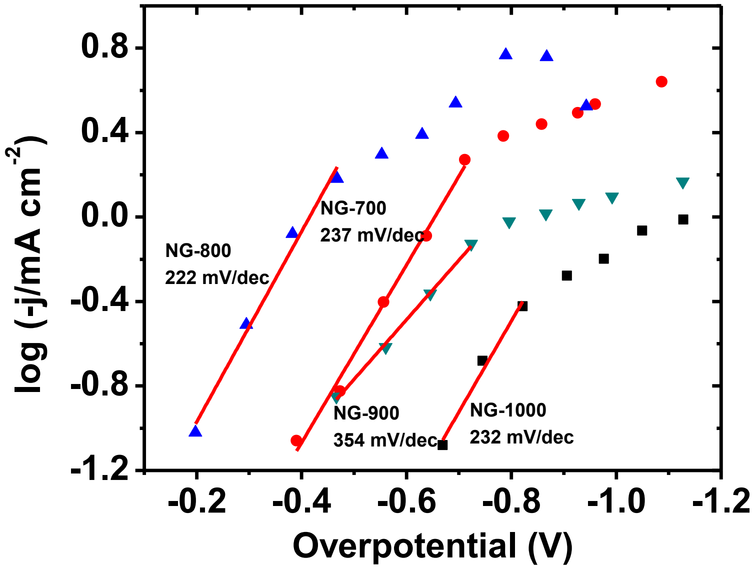

**Figure 4.6.** Tafel plots of NG electrodes for $CO_2$ reduction

**Table 4.2.** Gas permeability of various electrodes measured at a compression ratio of 10%.

| **Electrode** | **Gas permeability (×$10^{-12}$ $m^2$)** |
|---|---|
| Carbon gas diffusion layer | 6.2 |
| Pristine graphene | 3.6 |
| NG-700 | 2.9 |
| NG-800 | 3.2 |
| NG-900 | 3.3 |
| NG-1000 | 3.6 |
| Au powder | 4.2 |
| Ag powder | 3.9 |

**Mechanistic Insights:** The role of different N moieties towards $CO_2$ reduction reaction (CRR) was further examined using density functional theory (DFT) calculations based on computational hydrogen electrode (CHE) model.[28, 29, 30] A 5×6 graphene with 60 carbon atoms was applied in the first principles simulations doped by graphitic, single-pyridinic, triple-pyridinic and pyrrolic N respectively. The reaction mechanism of electro-reduction of $CO_2$ to CO was considered through the adsorbed intermediates, COOH* and CO* on pristine as well as N-doped graphene **(Figure 4.7)**. Similar intermediates have been proposed for the electroreduction of $CO_2$ on late transition metals like Au, Pt, and Cu.[28, 29, 30] The corresponding free energy diagram for the lowest energy pathways of $CO_2$ reduced to CO through this scheme is shown in **Figure 4.7a**. The overpotential originates from the uphill barrier of the first proton-coupled electron transfer step forming COOH* for pristine graphene, graphitic, triple-pyridinic and single-pyridinic N doped graphene. After adsorption of COOH*, the free-energy pathway becomes thermodynamically downhill for the transfer of the second proton-coupled electron to form adsorbed CO*. The pristine graphene has the highest free energy barrier for the first step of COOH* adsorption which hinders CRR. The CRR activity is, however, enhanced by introducing the electronegative N atoms in the graphitic lattice. The COOH* bonds to N defects at pyridinic and pyrrolic N sites while the positively charged carbon atom adjacent to nitrogen is the active site for graphitic N (**Figure 4.7b**). The free energy barrier for COOH* adsorption drops dramatically with N defects because of dangling N bonds that binding intermediate COOH* fragment much stronger. Triple-pyridinic N lowers the barrier of COOH* adsorption step to the most followed by single-pyridinic and graphitic N. Interestingly, $COOH^*$ adsorption at a pyrrolic N-defect site is exergonic. However, the release of chemisorbed CO from pyrrolic-N through a non-electrochemical desorption step possesses an energy barrier of ~ 0.6 eV, which is independent of applied voltage.

To fully unravel the reactivity of N moieties, the competing hydrogen evolution reaction (HER) is taken into consideration due to its more favorable thermodynamics over CRR. The active sites for HER are identical with CRR. The free energy diagram of HER suggests a strong adsorption of H* on triple-pyridinic, pyrrolic and single-pyridinic N. The H* bonding to single-pyridinic N is easy to desorb since single-pyridinic N exhibits a relatively lower barrier for Heyrovsky step than that for COOH* adsorption. As a result, single-pyridinic N can function as an active site for CRR with a relative low uphill barrier for COOH* adsorption. However, triple-pyridinic and pyrrolic N tend to be passivated by strongly bonded H*.

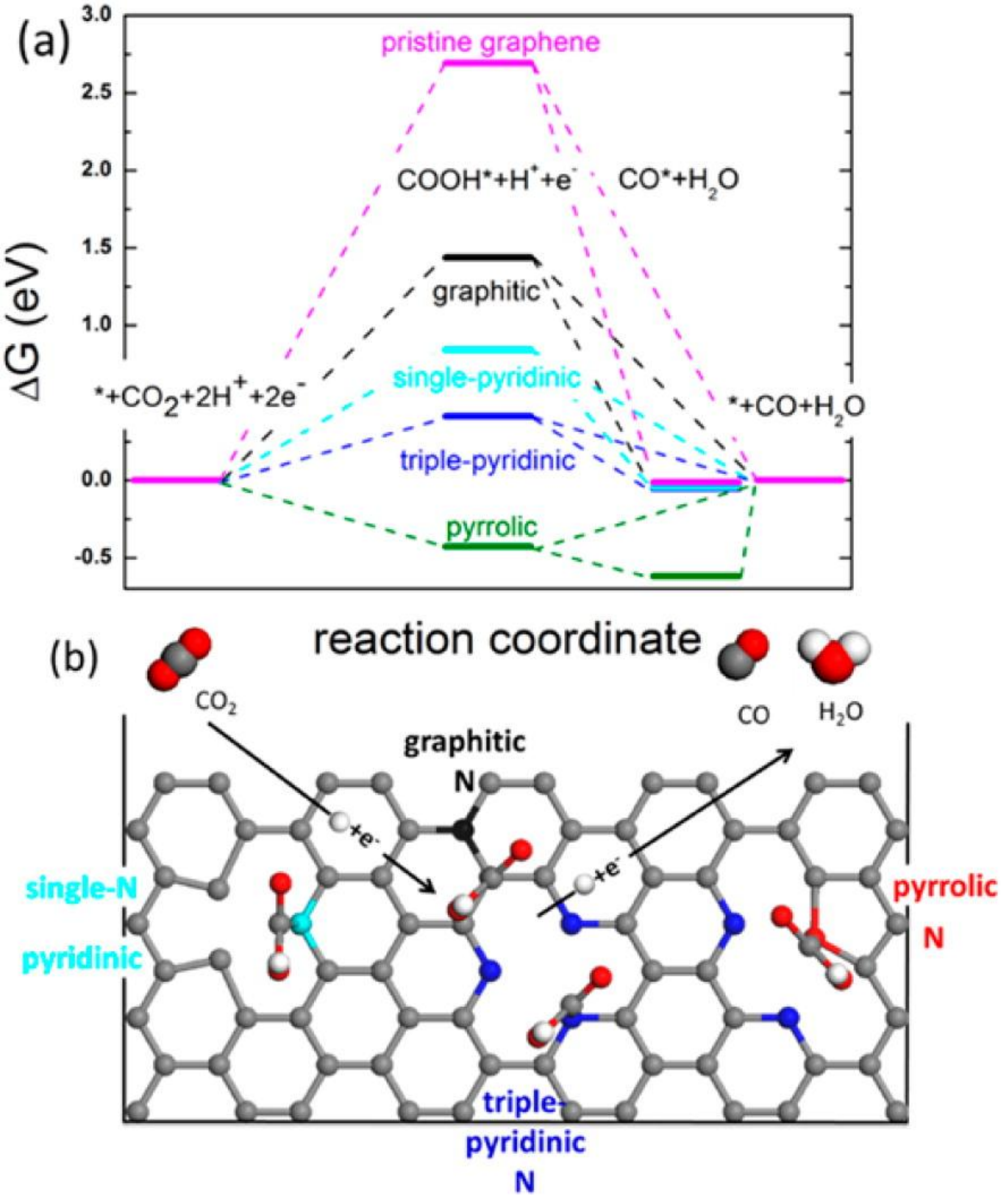

**Figure 4.7.** DFT modeling of electrocatalysis of $CO_2$ on NG. (a) Free energy diagram of electrochemical reduction of $CO_2$ to CO on NG and (b) schematic of N configuration and $CO_2$ reduction pathway. DFT calculations were done by Mingjie Liu at Rice University.

To suppress the passivation and simultaneously enhance the CRR, the choice of electrolyte, e.g., 0.1 M $KHCO_3$ (pH ≈ 6.8 after $CO_2$ saturation) in this case, is significant to ensure a local neutral environment near the electrode surface. Triple-pyridinic N becomes available for actively catalyzing CRR with the lowest uphill free energy barrier of COOH* adsorption. Without H* passivation, pyrrolic N might also be active for CRR in an alternative pathway through directly protonating COOH* to form CO gas and $H_2O$, since this protonation step requires much lower barrier (-0.5 eV) than that for Heyrovsky step for $H_2$ formation (-2.0 eV). Considering both CRR and HER, pyridinic N (including triple-and single-pyridinic N) is the relative higher active site for CO formation consistent with the experimental results (**Figure 4.5c**).

## 4.4 Conclusions

In summary, N-doped 3D graphene foams are synthesized with different N-defect structures and content through a post-doping process at various temperatures. These N-defects catalyze $CO_2$ reduction to CO at low overpotentials with high selectivity and long durability in contradiction to pristine graphene, which displays no activity. A combination of experimental and theoretical investigations reveals distinct catalytic activity of different N functionalities. The pyridinic-N defects exhibit the highest catalytic activity by lowering the free energy barrier to form adsorbed COOH, eventually leading to CO formation. This work demonstrates the directions for future efforts to deliberately incorporate high pyridinic-N content in carbon nanostructures as metal-free electrocatalysts for $CO_2$ reduction.

## References

1. Li CW, Kanan MW. $CO_2$ Reduction at Low Overpotential on Cu Electrodes Resulting from the Reduction of Thick $Cu_2O$ Films. *J Am Chem Soc* **134**, 7231-7234 (2012).

2. Li CW, Ciston J, Kanan MW. Electroreduction of carbon monoxide to liquid fuel on oxide-derived nanocrystalline copper. *Nature* **508**, 504-507 (2014).

3. Kaneco S, Iiba K, Hiei N-H, Ohta K, Mizuno T, Suzuki T. Electrochemical reduction of carbon dioxide to ethylene with high Faradaic efficiency at a Cu electrode in CsOH/methanol. *Electrochim Acta* **44**, 4701-4706 (1999).

4. Le M, Ren M, Zhang Z, Sprunger PT, Kurtz RL, Flake JC. Electrochemical Reduction of $CO_2$ to $CH_3OH$ at Copper Oxide Surfaces. *J Electrochem Soc* **158**, E45-E49 (2011).

5. Chen Y, Li CW, Kanan MW. Aqueous $CO_2$ Reduction at Very Low Overpotential on Oxide-Derived Au Nanoparticles. *J Am Chem Soc* **134**, 19969-19972 (2012).

6. Rosen BA, *et al.* Ionic Liquid–Mediated Selective Conversion of $CO_2$ to CO at Low Overpotentials. *Science* **334**, 643-644 (2011).

7. Lu Q, *et al.* A selective and efficient electrocatalyst for carbon dioxide reduction. *Nat Commun* **5**, (2014).

8. Zhu W, *et al.* Monodisperse Au Nanoparticles for Selective Electrocatalytic Reduction of $CO_2$ to CO. *J Am Chem Soc* **135**, 16833-16836 (2013).

9. Kumar B, *et al.* Renewable and metal-free carbon nanofibre catalysts for carbon dioxide reduction. *Nat Commun* **4**, (2013).

10. Zhang S, *et al.* Polyethylenimine-Enhanced Electrocatalytic Reduction of $CO_2$ to Formate at Nitrogen-Doped Carbon Nanomaterials. *J Am Chem Soc* **136**, 7845-7848 (2014).

11. Wu J, *et al.* Achieving Highly Efficient, Selective and Stable $CO_2$ Reduction on Nitrogen Doped Carbon Nanotubes. *ACS nano*, (2015).

12. Wu J, *et al.* Nitrogen-Doped Graphene with Pyridinic Dominance as a Highly Active and Stable Electrocatalyst for Oxygen Reduction. *ACS Appl Mater Interfaces* **7**, 14763-14769 (2015).

13. Wu J, Risalvato FG, Sharma PP, Pellechia PJ, Ke F-S, Zhou X-D. Electrochemical Reduction of Carbon Dioxide II. Design, Assembly, and Performance of Low Temperature Full Electrochemical Cells. *J Electrochem Soc* **160**, F953-F957 (2013).

14. Wu J, *et al.* Achieving Highly Efficient, Selective and Stable $CO_2$ Reduction on Nitrogen Doped Carbon Nanotubes. *ACS nano* **9**, 5364–5371 (2015).

15. Wu J, Risalvato FG, Ke F-S, Pellechia P, Zhou X-D. Electrochemical reduction of carbon dioxide I. Effects of the electrolyte on the selectivity and activity with Sn electrode. *J Electrochem Soc* **159**, F353-F359 (2012).

16. Perdew JP, Burke K, Ernzerhof M. Generalized Gradient Approximation Made Simple. *Phys Rev Lett* **77**, 3865-3868 (1996).

17. Nørskov JK, *et al.* Origin of the overpotential for oxygen reduction at a fuel-cell cathode. *The Journal of Physical Chemistry B* **108**, 17886-17892 %@ 11520-16106 (2004).

18. Peterson AA, Abild-Pedersen F, Studt F, Rossmeisl J, Nørskov JK. How copper catalyzes the electroreduction of carbon dioxide into hydrocarbon fuels. *Energy & Environmental Science* **3**, 1311-1315 (2010).

19. Chen Z, Ren W, Gao L, Liu B, Pei S, Cheng HM. Three-dimensional flexible and conductive interconnected graphene networks grown by chemical vapour deposition. *Nature materials* **10**, 424-428 (2011).

20. Hao Y, *et al.* Probing Layer Number and Stacking Order of Few-Layer Graphene by Raman Spectroscopy. *Small* **6**, 195-200 (2010).

21. Qu L, Liu Y, Baek J-B, Dai L. Nitrogen-Doped Graphene as Efficient Metal-Free Electrocatalyst for Oxygen Reduction in Fuel Cells. *ACS Nano* **4**, 1321-1326 (2010).

22. Ratso S, *et al.* Highly active nitrogen-doped few-layer graphene/carbon nanotube composite electrocatalyst for oxygen reduction reaction in alkaline media. *Carbon* **73**, 361-370 (2014).

23. Sharifi T, Hu G, Jia X, Wågberg T. Formation of Active Sites for Oxygen Reduction Reactions by Transformation of Nitrogen Functionalities in Nitrogen-Doped Carbon Nanotubes. *ACS Nano* **6**, 8904-8912 (2012).

24. Jacobson IA, Heady HH, Dinneen GU. Thermal Reactions of Organic Nitrogen Compounds. I. 1-Methylpyrrole. *J Phys Chem* **62**, 1563-1565 (1958).

25. Arrigo R, Havecker M, Schlogl R, Su DS. Dynamic surface rearrangement and thermal stability of nitrogen functional groups on carbon nanotubes. *Chem Commun*, 4891-4893 (2008).

26. Feng X, Jiang K, Fan S, Kanan MW. Grain-Boundary-Dependent $CO_2$ Electroreduction Activity. *J Am Chem Soc* **137**, 4606-4609 (2015).

27. Sharma PP, *et al.* Nitrogen-Doped Carbon Nanotube Arrays for High-Efficiency Electrochemical Reduction of $CO_2$: On the Understanding of Defects, Defect Density, and Selectivity. *Angew Chem Int Ed* **54**, 13701–13705 (2015).

28. Peterson AA, Abild-Pedersen F, Studt F, Rossmeisl J, Norskov JK. How copper catalyzes the electroreduction of carbon dioxide into hydrocarbon fuels. *Energy Environ Sci* **3**, 1311-1315 (2010).

29. Peterson AA, Nørskov JK. Activity Descriptors for $CO_2$ Electroreduction to Methane on Transition-Metal Catalysts. *J Phys Chem Lett* **3**, 251-258 (2012).

30. Hansen HA, Varley JB, Peterson AA, Nørskov JK. Understanding Trends in the Electrocatalytic Activity of Metals and Enzymes for $CO_2$ Reduction to CO. *J Phys Chem Lett* **4**, 388-392 (2013).

# Chapter 5

# Electrocatalytic Conversion of Carbon Dioxide to Fuels: A Review on the Interaction between $CO_2$ and the Liquid Electrolyte

Multiple years of climate studies have shown that the global temperature rises are closely related to the cumulative emission of greenhouse gases.[1, 2, 3, 4, 5, 6, 7, 8, 9] Indeed, since the inception of industrial revolution around the nineteenth century, human activities have tremendously increased $CO_2$ levels in earth atmosphere. The daily mean concentration of carbon dioxide in the atmosphere measured at the Mauna Loa Observatory in Hawaii was recorded above 400 parts per million for the first time on May 9th, 2013, as shown in **Figure 5.1**. A continuous accumulation of $CO_2$ has raised concerns because of the associated detrimental environmental impacts, for instance global warming, climate change, and ocean acidification. A global temperature increase by 2 – 6 ºC is estimated during the next century, which might cause a sea level rise up to 1.5 m, leading to potentially catastrophic effects.[10, 11, 12] A recent comprehensive analysis showed that an additional 0.5 ºC increase from 1.5 ºC to 2 ºC would lead to longer heat waves, greater droughts and, in the tropics, reduced crop yield and all coral reefs being put in grave danger.[13] These issues have spurred the research in $CO_2$ capture and fixation

in recent years. A carbon-neutral energy cycle can provide solutions to these problems by converting $CO_2$ to value-added products using renewable energy sources.

The electrochemical conversion of $CO_2$ has been studied for over a span of thirty years. Both metallic (e.g. silver[14, 15, 16], gold[17, 18, 19], copper[20, 21, 22, 23, 24], tin[25, 26, 27, 28, 29]) and non-metallic (metal oxides[30, 31, 32], doped carbon nanostructures[33, 34, 35, 36]) catalysts have been reported to produce various fuels (e.g. CO, HCOOH, $CH_4$, $C_2H_4$, $CH_3OH$ etc). While the catalyst structure provides the active sites, the electrolyte plays an equally important role in catalysis by interacting with the reactant and intermediate species, ultimately influencing the overall reduction reaction.[37, 38, 39, 40, 41] An example is the use of ionic liquid solvents, which provide a friendly environment stabilizing the intermediate species and eventually improve the catalytic activity.[14, 18]

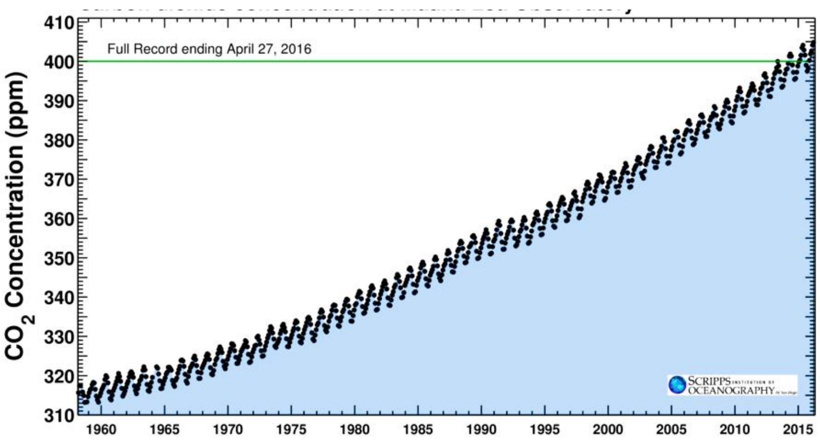

**Figure 5.1.** The Keeling curve, carbon dioxide concentrations at the Mauna Loa Observatory (Source: Scripps Institution of Oceanography)

The choice of an ionic liquid for this purpose stems from its tendency to form a complex with $CO_2$.[14] Moreover, it has shown that the product and product yield obtained in aqueous electrolyte differ from that in organics or ionic liquids that employ the same catalyst.[42] Therefore, an understanding of the interactions between a solvent and $CO_2$

molecule can shed light on properly selecting the electrolyte chemistry and tuning the product selectivity. Furthermore, these interactive forces govern $CO_2$ solubility and as a result, this insight can help develop new $CO_2$ capture schemes. The aim of this review article is to describe the interactions of $CO_2$ in three solvent systems: water, organics and ionic liquids. This knowledge provides a fundamental overview on the interactions between $CO_2$ and various species, which can be used to design novel hybrid solvent systems for $CO_2$ capture and fixation.

## 5.1 $CO_2$ in Aqueous Electrolyte

An electrolysis cell for $CO_2$ conversion based on a proton-exchange membrane fuel cell (PEMFC) requires a buffer layer to suppress hydrogen evolution reaction and consequently, promote $CO_2$ reduction at cathode.[43, 44] **Figure 5.2** shows the schematic of such cell, where an electrolyte is circulated through a buffer layer, which resides between the Nafion membrane and cathode catalyst layer. This electrolyte flowing through the buffer layer perhaps acts as a co-catalyst which significantly lowers the overpotential for $CO_2$ reduction. In addition, a flowing electrolyte can provide moderate convective mixing in comparison to stagnant electrolyte systems, which can tune the proton concentration near cathode surface, making $CO_2$ reduction feasible. This is supported by the results shown in **Figure 5.3**, where inclusion of a buffer layer significantly shifts the selectivity of the cathode towards $CO_2$ reduction. An incorporation of a thick buffer layer, however, increases the ohmic resistance of the electrolysis cell, thereby decreasing the current density for products formation from $CO_2$ reduction.

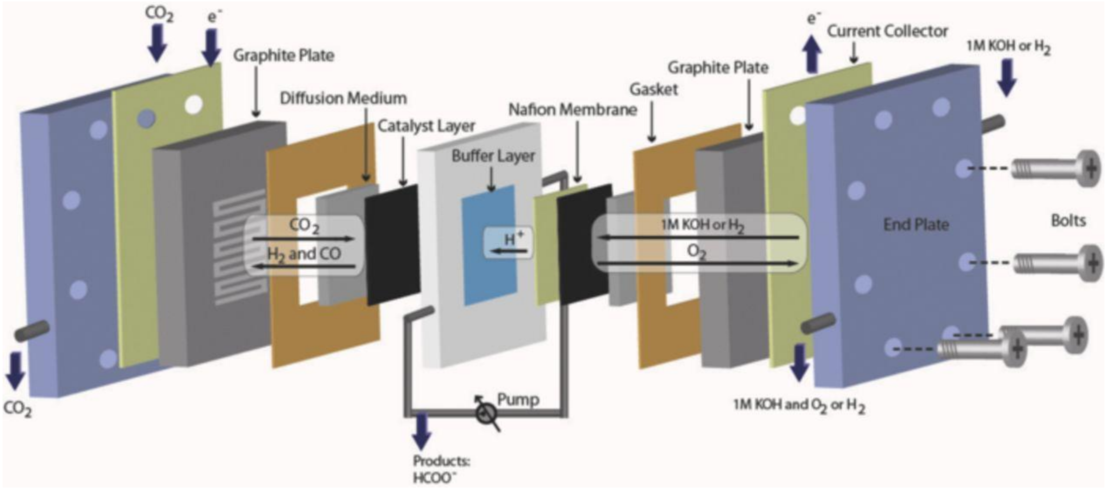

**Figure 5.2**. A schematic of the full electrochemical cell featuring a buffer layer circulating a liquid-electrolyte [44]

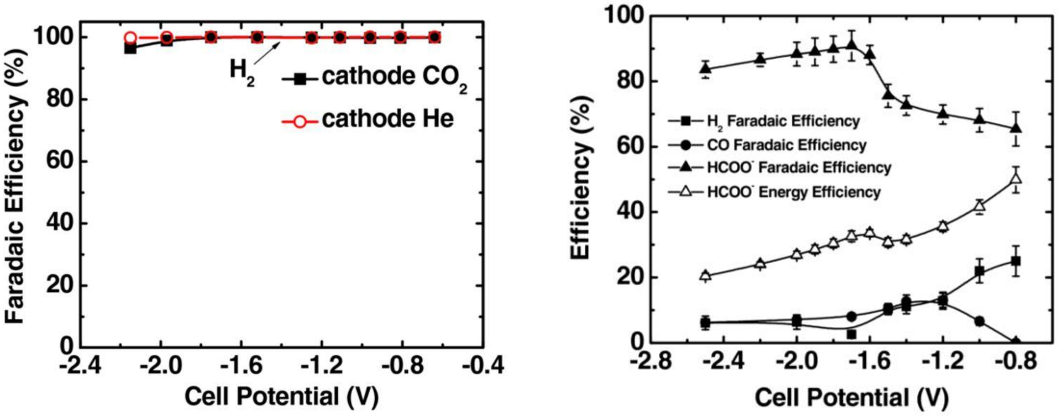

**Figure 5.3.** Performance of full electrochemical cell without (left) and with (right) a buffer layer. Anode catalyst: Pt/C; Cathode catalyst: Sn[44]

Furthermore, the type of liquid electrolyte also results in different selectivity towards formation of products from $CO_2$ reduction. Some of these reported results are listed in **Table 5.1** (see details in Chapter 1, Table 1.1).

**Table 5.1.** Products from $CO_2$ reduction in different electrolyte systems at various metal electrodes

| **Metals** | **Valence Electron Configuration** | **Electrolyte (Aqueous/Non-aqueous)** | **Major Products** | **Selectivity (Maximum Faradaic efficiency, %)** |
|---|---|---|---|---|
| Pb, Hg, Sn, In, Bi | s/sp | Aqueous | HCOOH (all) | 90 |
| | | Non-aqueous<br>(Propylene carbonate) | $(COOH)_2$ for Pb, Hg | 80 |
| | | Non-aqueous<br>(Methanol) | CO (disproportionation) for Sn | 72 |
| Cu | $4s^1$/d group | Aqueous | CO | 30 |
| | | | HCOOH | 35 |
| | | | $CH_4$ | 40 |
| | | | $C_2H_4$ | 20 |
| | | | $C_2H_5OH$ | 22 |
| | | Non-aqueous<br>(Propylene carbonate) | $CO/(COOH)_2$ | 70 |
| | | Non-aquoeus<br>(Methanol) | HCOOH | 17 |
| | | | $CH_4$ | 22 |
| | | | $C_2H_4$ | 20 |
| Ni, Pd,Pt | Fully filled d-orbital | Aqueous | CO (all) | < 10 |
| | | | HCOOH for Pd | 100 |
| | | Non-aqueous | CO/(COO | 60 |

|  |  |  |  |  |
|---|---|---|---|---|
|  |  | (Propylene carbonate) | H)$_2$ |  |
| Fe, Co, Rh, W, Ir, Re | Partly filled d-orbital | Aqueous | $H_2$ (all) | 100 |
|  |  | Non-aqueous (Methanol) | CO/(COOH)$_2$ for Re | 87 |
| Zn, Ag, Au, Cd | s only/s$^1$ | Aqueous | CO (disproportionation) for Zn, Ag, Au | 94 |
|  |  | Non-aqueous (Methanol) | CO for Zn, Ag, Au | 70 |
|  |  | Non-aqueous (1-Ethyl-3-methylimidazolium tetrafluoroborate) | CO for Ag | 100 |

The major questions that however, remain unanswered are: (1) Whether $CO_2$ reduction happens on gaseous or solvated $CO_2$ molecules; carbonates or bicarbonates (for the case of water)? (2) How does a liquid solvent act as co-catalyst for this reaction? (3) How does the solvent system interact with the intermediates formed during $CO_2$ reduction, thereby, influencing selective formation of different products? Therefore, it is of paramount importance to investigate how the presence of solvent molecules reduces the activation barrier for $CO_2$ reduction. This would require an understanding of the type of fundamental interactions between solvent and $CO_2$ molecules.

**$CO_2$ Speciation in Water:** $CO_2$ concentration in water at saturated conditions is ~ 38 mM at 20°C and ambient pressure.[54] This concentration is governed by Henry's law and thus, increases at higher $CO_2$ pressures. Upon dissolution in water, $CO_2$ exists in three inorganic forms: $CO_2$ (aq.), $HCO_3^-$ and $CO_3^{2-}$. The fourth form, i.e., carbonic acid ($H_2CO_3$) is also present, however, the concentration of $H_2CO_3$ is much lower than that of $CO_2$ (aq) (< 0.3%).[55] The dissolved $CO_2$ reacts with $H_2O$ to form $H_2CO_3$, which dissociates to form $HCO_3^-$ and $CO_3^{2-}$; species $CO_2$ (aq), $HCO_3^-$ and $CO_3^{2-}$ are in equilibrium with each other as represented by the **Equations [1]-[3]**. The sum of the concentrations of dissolved forms of $CO_2$ is termed as the dissolved inorganic carbon (DIC) content (**Eq. [4]**). The carbonate alkalinity (CA), on the other hand, represents the charge balance inside an aqueous medium. The carbonate ion ($CO_3^{2-}$) is accounted twice for calculating CA (**Eq. [5]**), because it has a double negative charge.[55]

$$CO_2 + H_2O \overset{K_1}{\Leftrightarrow} HCO_3^- + H^+ \overset{K_2}{\Leftrightarrow} CO_3^{2-} + 2H^+ \qquad [1]$$

$$K_1 = \frac{[HCO_3^-][H^+]}{[CO_2]} \qquad [2]$$

$$K_2 = \frac{[CO_3^{2-}][H^+]}{[HCO_3^-]} \qquad [3]$$

$$DIC = \sum CO_2 = [CO_2] + [HCO_3^-] + [CO_3^{2-}] \qquad [4]$$

$$CA = [HCO_3^-] + 2[CO_3^{2-}] \qquad [5]$$

The expressions for $K_1$ and $K_2$ (**Equations [2] and [3]**) illustrate the equilibrium dependence on the pH of the aqueous solution. **Figure 5.4** shows the variation in concentration of $CO_2$, $HCO_3^-$ and $CO_3^{2-}$ species with pH.

**Table 5.2.** Thermodynamic Gibbs energy of formation of various epecies at 25°C and 1 atm[57, 58]

| **Species** | **$\Delta G_f^0$ (KJ/mol)** |
|---|---|
| $CO_2$(g) | -394 |
| $H_2O$(l) | -237.14 |
| $CO_2$(aq) | -386 |

The dissolution of solute in a particular solvent takes places via two steps. The intermolecular bonds between the solvent molecules, which are responsible for holding them together, are broken, and a similar process takes place for solute molecules. This first step requires input energy. In the second step, the solvent and solute molecules can interact through various forces (e.g. H-bonding, ion-dipole etc.), thereby releasing energy resulting in dissolution. A larger negative value of standard Gibbs free energy of formation for $CO_2$ reflects its high stability. However, the Gibbs free energy lowers in magnitude by 8 KJ/mol (~ 0.1 eV/molecule) for solvated $CO_2$ in comparison to $CO_2$ in the gas phase, suggesting a higher reactivity of solvated $CO_2$, i.e., $CO_2$(aq) than $CO_2$(g).

**$CO_2$ Solubility in Water:** A model addresses the solubility of $CO_2$(g) in water by calculating the chemical potentials of $CO_2$ in gas and liquid phase using equation of state (EOS) and specific interaction model respectively, consistent with experimental measurements.[59] $CO_2$ solubility in aqueous phase is determined by a balance between the chemical potential of $CO_2$ in the gas ($\mu^g_{CO2}$) and liquid phase ($\mu^l_{CO2}$).

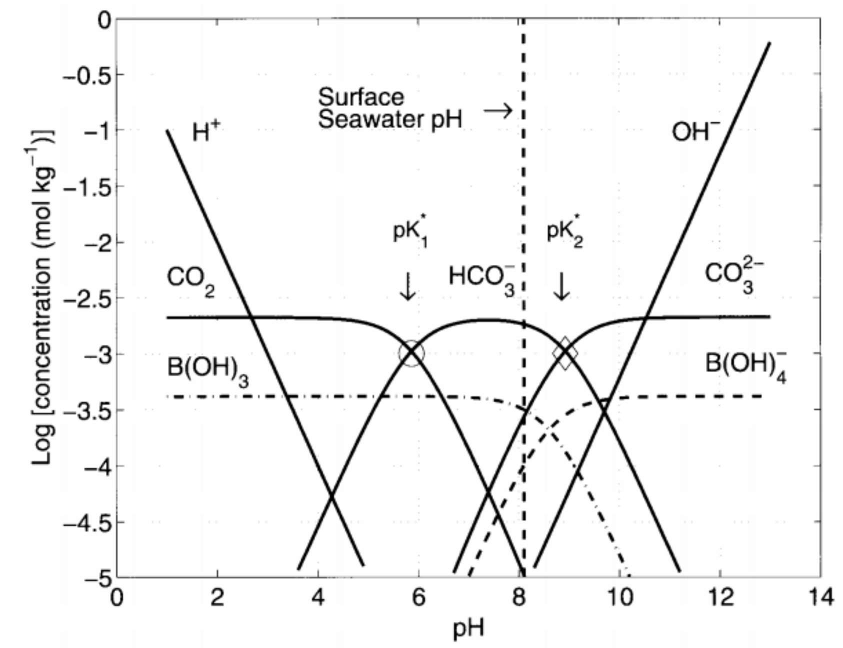

**Figure 5.4**. Variations in concentration of $CO_2$, $HCO_3^-$ and $CO_3^{2-}$ with pH of the aqueous medium. DIC = 2.1 mmol/kg, Salinity, S = 35 and T = 25 °C.[55] ($K_1^* = K_1$; $K_2^* = K_2$).

The chemical potentials of $CO_2$ in the gas and liquid phase, in turn can be related to the fugacity and activity of $CO_2$ in the gas and liquid phase respectively, as respresented by **Eqs. [6] and [7]**.

$$\mu^{g}_{CO2} = \mu^{g(0)}_{CO2} + RTlnf_{CO2} \qquad [6]$$

$$\mu^{l}_{CO2} = \mu^{l(0)}_{CO2} + RTlna_{CO2} \qquad [7]$$

The fugacity and activity of $CO_2$ can be related to mole fraction of $CO_2$ in gas and liquid phase respectively. Knowing the composition in the gas phase, the mole fraction of $CO_2$ in liquid phase is calculated. **Tables 5.3 and 5.4** show the trends in solubility of $CO_2$ with pressure and temperatures in different aqueous solutions. As expected, the solubility decreases with increase in temperature, while it increases on increasing the $CO_2$ pressure.

**Table 5.3.** Comparison of the solubility of $CO_2$ in water and water containing NaCl in different concentrations at 1 bar pressure and various temperatures[59]

| **Temperature (K)** | **Solubility (mol/kg) in water** | **Solubility (mol/kg) in 1 m NaCl aqueous solution** | **Solubility (mol/kg) in 2 M NaCl aqueous solution** |
|---|---|---|---|
| 273.15 | 0.0693 | 0.0557 | 0.0452 |
| 303.15 | 0.0286 | 0.0238 | 0.0200 |
| 333.15 | 0.0137 | 0.0116 | 0.0100 |
| 363.15 | 0.0036 | 0.0031 | 0.0027 |

**Table 5.4.** Comparison of the solubility of $CO_2$ in water and water containing NaCl in different concentrations at 303.15 K and various pressures[59]

| **Pressure (bar)** | **Solubility (mol/kg) in water** | **Solubility (mol/kg) in 1 m NaCl aqueous solution** | **Solubility (mol/kg) in 2 M NaCl aqueous solution** |
|---|---|---|---|
| 1 | 0.0286 | 0.0238 | 0.0200 |
| 5 | 0.1442 | 0.1185 | 0.0984 |
| 10 | 0.2809 | 0.2294 | 0.1895 |
| 50 | 1.0811 | 0.8729 | 0.7135 |

The solubility also decreases with increasing salt concentration in aqueous solution, a phenomenon referred to as "salting-out" effect. Because of the presence of anions and cations in the aqueous solution formed by salt dissociation, lesser water molecules interact with $CO_2$, resulting in lower dissolution. Addition of salts to fresh water increases the total number of ions in the solution, however, the ion activity decreases because of: 1) long-range electrostatic interactions, 2) ion pairing and complex formation.[55] **Figure 5.5** shows the effect of salinity, or ionic strength on the concentrations of $CO_2$, $HCO_3^-$ and $CO_3^{2-}$ species at different pH values. The relative proportion of $CO_3^{2-}$ ions increase with respect to [$CO_2$] and [$HCO_3^-$] at same pH and temperature with increasing salinity.[55]

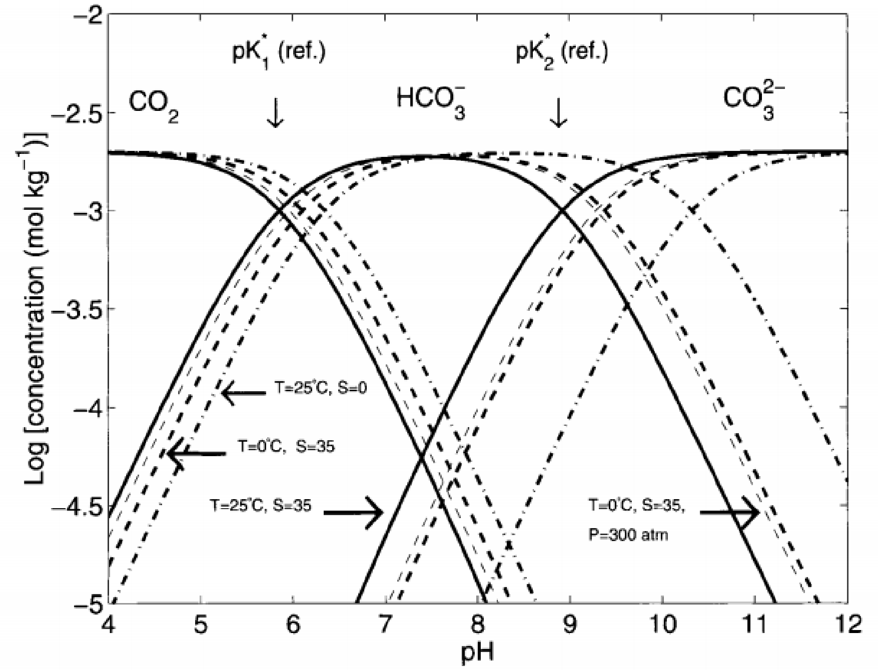

**Figure 5.5.** Illustration of the effect of temperature, pressure and salinity (ionic strength) on the concentration of $CO_2$, $HCO_3^-$ and $CO_3^{2-}$ species.[55] ($K_1^* = K_1$; $K_2^* = K_2$).

The understanding of diffusion of $CO_2$ in water is critical to build $CO_2$ capture and fixation schemes in an aqueous environment. The transport of $CO_2$ towards solid surface can be caused by convective and/or diffusive mechanisms. The convective transport mechanism become significant in cases of absorption of pure highly soluble gases, resulting in higher mass transfer rates at higher gas solubility. The convective transport can be modeled by using Maxwell-Stefan theory for mass transport, which has been validated by experimental measurements.[60] On the other hand, the diffusion coefficients are measured for $CO_2$-$H_2O$ using Taylor-Aris dispersion method.[61] This technique uses the dispersion of solute plug when injected in laminar flow to compute the diffusion coefficient of $CO_2$ in water. Axial dispersion is governed by a parabolic flow profile, which acts to disperse the solute in the longitudinal direction, while radial dispersion prevents the solute from being extended over a much larger region. As a result of these two phenomena, a Gaussian distribution function is obtained for dispersion curve once fully developed flow is attained. The dispersion coefficient in turn is related to the diffusion coefficient of $CO_2$ in water. **Figure 5.6** shows the diffusion coefficient of $CO_2$ in water as function of various temperatures and pressures. As expected the diffusion coefficient of $CO_2$ in water increases upon increasing the temperature. Importantly, the diffusion coefficient of $CO_2$ doesn't depend significantly upon pressure (14 – 45 MPa) in a temperature range between 298 and 423 K. The data obtained from experimental measurements can be described by Stokes-Einstein correlation, which is given by **Eq. [8].**[61]

$$D = \frac{k_B T}{n_{SE} \pi \mu a} \qquad [8]$$

where $n_{SE}$ is the Stokes-Einstein's number, $\mu$ is the viscosity and a is the hydrodynamic radius of solute. Furthermore, the hydrodynamic radius of $CO_2$ may show a weak dependence on temperature.[61]

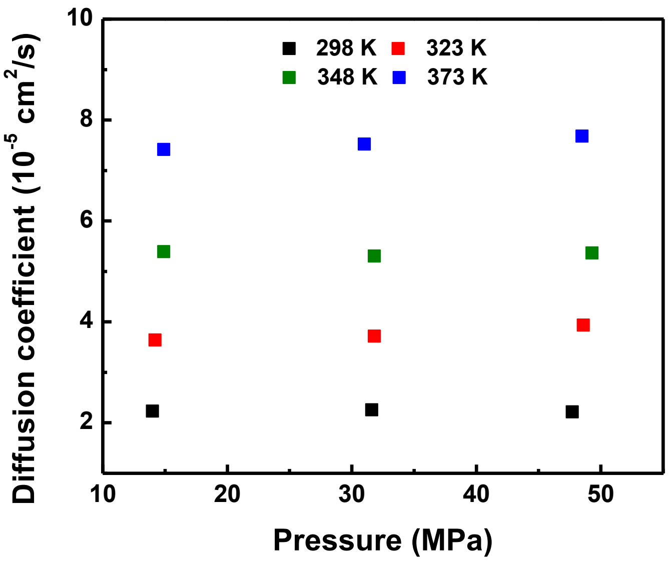

**Figure 5.6.** Diffusion coefficients of $CO_2$ in ultra-pure DI water at different temperatures and pressures[61]

**$CO_2$ Structure(s) in Water:** FTIR and Raman spectroscopy have been used to detect the presence of the different species formed by $CO_2$ dissolution in water.[54] The features in Raman spectra, including peak intensity, position, and width for the Fermi doublet of $CO_2$[56] of $CO_2$, change significantly in an aqueous environment suggesting the formation of hydrogen bonds between $CO_2$ and surrounding $H_2O$ molecules.[56] Modes of vibration for a $CO_2$ molecule are given by 3N-5; with N = 3 (number of atoms in $CO_2$), i.e., a total of 4 fundamental modes. Out of these modes, only one is Raman active. For a mode to be Raman active, a net change in polarizability of the molecule with vibration should be observed. This doublet in $CO_2$ arises because of the Fermi resonance, where two vibrational modes with the same energy and symmetry interact, thereby resulting in a shift of frequency and change in intensity of the spectrum. In addition, no symmetry breaking has been observed experimentally for $CO_2$ in an aqueous solution state.[56]

Computational studies also have shown similar results. The study of interaction between either O or C in $CO_2$ with $H_2O$ independently showed no change in C-O bond lengths.[62] The electronic structure of dissolved $CO_2$ is studied by calculating the X-ray absorption spectra using DFT. [63] The calculated near edge X-ray absorption fine (NEXAFS) carbon K-edge spectra for $CO_2$(g) and $CO_2$ (aq) are illustrated in **Figure 5.7**.[63] Both spectra exhibit a sharp feature at ~ 290.5 eV, representing the excitation of carbon 1s electron to the LUMO $2\pi_{u*}$ antibonding molecular states **(Figure 5.7)**.[63] In addition, a broad feature at ~ 310 eV is observed that shows the $4\sigma_{u*}$ resonance of $\sigma^*$ features. However, a small peak at ~ 292 eV is observed only for $CO_2$(g), representing the $3s\sigma_g$ Rydberg state[63], which is a excited electronic state that follows Rydberg's formula at very high principal quantum numbers, i.e., a state approaching ionization. The $3s\sigma_g$ state for $CO_2$(g) is very large and diffuse, which hybridizes with water molecules to form density of states with a mixed $CO_2$ $3s\sigma_g$ and $H_2O$ character.[63] This band formation is accompanied with a reduced overlap with carbon 1s orbital and therefore, 3s $\sigma_g$ peak disappears in solvated $CO_2$.[63] These results predict a difference in electronic structure of $CO_2$ (aq) and $CO_2$ (g) that likely impacts the reactivity of these species.

Ab initio molecular dynamics (AIMD) studies have investigated the interaction of $CO_2$ with water.[64] A pair correlation function illustrates the probability of finding another atom at a certain distance from another atom. The pair correlation functions between $CO_2$ and water indicate a hydrophobic arrangement of $H_2O$ molecules around $CO_2$, as shown in **Figure 5.8**. This study yields a coordination of 0.3 water molecules per oxygen, suggesting its weak hydrogen bonding with hydrogen atoms in water. The possible interaction of carbon atom (Lewis acid) in $CO_2$ with oxygen atom (Lewis base) in $H_2O$ is also reported. AIMD studies show a higher probability for finding oxygen atom in $H_2O$ near carbon atom in $CO_2$.[64]

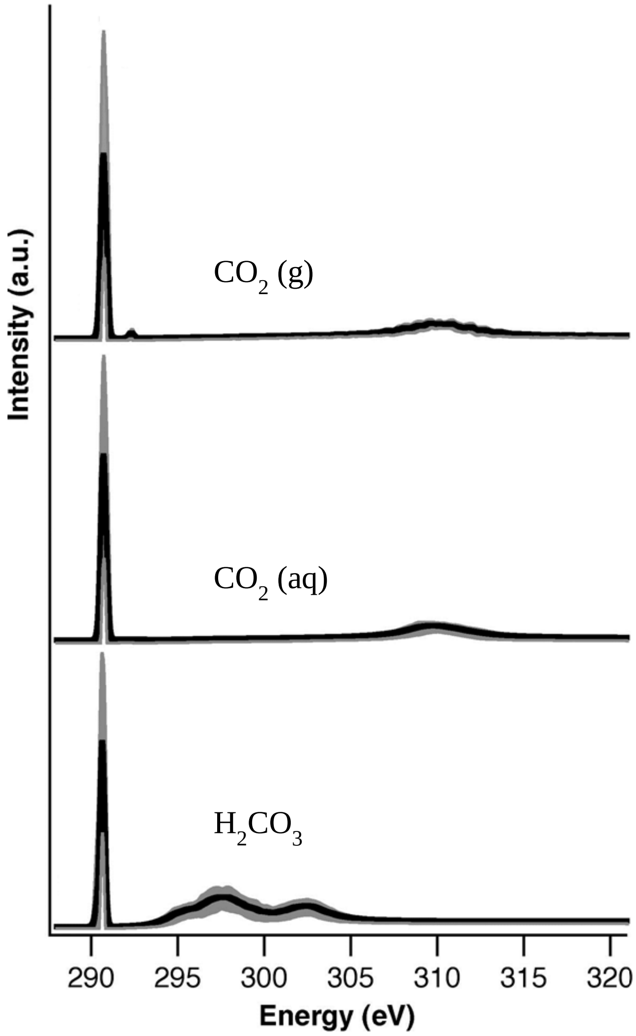

**Figure 5.7.** Calculated NEXAFS carbon K-edge spectra for various species[63] (Adapted)

The 1:1 complex of $CO_2$ and $H_2O$ is calculated to possess two different types of structures, namely the T- and H-type as predicted by ab-initio calculations.[65, 66] These two structures are calculated by analyzing the minima of potential-energy surface of the $H_2O$-$CO_2$ complex. The global minimum is attained with T-type structure, suggesting its higher thermodynamic stability than H-type.[66] Indeed, T-type structure has been illustrated by measuring the rotational spectra of the complex using molecular-beam electric resonance spectroscopy.[67]

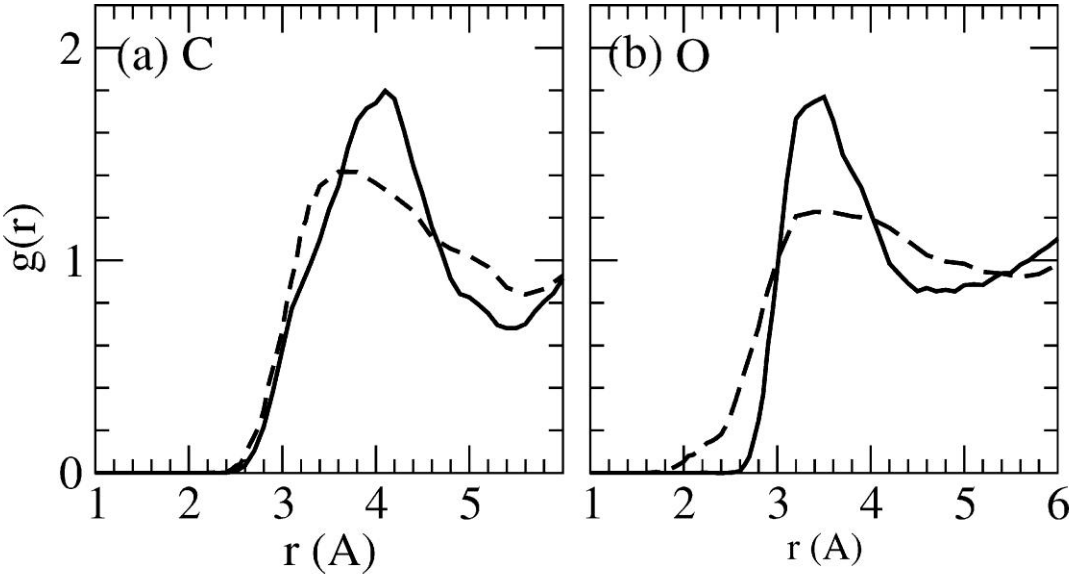

**Figure 5.8.** Pair correlation function between water and carbon dioxide. a) C atom in $CO_2$ b) O atom in $CO_2$. Solid and dashed lines refer to O and H sites in water respectively.

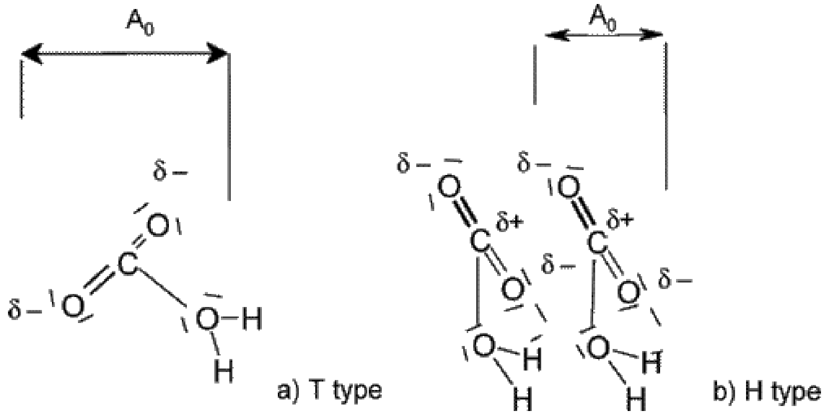

**Figure 5.9.** Structures of $CO_2$-$H_2O$ complex in a T and H-type configuration[65]

**Figure 5.9** illustrates these two structures that might be formed during $CO_2$ and $H_2O$ interaction. In the T-type configuration, the O atom of water faces the C atom and this axis is perpendicular to the OCO axis of the $CO_2$ molecule.[65] On the other hand, in the H-type, the H atom faces the O atom of $CO_2$ and the intermolecular C-O axis is tilted off by 10° with the OCO axis of the $CO_2$ molecule.[65] Importantly, the linear structure of $CO_2$ remains intact in both these configurations as observed experimentally.[56]

The molecular area of the T-type structure is higher than that of H-type. This difference in molecular area was previously exploited to determine the structure of $H_2O$-$CO_2$ complex for $CO_2$ molecule adsorbed at the $H_2O$ surface.[65] A low molecular area of 9 – 13 $A^2$/molecule is observed between temperatures 293 – 313 K, suggesting an H-type complex structure formation at the $CO_2$ (gas) – $H_2O$ (liquid) interface.[65] A decrease in molecular area of $CO_2$-$H_2O$ complex with decreasing temperature relates to the increasing interaction between hydrogen atom in $H_2O$ and oxygen atom in $CO_2$, thereby decreasing the C-O angle with OCO axis of the $CO_2$ molecule, i.e., making the structure more H-type.[65] After adsorption at the gas – liquid interface, the structure of $CO_2$-$H_2O$ complex might be transformed into T-type, during diffusion into bulk water solution owing to its higher thermodynamic stability.

Computational studies have shown different optimized structures for $CO_2$-$H_2O$ system. A difference in number of molecules in the complex formed between $CO_2$ and $H_2O$ results in dissimilar structures. The equilibrium structure of $CO_2$ and $H_2O$ dimer, i.e., $CO_2$-$H_2O$ obtained using ab intio calculations is shown in **Figure 5.10**.[68] The electron donor oxygen atom of water interacts with electron acceptor C atom of $CO_2$

molecule, leading to an intermolecular distance, $R_{O\text{-}C}$ of ~ 2.77 Å.[68] The bond angle HOH in water molecule increases by ~ 0.5-0.8 degrees after interaction with $CO_2$ molecule.[68] Interestingly, no hydrogen bond interaction is supported in the dimer ($CO_2$-$H_2O$) configuration.

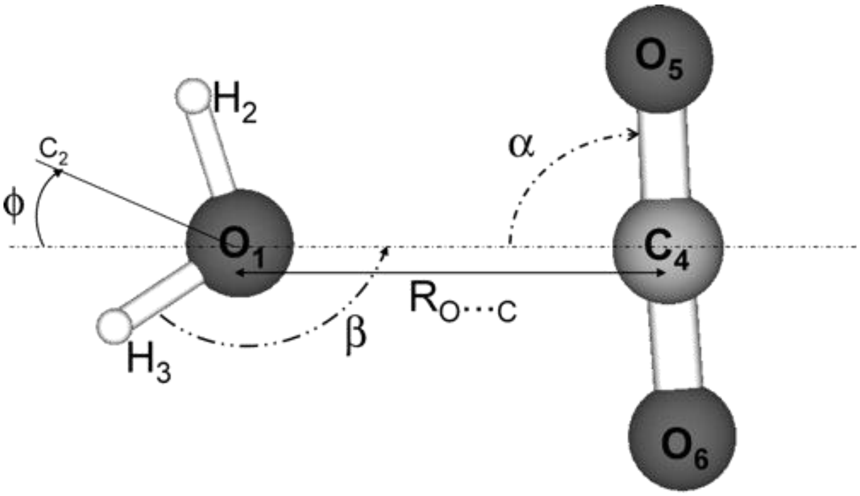

**Structure A**

**Figure 5.10.** Optimized structure of $CO_2$-$H_2O$ dimer[68]

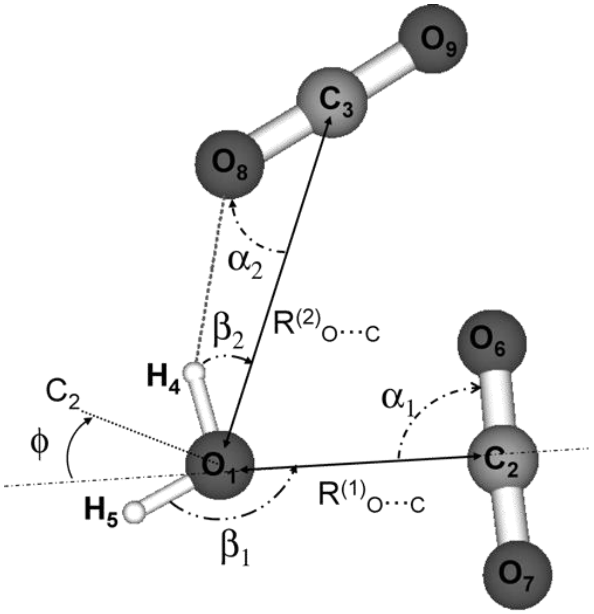

**Structure (I2) ($C_s$ symmetry)**

**Figure 5.11.** Optimized structure of $(CO_2)_2$-$H_2O$ trimer[68]

In the trimer ($(CO_2)_2$-$H_2O$) type configuration as shown in **Figure 5.11**, the electron donor oxygen atom of water interacts with the acceptor carbon atom of the nearest $CO_2$ molecule, situated at an interatomic distance $R_{C\text{-}O}^{1}$ ~ 2.76 Å.[68] Both hydrogen atoms of water are almost point away from this nearest $CO_2$. The approximate distance between carbon atom of the other $CO_2$ molecule and oxygen atom of the water molecule is ~ 3.82 Å.[68] On the other hand, the intermolecular distance between carbon atoms of $CO_2$ molecules, $R_{C\text{-}C}$ is 4.0 Å**.**[68] Importantly, a hydrogen bond is observed between the hydrogen atom of $H_2O$ molecule and oxygen atom of $CO_2$, characterized by a distance of ~ 2.13 Å.[68] This structure supports the main electron donor-acceptor (EDA) as well as a secondary hydrogen bond interaction between water and $CO_2$ molecule**.**

In an alternate method, clustering of water molecules in the presence of $CO_2$ is considered to identify the structure and stability of possible complexes formed during $CO_2$ dissolution in $H_2O$.[69] $CO_2$ binds to water molecules ultimately leading to complex formation through EDA and O-H--$O_C$ interactions. Thermodynamic calculations predict a spontaneous formation of $CO_2$-$(H_2O)_n$ (n=1,2,…,8) complex at low temperatures ($50 < T < 273$ K) as shown in **Figure 5.12**.[69] Perhaps, the Gibbs free energy change for the complex formation becomes more negative with increasing n values in the same temperature range, suggesting favorable water clustering during the complex formation. In addition, the complex formation results in a change in stretching frequencies of $CO_2$ and $H_2O$ molecules involved in the complex formation as shown in **Table 5.5**.[69] A blue shift is reported in the asymmetric stretching of the $C = O$ bond, while a red shift is calculated for the stretching frequencies of the O-H bonds attached to $CO_2$ molecule.[69] The magnitude of red and blue shifts in the stretching frequencies of the respective bonds depends on the strength of the interaction between $CO_2$ and water molecules. The formation of $CO_2(H_2O)$ without any hydrogen bond is indicated by molecular beam spectroscopy experiments.[67] Importantly, the hydrogen bond formation is observed for the case of interaction of protonated water with $CO_2$.[70] Neutral water molecules don't tend to form hydrogen bond with $CO_2$ molecule.[69] These findings suggest that formation of hydrogen bonds between $CO_2$ and $H_2O$ molecules is more likely at low pH values (pH <7).

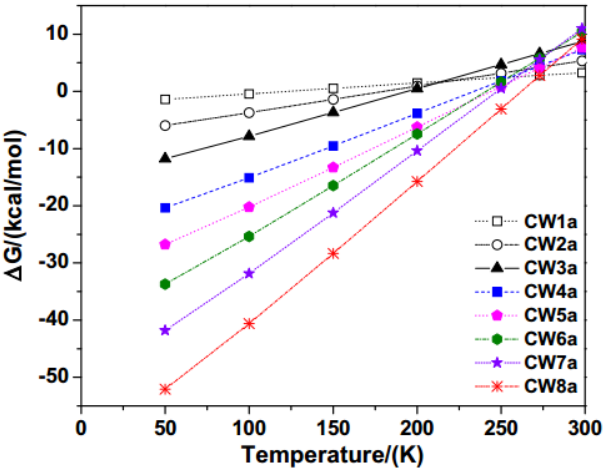

**Figure 5.12.** Gibbs free energy change with temperature for $CO_2$-$(H_2O)_n$, n=1,2,…,8[69]

**Electrocatalytic $CO_2$ Activation:** Electron-mediated $CO_2$ conversion typically proceeds through the formation of $CO_2$ radical anion intermediate, i.e., $CO_2^-$,[14, 71, 72] and therefore, an understanding interactions between $CO_2^-$ and $H_2O$ are is necessary. DFT calculations show a negative character for the two O atoms (-0.76e) and a positive change on the C atom (+0.52e).[73] Charge density calculations are supported by spin (densities) population results, which indicate a 68 and 16% electron delocalization on the C and O atoms respectively.[73] The electronic structure of $CO_2^-$ affects its chemical reactivity and interactions with $H_2O$. Negatively charged clusters of carbon dioxide, $(CO_2)_n^{-}$ have been identified, where the negative charge is delocalized over two $CO_2$ molecules for the values of n ranging from 2-5, forming a $C_2O_4^{-}$ ion core.[74, 75, 76] On the other hand, for the case of $(CO_2)_n^{-}$ ions with n ranging from 7–13, charge is localized over one $CO_2$ molecule, which can be described as $CO_2^{-} \bullet (CO_2)_{n-1}$.[76] However, for n=6, two forms of isomers with the $CO_2^{-}$ and the $C_2O_4^{-}$ ion core co-exist as indicated by photoelectron spectra measurements.[74]

**Table 5.5.** Calculated asymmetric stretching frequencies for $CO_2$ and $H_2O$ in $CO_2$-$(H_2O)_n$, n=1,2,…,8. $CO_2$ and $H_2O$ are denoted by C and W respectively[69]

| **System** | **$CO_2$** | | **$H_2O$** | |
|---|---|---|---|---|
| | Frequency ($cm^{-1}$) | Blue shift ($cm^{-1}$) | Frequency ($cm^{-1}$) | Red shift ($cm^{-1}$) |
| Free | 2374 | - | 3917 | - |
| CW1a | 2383 | 9 | 3916 | 1 |
| CW2a | 2388 | 14 | 3907 | 10 |
| CW3a | 2387 | 13 | 3880 | 37 |
| CW4a | 2387 | 13 | 3883; 3892 | 34; 25 |
| CW5a | 2387 | 13 | 3885 | 32 |
| CW6a | 2388 | 14 | 3819 | 98 |
| CW7a | 2390 | 16 | 3850 | 67 |
| CW8a | 2383 | 9 | 3874; 3900 | 43; 17 |

The addition of one water $H_2O$ or methanol $CH_3OH$ molecule to the $(CO_2)_n^{-}$ ions, however, substantially affects the stability of the ion cores in the clusters. For instance, for n=2 ion, the $CO_2^-$ can be stabilized by addition of $H_2O$ or $CH_3OH$.[77] This increased stability of $CO_2^-$ over $C_2O_4^-$ is because of hydrogen bonds formation of $CO_2^-$ with $H_2O$ or $CH_3OH$ as suggested by IR spectroscopy.[78] $CO_2$ electrocatalysis in aqueous medium has been studied over last thirty years on different metal surfaces. The effect of pH, type of salt on the catalytic activity is understood by investigating the structure of electric double layer with solvated species.[27] The presence of salts in aqueous medium change the potential at the Outer Helmholtz Plane (OHP) inside the electric double layer, which leads to difference in selective formation of products from $CO_2$ reduction **(Figure 5.13).** Aqueous electrolytes tend to decrease the charge transfer resistance for electron transfer to $CO_2$ molecule, and thereby facilitating $CO_2$ activation[79] **(Figure 5.14)**. In some cases, $CO_2$ can insert between an anion and the cation of a salt in water, which weakens the C-O bond in $CO_2$ molecule and thus facilitating electron transfer.[80] However, knowledge of solvated structures of the reactive and intermediate species formed during electrochemical reduction of $CO_2$ is not known yet. An in-depth understanding of these structures would allow for manipulating the selectivity towards formation of specific products from $CO_2$ reduction. In addition, degree of solvation (number of water molecules interacting with reactive/intermediate species) can influence the rate of proton-electron transfer process eventually leading to formation of products. A larger degree of solvation of the reactive and/or intermediate species might also increase rate of water reduction, i.e. hydrogen evolution reaction in comparison to $CO_2$ reduction. Therefore, a thorough investigation of solvation mechanism of reactive and intermediate species during $CO_2$ reduction might be necessary to elucidate the difference in selectivity.

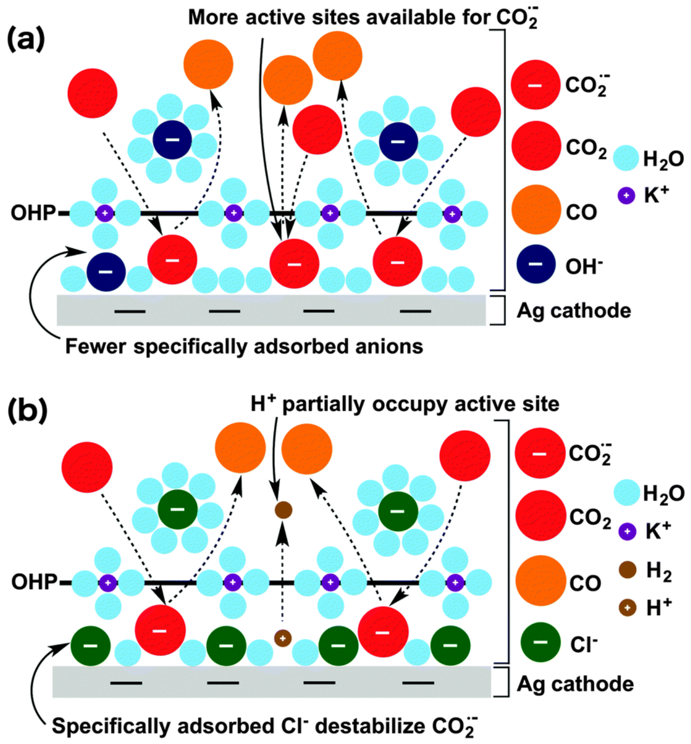

**Figure 5.13.** Schematic illustrations of processes in the double layer that play a role in the kinetics of $CO_2$ to CO conversion on a Ag cathode when using (a) KOH or (b) KCl as the electrolyte.[79]

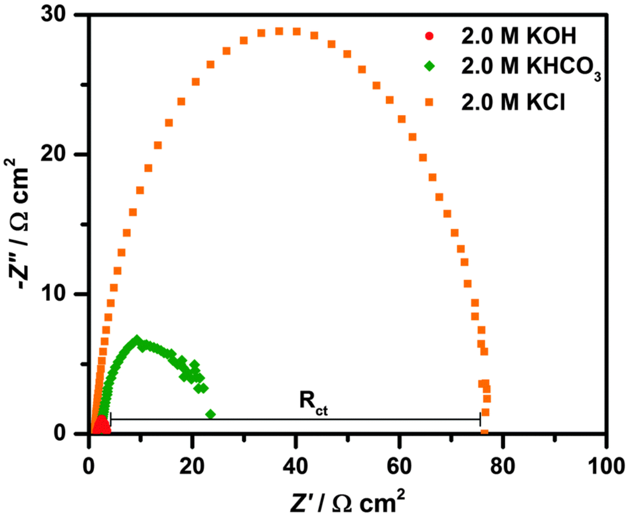

**Figure 5.14.** Nyquist plot for different electrolytes obtained via electrochemical impedance spectroscopy at a cell potential of −2.25 V.[79]

## 5.2 $CO_2$ in Organic Solvents

**$CO_2$ Solubility in Organic Solvents:** The solubility of $CO_2$ is much higher in organic solvents in comparison to water as listed in **Table 5.6**. The solubility of $CO_2$ increases with the presence of carbonyl groups in organic solvents.[81] In addition, the solubility of $CO_2$ increases in mixtures of organic solvents than in pure solvents. As the temperature is increased, the solubility of $CO_2$ decreases. The higher solubility of $CO_2$ in organic solvents makes it attractive for solvent choice for $CO_2$ electrocatalysis.

**Table 5.6.** $CO_2$ solubility in organic solvents.[81]

| **Solvent** | **Temperature (°C)** | **Solubility ($cm^3/cm^3$)** |
|---|---|---|
| Ethyl acetate | 25 | 232.96 |
| Acetone | 25 | 174.06 |
| Toluene | 0 | 135.54 |
|  | 5 | 129.89 |
|  | 25 | 81.33 |
| Dimethylformamide | 5 | 249.6 |
| Methanol | 25 | 42.7 |
| Ethanol | 25 | 58.8 |
| $NH_3$+$H_2O$ | 60 | ~ 0.7 |

The selectivity for $CO_2$ reduction shifts as the electrolyte is changed from aqueous to organic solvents. This observed phenomenon poses new questions: (1) Whether the difference in solubility or proton availability causes this change in selectivity towards $CO_2$ reduction? (2) Does the higher solubility of $CO_2$ in organic solvents change $CO_2$

structure, thereby influencing catalytic activity? (3) How are the structures of intermediates formed during $CO_2$ reduction different in water and organic solvents? Probing into the nature of interactions between $CO_2$ and organic solvent molecules can potentially provide insights into the shift in selectivity.

**$CO_2$ Structure(s) in Organic Solvents:** Organic solvents tend to form complexes with $CO_2$ primarily through lewis acid-base attractions. The stability of complex formed during interaction of $CO_2$ with oxygen donating species can be determined in cryosolutions (e.g. liquid argon), since these complexes are formed under equilibrium conditions.[82] The interaction of $CO_2$ with dimethyl ether (DME) in a liquid argon environment is studied.[82] The carbon atom of $CO_2$, being a lewis acid interacts with oxygen atom in DME, which behaves as a lewis base. The optimized structure of the complex formed between $CO_2$ and DME obtained from ab initio calculations is shown in **Figure 5.15**.[82] The van der Waals bond length, i.e., the distance between C(10) and O(2) is 2.812 Å, lower than 2.886 Å as predicted by ab initio calculations for $CO_2$-$H_2O$ interactions.[82] Once this complex is formed, the bond angle for $CO_2$ decreases from 180 to 178.1 degrees, thereby causing $CO_2$ molecule to bend slightly.[82] In addition, the C-O bond lengths in the $CO_2$-DME complex also shorten by $0.2 \times 10^{-4}$ Å, in comparison to linear $CO_2$ molecule.[82]

The structure of the complex formed was experimentally investigated using IR spectroscopy. The presence of several new bands suggested the presence of formation of complex between $CO_2$ and DME.[82] The degenerate bending modes for $CO_2$ at ~ 664 $cm^{-1}$ split into two, one blue-shifted by 4.5 $cm^{-1}$, while the other red shifted by 14.1 $cm^{-1}$ for the complex species.[82] The 1:1 stoichiometry of the complex was obtained by changing the concentrations of $CO_2$ in DME and analyzing the intensities of bands at 928, 668 and 650 cm$^{-1}$ arising from the complex structure with the bands from $CO_2$ and DME at 664 and 931 cm$^{-1}$ respectively.[82]

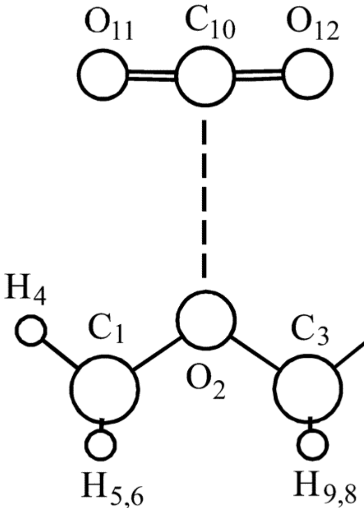

**Figure 5.15.** Optimized structure of complex formed during $CO_2$ and DME interaction[82]

Depending upon the type of organic group in the solvent, weak interactions of oxygen atom of $CO_2$ and hydrogen atom in alkyl group are also demonstrated. In this regard, the optimized complex structure formed between $CO_2$ and acetaldehyde predicted by ab initio calculations is shown in **Figure 5.16.**[83] The binding energy of the complex for the optimized geometry relative to the separated molecules infinitely apart is ~ -2.69 kcal/mol; which includes both the Lewis acid - Lewis base and weaker C-H--O interactions.[83] The aldehydic proton interacts with one of the oxygen atom in $CO_2$ as shown in **Figure 5.16**. This enhanced C-H--O interactions lead to higher solubility of $CO_2$ in acetate-containing compounds. In addition, the carbon atom hybridization determines the effect of C-H--X interaction on C-H bond length as demonstrated by ab initio calculations.[83] For the case of acetaldehyde-$CO_2$ system, the C-H bond involved in C-H--O interaction actually contracts, reflected by a blue-shift in the C-H stretching frequency. [83]

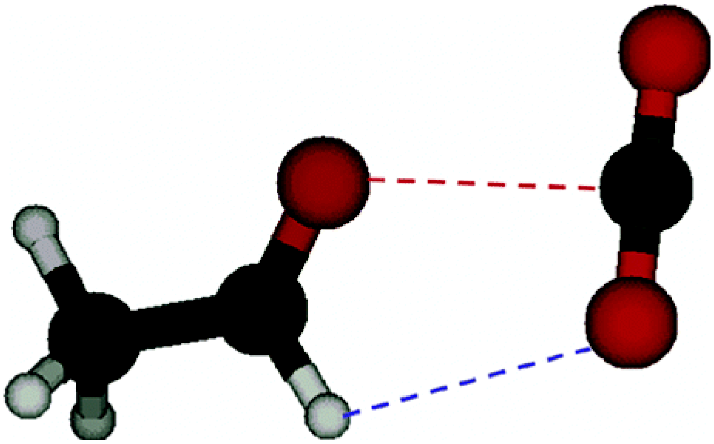

**Figure 5.16.** Optimized structure of the acetaldehyde-$CO_2$ complex[83]

The Raman spectra for acetaldehyde with He and $CO_2$ is shown in **Figure 5.17**.[83] Helium allows to investigate the peak shifts arising only because of specific interactions due to its negligible intermolecular attractions.[83] A red-shift for the carbonyl band maximum is observed from 1746.0 to 1743.5 $cm^{-1}$ (**Figure 5.17A**), a shift of -2.5 $cm^{-1}$ and increases in width from 6.8 to 9.2 $cm^{-1}$, i.e. an increase of 2.4 $cm^{-1}$. Interestingly, **Figure 5.17B** shows that the aldehydic proton band maximum blue shifts from 2717.0 to 2718.3 $cm^{-1}$, a shift of +1.3 $cm^{-1}$ and broadens significantly, increasing in width from 4.5 to 8.9 $cm^{-1}$, an increase of 4.4 $cm^{-1}$. These observations are consistent with the predicted C-H--O interaction involving the oxygen atom in $CO_2$ as shown in **Figure 5.16**. The intensity of the aldehyde C-H stretching mode following $CO_2$ solvation also decreases significantly as illustrated in insets of **Figure 5.17B**. This decrease in the C-H stretching intensity also suggests C-H--O interaction. On the other hand, the intensity for the carbonyl stretching mode decreases only slightly following $CO_2$ solvation (**Figure 5.17A**). These results illustrate that for carbonyl group based organic solvents, $CO_2$ preferentially interacts only with aldehydic proton.

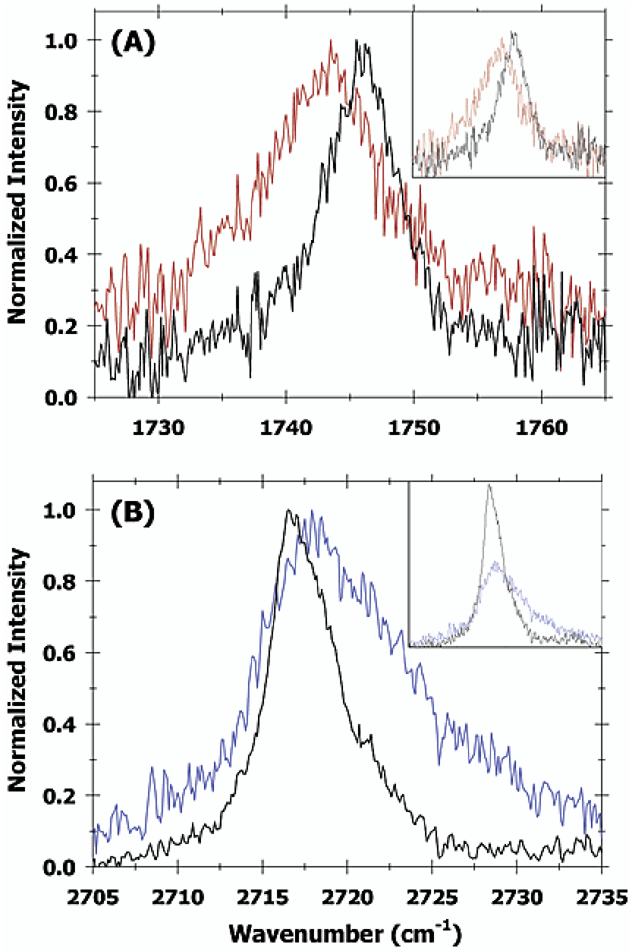

**Figure 5.17.** Raman spectra of acetaldehyde (A) the carbonyl stretch region in He (black) and $CO_2$ (red). (B) the aldehydic C-H stretch in He (black) and $CO_2$ (blue). Insets show the intensity changes upon complexation. [83]

**Electrocatalytic $CO_2$ Activation:** Organic solvents exhibit a much higher cathodic potential window in comparison to aqueous electrolytes because of difficulty of breaking the C−H bonds when compared with O−H bonds in water. Therefore, higher overpotentials can be applied in the case of organic solvents, and $CO_2$ reduction can be obtained because of the suppression of concurrent hydrogen evolution reaction. In addition, efficient $CO_2$ reduction requires protons in electrolyte for forming products other than CO, carbonate, and oxalate from $CO_2$ reduction.[84] Due to low proton availability in organic solvents, the products typically formed from $CO_2$ reduction include CO and oxalate.[85] On the other hand, the presence of water even in residual levels (~ 50 ppm) can influence the reaction mechanism of $CO_2$ reduction in organic electrolytes, leading to the formation of different products.[84, 86, 87]

$$2CO_2 + H_2O + e^- \rightarrow HCO_2^- + HCO_3^- \quad \text{(In aqueous electrolytes)}$$

$$2CO_2 + 2\,e^- \rightarrow C_2O_4^-;\; 2CO_2 + 2\,e^- \rightarrow CO + CO_3^{2-} \quad \text{(In organic solvents)}$$

In the absence of protons, the overpotential for $CO_2$ reduction is high as the reaction can only proceed through the formation of $CO_2^-$ radical anion;[84] which happens at high cathodic potentials (~ -1.9 V vs. NHE). Therefore, organic electrolytes that can stabilize this intermediate would only result in significant product formation from $CO_2$ reduction. Indeed, tuning the selectivity for formation of different products from $CO_2$ reduction in organic electrolytes would require a deeper understanding of the nature of interactions between $CO_2^-$ radical anion and solvent molecules.

## 5.3 $CO_2$ in Ionic Liquids

Ionic-liquid mediated $CO_2$ reduction has been reported on various catalysts systems.[14, 33, 88, 89] The ionic liquid tends to stabilize the intermediate formed during $CO_2$ reduction by forming a complex. This significantly lowers the lowers the overpotential for CO2 activation in comparison to aqueous and organic solvents as electrolyte (**Figure 5.18**).[14] The complex formed in presence of ionic liquid should bind strongly enough to facilitate $CO_2$ reduction, however too much stronger binding might make the complex unreactive.[14] Similar to the cases of water and organic solvent systems, an understanding of the interactions between ionic liquid and $CO_2$ would be beneficial to engineer the overpotential and selectivity of products formed during $CO_2$ reduction.

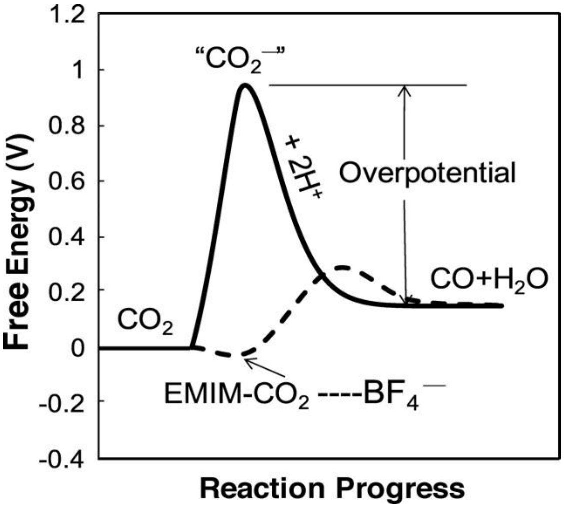

**Figure 5.18.** A schematic of how the free energy of the system changes during the reaction $CO_2 + 2H^+ + 2e^- \rightleftharpoons CO + H_2O$ in water or acetonitrile (solid line) or EMIM-$BF_4$ (dashed line)[14]

**$CO_2$ Solubility in Ionic Liquids:** Solubility of $CO_2$ in room temperature ionic liquids (RTILs) at ambient pressure and temperature is comparable to some of the organic solvents. An ionic liquid is a salt where the ions are poorly coordinated, resulting in their liquid phase at room temperatures. Some examples are, [emim][$BF_4$], [emim][$PF_6$], [emim][$ClO_4$], [emim][$NO_3$] etc. Structure of [emim] cation is represented in **Figure 5.19**; e, m and im in [emim] correspond to ethyl, methyl and imidazolium respectively. The anion plays a key role in $CO_2$ dissolution in RTILs, while increasing the alkyl chain length in cation increases $CO_2$ solubility slightly.[90] Typically, the solubility of $CO_2$ can be increased by increasing the number of fluoroalkyl groups in both the anion and cation group, although the extent of increase is larger with anion-fluorination.[90] Importantly, van der Waal forces dominate the dissolution of $CO_2$ in RTILs[91]; different from $CO_2$ solvation in aqueous solution, where formation of hydrogen bonds might happen as discussed previously.

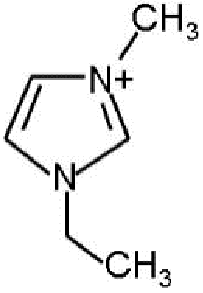

**Figure 5.19.** Structure of [emim] cation in an ionic liquid

However, the hydrogen attached to C2 position (C atom attached to two N atoms) in imidazol is relatively more acidic than other hydrogen atoms and therefore, might provide site for formation of hydrogen bonds with $CO_2$, facilitating dissolution.[90]

Computational studies show that $CO_2$ solubility in ionic liquids is governed by two factors. 1) cation-anion and 2) $CO_2$-anion interaction.[92] **Figure 5.20** relate the $CO_2$ solubility to interaction energy of cation and anion in an ionic liquid and interaction energy between $CO_2$ and respective anion of the ionic liquid.  These results suggest that weaker cation-anion interaction in the ionic liquid is the dominating factor in determining

$CO_2$ solubility.[92] This is because weak cation-anion interaction allows for easier expansion and $CO_2$ insertion.

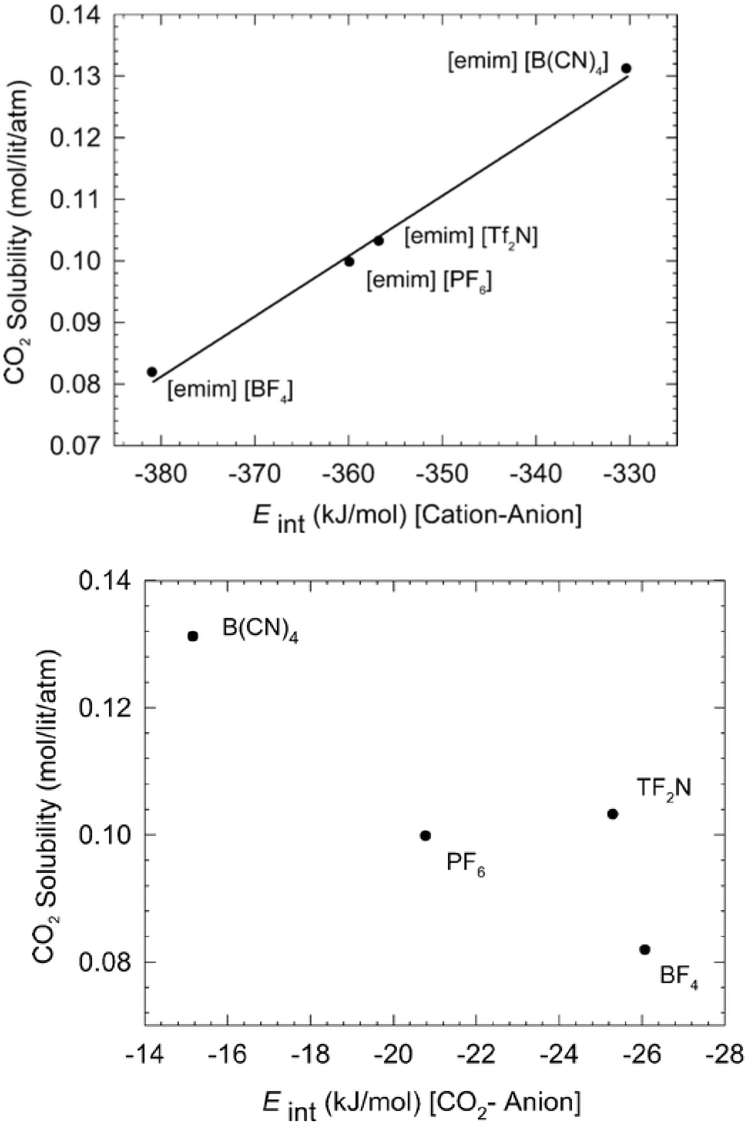

**Figure 5.20.** Correlation between gas-phase cation-anion interaction energy and the experimental $CO_2$ solubility at 1 bar and 298 K for four ionic liquids with the same [emim] cation but different anions (Top). Correlation between the gas-phase $CO_2$ anion interaction energy and the experimental $CO_2$ solubility at 1 bar and 298 K for four ionic liquids with the same [emim] cation but different anions (Bottom)[92]

Surprisingly, the solubility of $CO_2$ in [emim][B(CN)$_4$] is found to be significantly high, irrespective of small and symmetric anion structure. Perhaps the solubility of $CO_2$ in [emim][B(CN)$_4$] is ~ 30% higher than in popular ionic liquid [emim][Tf2N].[92] Radial distribution function studies indicate a weaker cohesion in [emim][B(CN)$_4$] in comparison to [emim][Tf$_2$N] which might result in easier expansion of [emim][B(CN)$_4$].[92] In addition, the strength of hydrogen bonding is reduced significantly in [emim][B(CN)$_4$], thereby explaining its ability to expand during $CO_2$ dissolution.[92] The radial distribution function shows the coordination number of $CO_2$ around [B(CN)$_4$] to be 5.08, while being only 4.0 for [Tf$_2$N], suggesting stronger interaction of $CO_2$ with [B(CN)$_4$] and explaining its higher solubility in [emim][B(CN)$_4$].[92] The behavior of $CO_2$ dissolution in RTILs at low pressures (low pressures ~ 1 bar so that ideal gas behavior can be assumed) can be modeled using modified version of regular solution theory (RST).[93] According to RST, the excess entropy of mixing is zero and hence, forces of attraction existing between molecules are primarily short-range dispersion forces at constant pressure and temperature. The presence of a large cation in RTILs delocalizes the charge resulting in low coulombic interactions, which are short-range. The Henry's constant governing the solubility of $CO_2$ in RTILs is given by **Equation [9]**.[94]

$$ln\, H_{CO2} = A + B(\delta_{IL} - \delta_{CO2})^2 \qquad [9]$$

where A and B are parameters that depend only on temperature; while $\delta_{IL}$ and $\delta_{CO2}$ are solubility parameters for pure RTIL and $CO_2$

The solubility parameter of a given molecule is defined by the square root of its cohesive energy density, which is related to the energy of vaporization, $\Delta U^{vap}$ and molar volume , $\vartheta$, by **Equation [10].**[94]

$$\delta = \sqrt{\frac{\Delta U^{vap}}{\vartheta}} \qquad [10]$$

The accurate determinations of energy of vaporization ($\Delta U^{vap}$) for RTILs are, however, difficult considering their non-volatility. Different approaches have been adopted in literature to compute cohesive energy density of RTILs, some of which are highlighted elsewhere.[94] On the other hand, the solubility parameter for $CO_2$ as a function of temperature is given by **Equation [11]**.[94]

$$\delta_{CO2} = -0.0535T + 28.26 \qquad [11]$$

where T is the absolute temperature. The solubility of $CO_2$ is inversely proportional to the solubility parameter of the ionic liquid.[94]

$CO_2$ exhibits a remarkable solubility, with mole fractions of $CO_2$ reaching up to 30% in imidazolium based ionic liquids.[95] Attenuated total reflectance–infra red (ATR-IR) spectroscopy shows a lewis acid-base interaction between $CO_2$ and anions of the ionic liquids.[96] On the other hand, acidic hydrogen atoms tend to form hydrogen bonds with oxygen atoms in the $CO_2$ molecule. The solubility of $CO_2$ in ionic liquid is, however, primarily governed by the lewis acid-base interaction between $CO_2$ and anion of the ionic liquid; while the acidic hydrogen atoms affect $CO_2$ solubility only slightly.[95]

**$CO_2$ Structure(s) in Ionic Liquid:** The partial molar volumes of ionic liquids before and after $CO_2$ dissolution remain nearly the same, suggesting that $CO_2$ doesn’t disturb the underlying structure of ionic liquid upon dissolution.[95] These results highlight that the cation and anion form a strong network in ionic liquids with $CO_2$ filling the interstices in the fluid.[95] This is further supported by molecular dynamics simulation studies of $CO_2$ in [emim][B(CN)$_4$], which suggest that $CO_2$ is present in the void regions of the B(CN)4 tetrahedron; above and below the five-membered ring of the [emim] cation **(Figure 5.21)**.[97] Raman spectra of $CO_2$ in imidazole based RTILs, i.e., [bmim][PF$_6$] (b representing butyl group), however, show no shift in peak positions **(Figure 5.22)** for the Fermi doublet observed for $CO_2$,[98] a phenomenon different from what observed in aqueous solution, and suggesting no hydrogen bond type interaction.

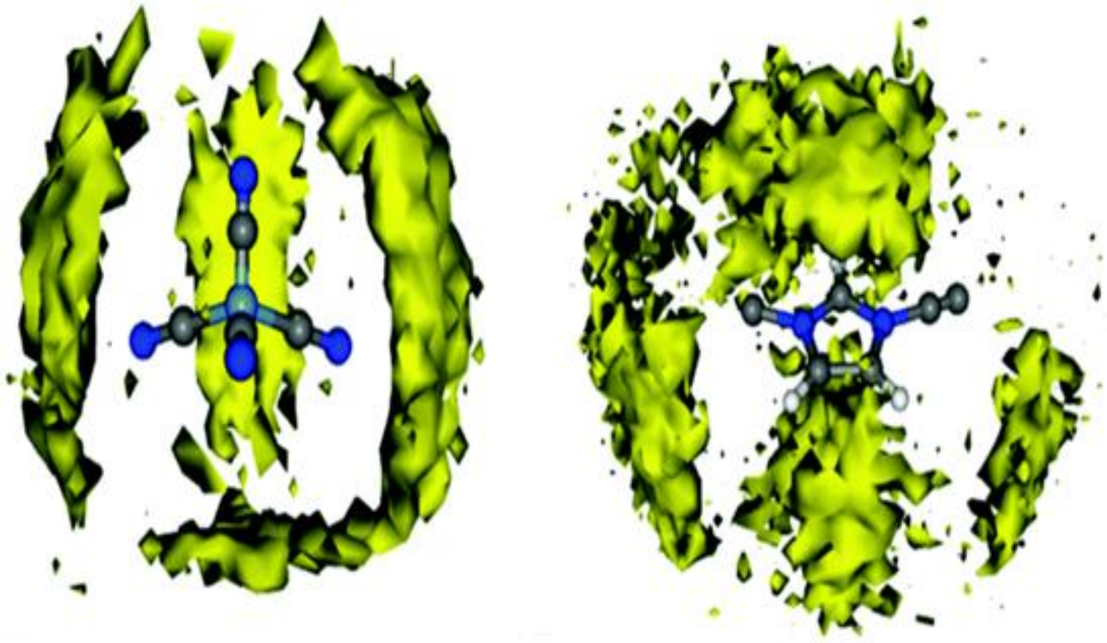

**Figure 5.21.** The spatial radial distribution function of $CO_2$ (yellow) around B(CN)$_4$ (left) and emim (right)[97]

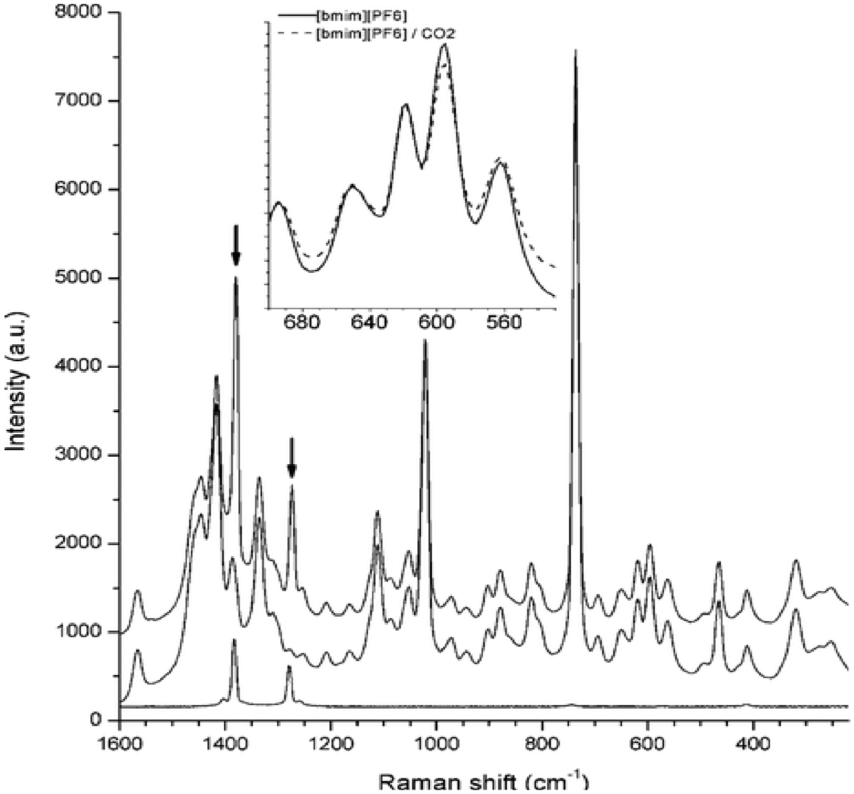

**Figure 5.22.** Raman spectra of [bmim][$PF_6$]-$CO_2$ system at 313 K. From top to bottom 1) [bmim][$PF_6$]-$CO_2$ at 140 bar. 2) [bmim][$PF_6$] without $CO_2$. 3) Pure $CO_2$. Arrows indicate bands of pure $CO_2$[98]

Nonfluorinated $CO_2$-philic molecules in ionic liquids have attracted attention because of the high cost and environmental implications of the fluorinated materials.[99, 100] The $CO_2$-philicity can be increased by choosing carbonyl groups based cations in the ionic liquids. These carbonyl groups can interact with $CO_2$ through the lewis acid-base attractions. The solubility of $CO_2$ in ionic liquid can also be improved by introducing an ether based group in the cation.[101] In addition, introducing cation in ionic liquid having carbonyl groups adjacent to the nitrogen can provide opportunity for interaction with $CO_2$.[101] This carbonyl group is particularly nucleophilic, and can interact with the electrophilic carbon in $CO_2$.[101] The strength of interaction between an ionic liquid and $CO_2$ can provide the estimate of stability of the resulting complex formed between these two species. A larger negative value for the enthalpy indicates stronger interactions between $CO_2$ molecules and ionic liquid. The partial molar enthalpy and entropy of dissolution of $CO_2$ in the ionic liquids can be calculated from the temperature dependence of the Henry's law constants.[102] The partial molar enthalpies of $CO_2$ dissolution, however, exhibited similar values (~ -12 KJ/mol) in different ionic liquids.[102] Therefore, the relative strengths of physical interactions between $CO_2$ and ionic liquids is challenging to determine experimentally. Computational studies have shown that $CO_2$ solvation in fluorinated anion ionic liquid ([bmim][$PF_6$]) is primarily facilitated by anion. $CO_2$ molecules were found to be aligned tangential to the anion spheres with their most probable location being the octahedral voids of the anion.[103] Furthermore, the structure of ionic liquid was found similar after $CO_2$ dissolution predicted using radial distribution function analysis as supported by experimental measurements.[103, 104]

**Electrocatalytic $CO_2$ Activation in Ionic Liquids:** Since 2011, $CO_2$ electrocatalysis in ionic liquid electrolytes has been reported widely.[14, 16, 33, 89, 105] Specifically, 1,3-Dialkyl substituted imidazolium based ionic liquids that can strongly interact with $CO_2$ have attracted attention in this regard.[106] Stabilizing the intermediate, $CO_2^-$ formed during $CO_2$ reduction can perhaps lower the overpotential for this reaction.[107] The intermediate formed during $CO_2$ reduction tend to bind to such an ionic liquid, thereby decreasing the overpotential for CO formation.[14] The carboxylation of the imidazolium in presence of $CO_2$ as depicted for 1,3-dimethylimidazolium by **Equation [12]** can potentially provide protons for $CO_2$ reduction.[106, 108, 109] In addition, ionic liquids, like organic solvents offer a wider electrochemical cathodic potential window for $CO_2$ reduction, where water reduction can be substantially suppressed.

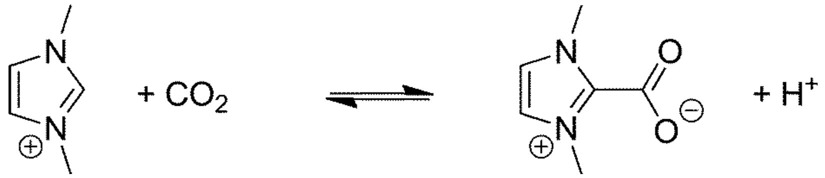

[12]

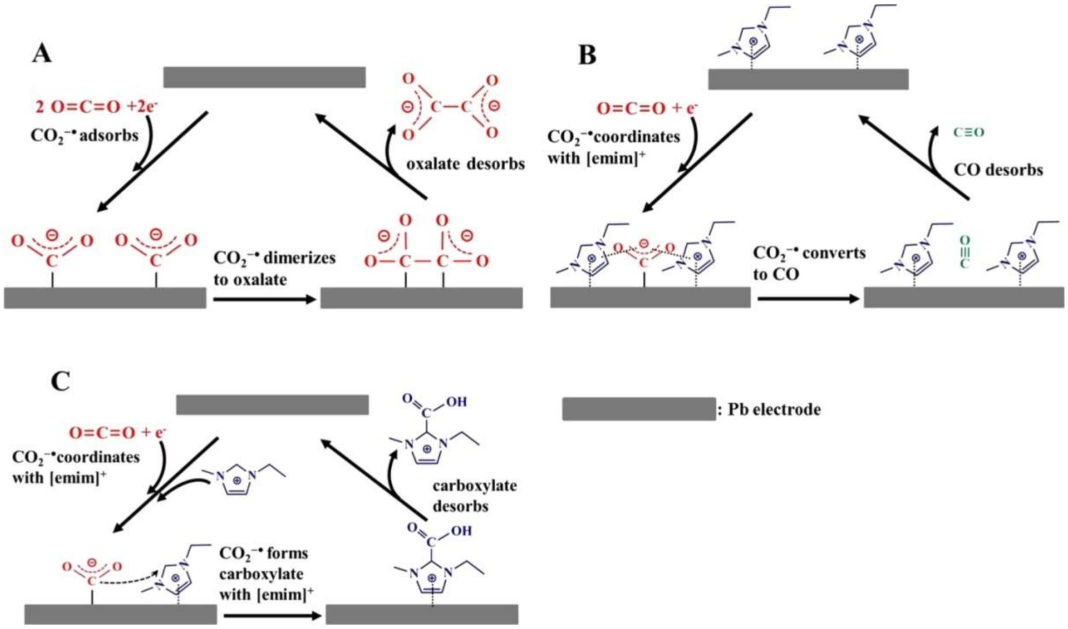

**Figure 5.23.** Reaction Pathways for the Electrochemical Reduction of $CO_2$ in the (A) Absence and (B, C) Presence of [emim][$Tf_2N$] at a Pb Electrode in acetonitrile.[110]

**Figure 5.23** illustrates the difference in mechanism and selectivity of products for $CO_2$ reduction on Pb electrode in an organic solvent (acetonitrile) in the presence of an ionic liquid ([emim][$Tf_2N$]). A further understanding of the interactions between ionic liquids and intermediates formed during $CO_2$ reduction would be necessary in future to engineer the selectivity towards formation of hydrocarbons and alcohols.

## 5.4 Summary

$CO_2$ capture and utilization technologies which enable $CO_2$ recycling from atmosphere can potentially address environmental problems due to global warming. In one approach, $CO_2$ capturing schemes might use suitable solvents that dissolve $CO_2$. Aqueous solvents in spite of possessing low $CO_2$ solubility (~ 35 mM) still provide economical alternatives to the source of protons necessary for subsequent $CO_2$ conversion to fuels during electrocatalysis. Ionic liquids based solvent systems can be particularly useful for $CO_2$ capture schemes. However, the cost-effectiveness of this process can be achieved combining ionic liquids with other solvents, leading to a class of hybrid solvents. Rationalizing the design of such hybrid solvents would require an in-depth understanding of the interaction of $CO_2$ with different solvent molecules. Furthermore, an understanding of interactions between intermediates formed during $CO_2$ electrocatalysis with solvent molecules can be useful in engineering the product selectivity during $CO_2$ conversion to fuels.

## References

1. Meinshausen M, *et al.* Greenhouse-gas emission targets for limiting global warming to 2[thinsp][deg]C. *Nature* **458**, 1158-1162 (2009).

2. Allen MR, *et al.* Warming caused by cumulative carbon emissions towards the trillionth tonne. *Nature* **458**, 1163-1166 (2009).

3. Matthews HD, Gillett NP, Stott PA, Zickfeld K. The proportionality of global warming to cumulative carbon emissions. *Nature* **459**, 829-832 (2009).

4. Dobricic S, Vignati E, Russo S. Large-Scale Atmospheric Warming in Winter and the Arctic Sea Ice Retreat. *Journal of Climate* **29**, 2869-2888 (2016).

5. Stips A, Macias D, Coughlan C, Garcia-Gorriz E, San Liang X. On the causal structure between CO2 and global temperature. *Scientific Reports* **6**, (2016).

6. Wang W, Nemani R. Dynamic responses of atmospheric carbon dioxide concentration to global temperature changes between 1850 and 2010. *Advances in Atmospheric Sciences* **33**, 247-258 (2016).

7. Crowley TJ. Causes of climate change over the past 1000 years. *Science* **289**, 270-277 (2000).

8. Hansen J, Sato M, Ruedy R, Lo K, Lea DW, Medina-Elizade M. Global temperature change. *Proceedings of the National Academy of Sciences of the United States of America* **103**, 14288-14293 (2006).

9. Shakun JD, *et al.* Global warming preceded by increasing carbon dioxide concentrations during the last deglaciation. *Nature* **484**, 49-+ (2012).

10. Schneider SH. The Greenhouse Effect: Science and Policy. *Science* **243**, 771-781 (1989).

11. McGlade C, Ekins P. The geographical distribution of fossil fuels unused when limiting global warming to 2 [deg]C. *Nature* **517**, 187-190 (2015).

12. Hansen J, *et al.* Ice melt, sea level rise and superstorms: evidence from paleoclimate data, climate modeling, and modern observations that 2 °C global warming is highly dangerous. *Atmos Chem Phys Discuss* **15**, 20059-20179 (2015).

13. Schleussner CF, *et al.* Differential climate impacts for policy-relevant limits to global warming: the case of 1.5 °C and 2 °C. *Earth Syst Dynam* **7**, 327-351 (2016).

14. Rosen BA, *et al.* Ionic Liquid–Mediated Selective Conversion of $CO_2$ to CO at Low Overpotentials. *Science* **334**, 643-644 (2011).

15. Kim B, Ma S, Molly Jhong H-R, Kenis PJA. Influence of dilute feed and pH on electrochemical reduction of $CO_2$ to CO on Ag in a continuous flow electrolyzer. *Electrochimica Acta* **166**, 271-276 (2015).

16. Lu Q, *et al.* A selective and efficient electrocatalyst for carbon dioxide reduction. *Nat Commun* **5**, (2014).

17. Chen Y, Li CW, Kanan MW. Aqueous $CO_2$ Reduction at Very Low Overpotential on Oxide-Derived Au Nanoparticles. *Journal of the American Chemical Society* **134**, 19969-19972 (2012).

18. Zhu W, *et al.* Monodisperse Au Nanoparticles for Selective Electrocatalytic Reduction of $CO_2$ to CO. *Journal of the American Chemical Society* **135**, 16833-16836 (2013).

19. Nursanto EB, *et al.* Gold catalyst reactivity for $CO_2$ electro-reduction: From nano particle to layer. *Catalysis Today*.

20. Hori Y, Takahashi I, Koga O, Hoshi N. Selective Formation of C2 Compounds from Electrochemical Reduction of $CO_2$ at a Series of Copper Single Crystal Electrodes. *The Journal of Physical Chemistry B* **106**, 15-17 (2001).

21. Hori Y, Murata A, Takahashi R. Formation of hydrocarbons in the electrochemical reduction of carbon dioxide at a copper electrode in aqueous solution. *Journal of the Chemical Society, Faraday Transactions 1: Physical Chemistry in Condensed Phases* **85**, 2309-2326 (1989).

22. Li CW, Kanan MW. $CO_2$ Reduction at Low Overpotential on Cu Electrodes Resulting from the Reduction of Thick $Cu_2O$ Films. *Journal of the American Chemical Society* **134**, 7231-7234 (2012).

23. Li CW, Ciston J, Kanan MW. Electroreduction of carbon monoxide to liquid fuel on oxide-derived nanocrystalline copper. *Nature* **508**, 504-507 (2014).

24. Verdaguer-Casadevall A, *et al.* Probing the Active Surface Sites for CO Reduction on Oxide-Derived Copper Electrocatalysts. *Journal of the American Chemical Society* **137**, 9808-9811 (2015).

25. Wu J, Sharma PP, Harris BH, Zhou X-D. Electrochemical reduction of carbon dioxide: IV dependence of the Faradaic efficiency and current density on the microstructure and thickness of tin electrode. *Journal of Power Sources* **258**, 189-194 (2014).

26. Wu J, Risalvato FG, Ma S, Zhou X-D. Electrochemical reduction of carbon dioxide III. The role of oxide layer thickness on the performance of Sn electrode in a full electrochemical cell. *Journal of Materials Chemistry A* **2**, 1647-1651 (2014).

27. Wu J, Risalvato FG, Ke F-S, Pellechia PJ, Zhou X-D. Electrochemical Reduction of Carbon Dioxide I. Effects of the Electrolyte on the Selectivity and Activity with Sn Electrode. *Journal of The Electrochemical Society* **159**, F353-F359 (2012).

28. Chen Y, Kanan MW. Tin Oxide Dependence of the $CO_2$ Reduction Efficiency on Tin Electrodes and Enhanced Activity for Tin/Tin Oxide Thin-Film Catalysts. *Journal of the American Chemical Society* **134**, 1986-1989 (2012).

29. Zhang S, Kang P, Meyer TJ. Nanostructured Tin Catalysts for Selective Electrochemical Reduction of Carbon Dioxide to Formate. *Journal of the American Chemical Society* **136**, 1734-1737 (2014).

30. Bandi A. Electrochemical Reduction of Carbon Dioxide on Conductive Metallic Oxides. *Journal of The Electrochemical Society* **137**, 2157-2160 (1990).

31. Qu J, Zhang X, Wang Y, Xie C. Electrochemical reduction of $CO_2$ on $RuO_2/TiO_2$ nanotubes composite modified Pt electrode. *Electrochimica Acta* **50**, 3576-3580 (2005).

32. Ramesha GK, Brennecke JF, Kamat PV. Origin of Catalytic Effect in the Reduction of $CO_2$ at Nanostructured $TiO_2$ Films. *ACS Catalysis* **4**, 3249-3254 (2014).

33. Kumar B, *et al.* Renewable and metal-free carbon nanofibre catalysts for carbon dioxide reduction. *Nat Commun* **4**, (2013).

34. Zhang S, *et al.* Polyethylenimine-Enhanced Electrocatalytic Reduction of $CO_2$ to Formate at Nitrogen-Doped Carbon Nanomaterials. *Journal of the American Chemical Society* **136**, 7845-7848 (2014).

35. Wu J, *et al.* Achieving Highly Efficient, Selective, and Stable $CO_2$ Reduction on Nitrogen-Doped Carbon Nanotubes. *ACS Nano* **9**, 5364-5371 (2015).

36. Sharma PP, *et al.* Nitrogen-Doped Carbon Nanotube Arrays for High-Efficiency Electrochemical Reduction of $CO_2$: On the Understanding of Defects, Defect Density, and Selectivity. *Angewandte Chemie International Edition*, n/a-n/a (2015).

37. Zanta CLPS, de Andrade AR, Boodts JFC. Solvent and support electrolyte effects on the catalytic activity of Ti/$RuO_2$ and Ti/$IrO_2$ electrodes: oxidation of isosafrole as a probe model. *Electrochimica Acta* **44**, 3333-3340 (1999).

38. Sasaki K, Kashimura T, Ohura M, Ohsaki Y, Ohta N. Solvent Effect in the Electrochemical Reduction of p-Quinones in Several Aprotic Solvents. *Journal of The Electrochemical Society* **137**, 2437-2443 (1990).

39. Falciola L, Gennaro A, Isse AA, Mussini PR, Rossi M. The solvent effect in the electrocatalytic reduction of organic bromides on silver. *Journal of Electroanalytical Chemistry* **593**, 47-56 (2006).

40. Iwuoha EI, Smyth MR, Lyons MEG. Solvent effects on the reactivities of an amperometric glucose sensor. *Journal of Electroanalytical Chemistry* **390**, 35-45 (1995).

41. Sha Y, Yu TH, Liu Y, Merinov BV, Goddard WA. Theoretical Study of Solvent Effects on the Platinum-Catalyzed Oxygen Reduction Reaction. *The Journal of Physical Chemistry Letters* **1**, 856-861 (2010).

42. Chaplin RPS, Wragg AA. Effects of process conditions and electrode material on reaction pathways for carbon dioxide electroreduction with particular reference to formate formation. *Journal of Applied Electrochemistry* **33**, 1107-1123 (2003).

43. Delacourt C, Ridgway PL, Kerr JB, Newman J. Design of an Electrochemical Cell Making Syngas $(CO + H_2)$ from $CO_2$ and $H_2O$ Reduction at Room Temperature. *Journal of The Electrochemical Society* **155**, B42-B49 (2008).

44. Wu J, Risalvato FG, Sharma PP, Pellechia PJ, Ke F-S, Zhou X-D. Electrochemical Reduction of Carbon Dioxide: II. Design, Assembly, and Performance of Low Temperature Full Electrochemical Cells. *Journal of The Electrochemical Society* **160**, F953-F957 (2013).

45. Jitaru M, Lowy DA, Toma M, Toma BC, Oniciu L. Electrochemical reduction of carbon dioxide on flat metallic cathodes. *J Appl Electrochem* **27**, 875-889.

46. Ohta K, Kawamoto M, Mizuno T, Lowy AD. Electrochemical reduction of carbon dioxide in methanol at ambient temperature and pressure. *J Appl Electrochem* **28**, 717-724.

47. Hori Y, Vayenas CG, White RE, Gamboa-Aldeco ME. *Modern Aspects of Electrochemistry* (2008).

48. Ikeda S, Takagi T, Ito K. Selective Formation of Formic Acid, Oxalic Acid, and Carbon Monoxide by Electrochemical Reduction of Carbon Dioxide. *Bulletin of the Chemical Society of Japan* **60**, 2517-2522 (1987).

49. Kaneco S, Iiba K, Ohta K, Mizuno T. Electrochemical reduction of carbon dioxide on copper in methanol with various potassium supporting electrolytes at low temperature. *J Solid State Electrochem* **3**, 424-428.

50. Podlovchenko BI, Kolyadko EA, Lu S. Electroreduction of carbon dioxide on palladium electrodes at potentials higher than the reversible hydrogen potential. *Journal of Electroanalytical Chemistry* **373**, 185-187 (1994).

51. Azuma M, Hashimoto K, Hiramoto M, Watanabe M, Sakata T. Electrochemical Reduction of Carbon Dioxide on Various Metal Electrodes in Low-Temperature Aqueous $KHCO_3$ Media. *Journal of The Electrochemical Society* **137**, 1772-1778 (1990).

52. Schrebler R, Cury P, Herrera F, Gómez H, Córdova R. Study of the electrochemical reduction of $CO_2$ on electrodeposited rhenium electrodes in methanol media. *Journal of Electroanalytical Chemistry* **516**, 23-30 (2001).

53. Ohmori T, Nakayama A, Mametsuka H, Suzuki E. Influence of sputtering parameters on electrochemical $CO_2$ reduction in sputtered Au electrode. *Journal of Electroanalytical Chemistry* **514**, 51-55 (2001).

54. Falk M, Miller AG. Infrared spectrum of carbon dioxide in aqueous solution. *Vibrational Spectroscopy* **4**, 105-108 (1992).

55. Richard E. Zeebe DW-G. $CO_2$ in Seawater: Equilibrium, Kinetics, Isotopes. (ed^(eds). Elsevier (2001).

56. Rudolph WW, Fischer D, Irmer G. Vibrational Spectroscopic Studies and Density Functional Theory Calculations of Speciation in the $CO_2$?Water System. *Applied Spectroscopy* **60**, 130-144 (2006).

57. Thauer RK, Jungermann K, Decker K. Energy conservation in chemotrophic anaerobic bacteria. *Bacteriological Reviews* **41**, 100-180 (1977).

58. Stefánsson A, Bénézeth P, Schott J. Carbonic acid ionization and the stability of sodium bicarbonate and carbonate ion pairs to 200&#xa0;°C – A potentiometric and spectrophotometric study. *Geochimica et Cosmochimica Acta* **120**, 600-611 (2013).

59. Duan Z, Sun R. An improved model calculating $CO_2$ solubility in pure water and aqueous NaCl solutions from 273 to 533 K and from 0 to 2000 bar. *Chemical Geology* **193**, 257-271 (2003).

60. Frank MJW, Kuipers JAM, van Swaaij WPM. Diffusion Coefficients and Viscosities of $CO_2$ + $H_2O$, $CO_2$ + $CH_3OH$, $NH_3$ + $H_2O$, and $NH_3$ + $CH_3OH$ Liquid Mixtures. *Journal of Chemical & Engineering Data* **41**, 297-302 (1996).

61. Cadogan SP, Maitland GC, Trusler JPM. Diffusion Coefficients of $CO_2$ and $N_2$ in Water at Temperatures between 298.15 K and 423.15 K at Pressures up to 45 MPa. *Journal of Chemical & Engineering Data* **59**, 519-525 (2014).

62. Sato H, Matubayasi N, Nakahara M, Hirata F. Which carbon oxide is more soluble? Ab initio study on carbon monoxide and dioxide in aqueous solution. *Chemical Physics Letters* **323**, 257-262 (2000).

63. England AH, Duffin AM, Schwartz CP, Uejio JS, Prendergast D, Saykally RJ. On the hydration and hydrolysis of carbon dioxide. *Chemical Physics Letters* **514**, 187-195 (2011).

64. Leung K, Nielsen IMB, Kurtz I. Ab Initio Molecular Dynamics Study of Carbon Dioxide and Bicarbonate Hydration and the Nucleophilic Attack of Hydroxide on $CO_2$. *The Journal of Physical Chemistry B* **111**, 4453-4459 (2007).

65. Tewes F, Boury F. Thermodynamic and Dynamic Interfacial Properties of Binary Carbon Dioxide−Water Systems. *The Journal of Physical Chemistry B* **108**, 2405-2412 (2004).

66. Sadlej J, Makarewicz J, Chałasiński G. Ab initio study of energy, structure and dynamics of the water–carbon dioxide complex. *The Journal of Chemical Physics* **109**, 3919-3927 (1998).

67. Peterson KI, Klemperer W. Structure and internal rotation of $H_2O$–$CO_2$, HDO–$CO_2$, and $D_2O$–$CO_2$ van der Waals complexes. *The Journal of Chemical Physics* **80**, 2439-2445 (1984).

68. Danten Y, Tassaing T, Besnard M. Ab Initio Investigation of Vibrational Spectra of Water−($CO_2$)n Complexes (n = 1, 2). *The Journal of Physical Chemistry A* **109**, 3250-3256 (2005).

69. Ramachandran CN, Ruckenstein E. Water clustering in the presence of a $CO_2$ molecule. *Computational and Theoretical Chemistry* **966**, 84-90 (2011).

70. Prakash M, Subramanian V, Gadre SR. Stepwise Hydration of Protonated Carbonic Acid: A Theoretical Study. *The Journal of Physical Chemistry A* **113**, 12260-12275 (2009).

71. Chandrasekaran K, Bockris LOM. In-situ spectroscopic investigation of adsorbed intermediate radicals in electrochemical reactions: $CO_2^-$ on platinum. *Surface Science* **185**, 495-514 (1987).

72. Bockris JOM, Wass JC. The Photoelectrocatalytic Reduction of Carbon Dioxide. *Journal of The Electrochemical Society* **136**, 2521-2528 (1989).

73. Villamena FA, Locigno EJ, Rockenbauer A, Hadad CM, Zweier JL. Theoretical and Experimental Studies of the Spin Trapping of Inorganic Radicals by 5,5-Dimethyl-1-Pyrroline N-Oxide (DMPO). 1. Carbon Dioxide Radical Anion. *The Journal of Physical Chemistry A* **110**, 13253-13258 (2006).

74. Tsukuda T, Johnson MA, Nagata T. Photoelectron spectroscopy of $(CO_2)_n^-$ revisited: core switching in the $2 \leqslant n \leqslant 16$ range. *Chemical Physics Letters* **268**, 429-433 (1997).

75. Shin JW, Hammer NI, Johnson MA, Schneider H, Glöβ A, Weber JM. An Infrared Investigation of the $(CO_2)^{n-}$ Clusters: Core Ion Switching from Both the Ion and Solvent Perspectives. *The Journal of Physical Chemistry A* **109**, 3146-3152 (2005).

76. DeLuca MJ, Niu B, Johnson MA. Photoelectron spectroscopy of $(CO_2)^-_n$ clusters with $2 \leq n \leq 13$: Cluster size dependence of the core molecular ion. *The Journal of Chemical Physics* **88**, 5857-5863 (1988).

77. Nagata T, Yoshida H, Kondow T. Photoelectron spectroscopy of $(CO_2)_nH_2O^-$ $(2 \leqslant n \leqslant 8)$ clusters. *Chemical Physics Letters* **199**, 205-210 (1992).

78. Muraoka A, Inokuchi Y, Nishi N, Nagata T. Structures of $[(CO_2)_n(H_2O)_m]^-$ (n=1–4, m=1,2) cluster anions. I. Infrared photodissociation spectroscopy. *The Journal of Chemical Physics* **122**, 094303 (2005).

79. Verma S, Lu X, Ma S, Masel RI, Kenis PJA. The effect of electrolyte composition on the electroreduction of CO2 to CO on Ag based gas diffusion electrodes. *Physical Chemistry Chemical Physics* **18**, 7075-7084 (2016).

80. Salazar-Villalpando MD. Effect of Electrolyte on the Electrochemical Reduction of $CO_2$. *ECS Transactions* **33**, 77-88 (2011).

81. Pazuki GR, Pahlavanzadeh H. Correlation and Prediction of the Solubility of $CO_2$ in a Mixture of Organic Solution Solvents. *Theoretical Foundations of Chemical Engineering* **39**, 240-245.

82. Van Ginderen P, Herrebout WA, van der Veken BJ. van der Waals Complex of Dimethyl Ether with Carbon Dioxide. *The Journal of Physical Chemistry A* **107**, 5391-5396 (2003).

83. Blatchford MA, Raveendran P, Wallen SL. Raman Spectroscopic Evidence for Cooperative C−H···O Interactions in the Acetaldehyde−$CO_2$ Complex. *Journal of the American Chemical Society* **124**, 14818-14819 (2002).

84. Figueiredo MC, Ledezma-Yanez I, Koper MTM. In Situ Spectroscopic Study of $CO_2$ Electroreduction at Copper Electrodes in Acetonitrile. *ACS Catalysis* **6**, 2382-2392 (2016).

85. Amatore C, Saveant JM. Mechanism and kinetic characteristics of the electrochemical reduction of carbon dioxide in media of low proton availability. *Journal of the American Chemical Society* **103**, 5021-5023 (1981).

86. Rudnev AV*, et al.* The promoting effect of water on the electroreduction of $CO_2$ in acetonitrile. *Electrochimica Acta* **189**, 38-44 (2016).

87. Ortiz R, Márquez OP, Márquez J, Gutiérrez C. FTIR spectroscopy study of the electrochemical reduction of $CO_2$ on various metal electrodes in methanol. *Journal of Electroanalytical Chemistry* **390**, 99-107 (1995).

88. Grills DC, Matsubara Y, Kuwahara Y, Golisz SR, Kurtz DA, Mello BA. Electrocatalytic $CO_2$ Reduction with a Homogeneous Catalyst in Ionic Liquid: High Catalytic Activity at Low Overpotential. *The Journal of Physical Chemistry Letters* **5**, 2033-2038 (2014).

89. Oh Y, Hu X. Ionic liquids enhance the electrochemical $CO_2$ reduction catalyzed by $MoO_2$. *Chemical Communications* **51**, 13698-13701 (2015).

90. Aki SNVK, Mellein BR, Saurer EM, Brennecke JF. High-Pressure Phase Behavior of Carbon Dioxide with Imidazolium-Based Ionic Liquids. *The Journal of Physical Chemistry B* **108**, 20355-20365 (2004).

91. Palomar J, Gonzalez-Miquel M, Polo A, Rodriguez F. Understanding the Physical Absorption of $CO_2$ in Ionic Liquids Using the COSMO-RS Method. *Industrial & Engineering Chemistry Research* **50**, 3452-3463 (2011).

92. Babarao R, Dai S, Jiang D-e. Understanding the High Solubility of $CO_2$ in an Ionic Liquid with the Tetracyanoborate Anion. *The Journal of Physical Chemistry B* **115**, 9789-9794 (2011).

93. Bara JE*, et al.* Guide to $CO_2$ Separations in Imidazolium-Based Room-Temperature Ionic Liquids. *Industrial & Engineering Chemistry Research* **48**, 2739-2751 (2009).

94. Moganty SS, Baltus RE. Regular Solution Theory for Low Pressure Carbon Dioxide Solubility in Room Temperature Ionic Liquids: Ionic Liquid Solubility

Parameter from Activation Energy of Viscosity. *Industrial & Engineering Chemistry Research* **49**, 5846-5853 (2010).

95. Cadena C, Anthony JL, Shah JK, Morrow TI, Brennecke JF, Maginn EJ. Why Is $CO_2$ So Soluble in Imidazolium-Based Ionic Liquids? *Journal of the American Chemical Society* **126**, 5300-5308 (2004).

96. Kazarian SG, Briscoe BJ, Welton T. Combining ionic liquids and supercritical fluids: ATR-IR study of CO dissolved in two ionic liquids at high pressures. *Chemical Communications*, 2047-2048 (2000).

97. Liu H, Dai S, Jiang D-e. Structure and dynamics of $CO_2$ and $N_2$ in a tetracyanoborate based ionic liquid. *Physical Chemistry Chemical Physics* **16**, 1909-1913 (2014).

98. Andanson J-M, Jutz F, Baiker A. Supercritical $CO_2$/Ionic Liquid Systems: What Can We Extract from Infrared and Raman Spectra? *The Journal of Physical Chemistry B* **113**, 10249-10254 (2009).

99. Beckman EJ. A challenge for green chemistry: designing molecules that readily dissolve in carbon dioxide. *Chemical Communications*, 1885-1888 (2004).

100. Sarbu T, Styranec TJ, Beckman EJ. Design and Synthesis of Low Cost, Sustainable $CO_2$-philes. *Industrial & Engineering Chemistry Research* **39**, 4678-4683 (2000).

101. Muldoon MJ, Aki SNVK, Anderson JL, Dixon JK, Brennecke JF. Improving Carbon Dioxide Solubility in Ionic Liquids. *The Journal of Physical Chemistry B* **111**, 9001-9009 (2007).

102. Anthony JL, Anderson JL, Maginn EJ, Brennecke JF. Anion Effects on Gas Solubility in Ionic Liquids. *The Journal of Physical Chemistry B* **109**, 6366-6374 (2005).

103. Bhargava BL, Balasubramanian S. Insights into the Structure and Dynamics of a Room-Temperature Ionic Liquid: Ab Initio Molecular Dynamics Simulation Studies of 1-n-Butyl-3-methylimidazolium Hexafluorophosphate ([bmim][$PF_6$]) and the [bmim][$PF_6$]−$CO_2$ Mixture. *The Journal of Physical Chemistry B* **111**, 4477-4487 (2007).

104. Kikui K, *et al.* Solvent structure of ionic liquid with carbon dioxide. *Journal of Molecular Liquids*.

105. Asadi M, *et al.* Robust carbon dioxide reduction on molybdenum disulphide edges. *Nat Commun* **5**, (2014).

106. DiMeglio JL, Rosenthal J. Selective Conversion of $CO_2$ to CO with High Efficiency Using an Inexpensive Bismuth-Based Electrocatalyst. *Journal of the American Chemical Society* **135**, 8798-8801 (2013).

107. Whipple DT, Kenis PJA. Prospects of $CO_2$ Utilization via Direct Heterogeneous Electrochemical Reduction. *The Journal of Physical Chemistry Letters* **1**, 3451-3458 (2010).

108. Matsubara Y, Grills DC, Kuwahara Y. Thermodynamic Aspects of Electrocatalytic $CO_2$ Reduction in Acetonitrile and with an Ionic Liquid as Solvent or Electrolyte. *ACS Catalysis* **5**, 6440-6452 (2015).

109. Medina-Ramos J, DiMeglio JL, Rosenthal J. Efficient Reduction of $CO_2$ to CO with High Current Density Using in Situ or ex Situ Prepared Bi-Based Materials. *Journal of the American Chemical Society* **136**, 8361-8367 (2014).

110. Sun L, Ramesha GK, Kamat PV, Brennecke JF. Switching the Reaction Course of Electrochemical $CO_2$ Reduction with Ionic Liquids. *Langmuir* **30**, 6302-6308 (2014).

# Chapter 6

# Summary and Future Directions

## 6.1 Summary

The overall objective of this dissertation is to explore N-doped carbon nanostructures as potential electrocatalysts for $CO_2$ conversion to fuels. The performance of these electrocatalysts is further benchmarked with some of the metallic catalysts reported in literature, particularly Ag and Au that exhibit high catalytic activity towards $CO_2$ reduction. Based on the results demonstrated in previous chapters, following conclusions can be drawn from this work:

1) N-doped carbon nanotubes (NCNTs) act as a highly active, selective, and stable catalyst for electrocatalytic reduction of $CO_2$ to CO. These economical NCNTs are successful alternatives to expensive noble metal electrocatalysts (Au and Ag) for commercial $CO_2$ reduction application, with the promise of more efficiency and higher selectivity.

2) Compared to noble metals Au and Ag, these NCNTs exhibit lower overpotential to achieve the similar selectivity toward the production of CO. The maximum FE of CO reaches around 80% at a low overpotential of -0.26 V. In contrast, pristine CNTs show poor activity and selectivity toward electro-reduction of $CO_2$.

3) The catalytic activity of these NCNTs depends upon the nature of N-defects and defect density. Moreover, the catalytic activity of the synthesized NCNTs is independent of the electrochemical active surface area. In this regard, pristine CNTs exhibit the poorest catalytic activity in comparison to NCNTs in spite of showing a higher available electrochemical surface area.

4) The superior activity for NCNTs is mainly attributed to a low free energy barrier for the potential-limiting step to form adsorbed COOH. The overpotential required for COOH* formation is the lowest (~ 0.20 V) at a pyridinic N-defect site, followed by pyrrolic-N (~ 0.45 V) and graphitic-N (~ 1.0 V). On the other hand, this overpotential for COOH* intermediate formation on pristine CNTs is ~ 1.9 V.

5) Moreover, the suitable binding energy of the key intermediates enables strong COOH adsorption and feasible CO desorption that contributes to the high selectivity toward CO formation on NCNT electrocatalysts.

6) The presence of graphitic and pyridinic N defects inside CNTs significantly decreases the absolute overpotential and increases the selectivity towards CO formation in comparison to pristine CNTs.

7) The NCNTs synthesized using acetonitrile as the precursor at 850 °C exhibit the highest catalytic activity, that is, the lowest overpotential (~ 0.18 V) and maximum selectivity (~ 80% Faradaic efficiency) for CO formation, owing to the highest graphitic-N (~ 3.5 at.%) and pyridinic-N (~ 1.1 at.%) content.

8) Pyrrolic N defects seem to have little or no impact on $CO_2$ reduction activity, which is congruent with DFT calculations.

9) The N-defects in graphene also catalyze $CO_2$ reduction to CO at low overpotentials with high selectivity and long durability in contrast to pristine graphene, which displays no activity.

10) The pyridinic-N defects exhibit the highest catalytic activity by lowering the free energy barrier to form adsorbed COOH*, eventually leading to CO formation on N-doped graphene. These results demonstrate the directions for future efforts to deliberately incorporate high pyridinic-N content in carbon nanostructures as metal-free electrocatalysts for $CO_2$ reduction.

## 6.2 Future Directions

The development of $CO_2$ conversion technology to fuels still needs significant work in improving selectivity towards hydrocarbons and/or alcohols formation. Currently, copper is the only catalyst material known to form various hydrocarbons and alcohols at reasonable rates from $CO_2$ reduction. Therefore, an integration of copper and carbon nanostructures forming a composite metal-carbon nanomaterial might be a way to accomplish this purpose. Developing this type of composite nanomaterial can allow for stronger CO binding over a CNT/Cu surface and thereby, enabling its subsequent reduction. Engineering carbon nanomaterials with other dopant atoms such as fluorine, boron etc. might be another way to possibly influence the $CO_2$ reduction selectivity towards hydrocarbons or alcohols, which needs to be investigated.

Discovering/engineering other materials that can potentially catalyze $CO_2$ reduction reaction with long-term stability is also an area of active research. In this regard, transition metal dichalcogenides, $MX_2$ with M a transition metal atom (Mo, W etc.) and X a chalcogen atom (S, Se, Te) might provide active sites for $CO_2$ catalysis. There are reports available in literature demonstrating excellent catalytic activity of these 2-D layered materials for different applications. Perhaps, $MoS_2$ exhibits a superior catalytic performance for $CO_2$ reduction than noble metals such as Ag and Au in an ionic liquid environment. Future work needs to be done in engineering this material for efficient $CO_2$ reduction in an aqueous environment. Furthermore, surface structure of these materials need to be investigated in order to understand the active sites for $CO_2$ reduction. In another route, metal nanoparticles can be deposited on metal oxides, which can influence $CO_2$ catalysis synergistically through strong metal-support interactions.

In addition, the interaction of intermediates formed during $CO_2$ reduction with solvent molecules largely remains unknown. An understanding of these interactions would allow us to engineer the selectivity for the formation of a specific product from $CO_2$ reduction. This is particularly important for making higher order hydrocarbons and/or alcohols from $CO_2$ reduction. This study can be done by employing in-situ Raman or FTIR spectroscopy to understand the structure of various intermediates formed in different electrolyte systems during $CO_2$ conversion to hydrocarbons/alcohols. Furthermore, eventually, $CO_2$ reduction at cathode needs to be coupled with water splitting on the anode side to accomplish artificial photosynthesis. In this type of operation, water would be oxidized to oxygen and protons would be transported from the anode to the cathode side leading to $CO_2$ reduction. Realization of this type of technology would largely depend on the development of efficient and cheap electrocatalysts for water oxidation reaction at anode.

# Appendix A: Selective Formation of $C_2$ Products from the Electrochemical Conversion of $CO_2$ on Cu Electrodes Comprised of Nanoporous Ribbon Arrays

## A.1 Introduction

Electrochemical and photoelectrochemical conversion of $CO_2$ to fuels in itself is not a new concept. Much work was done decades ago on the use of metallic electrocatalysts for the formation of $C_1$ based products such as CO and $CH_3OH$.[1-3] Considerable progress has been made since 2010 to address the surface and interface of the electrocatalysts to improve the activity, selectivity and durability of the electrodes.[4-8] Albeit $C_1$ products are ubiquitous, a higher selectivity towards $C_2$ hydrocarbons or alcohols is more economically and industrially desirable. Copper may be the only electrocatalyst capable of forming various hydrocarbons and alcohols through an electrochemical process.[9-10] Central to develop copper-based electrocatalysts is to tackle their lackluster selectivity, due to multi-pathway reactions resulting in the formation of a broad range of $C_1$-$C_3$ products.

Hori’s seminal work showed that the electrolytes with larger cations in the order $Cs^+ > K^+ > Na^+ > Li^+$ promoted the selectivity towards the formation of $C_2H_4$ from 5% to 31%, while decreasing selectivity for $CH_4$ from 32% to 16%, largely due to the increase of pH near the Cu electrode surface.[7,11] The presence of sulfide ions during an electrolysis at 30-atm was observed to lead to an enhanced $C_2$ product selectivity ($C_2H_4$ and $C_2H_5OH$) from 13% to 30% because the adsorption of sulfide ions decreased the surface concentration of CO, thus suppressed the formation of $C_1$ products (e.g. $CH_4$ and $CH_3OH$).[12] Additionally, the surface atom arrangement on the copper electrode, e.g. an addition of (111) or (110) step atoms on the (100) basal plane of a single crystal Cu,[13] was found to increase the selectivity towards the formation of $C_2H_4$ over $CH_4$. In a similar regard, oxide-derived Cu electrodes have shown improved selectivity towards $C_2H_4$ and $C_2H_6$.[5] The $C_2$ selectivity was observed to increase on a Cu nanoflower electrode, which showed that the surface morphology might play a role in the increase of selectivity towards the formation of $C_2H_4$ over $CH_4$.[14] However, various $C_1$ products, including $CH_4$ and $HCOO^-$ were observed, ~30% of $C_1$ products at -1.2 V when the nanoflower copper electrodes were used.[14]

In this work, $CO_2$ reduction was investigated on electrodes comprised of three-dimensional (3-D) porous Cu nanoribbon arrays (NRAs). The selectivity towards the formation of $C_2$ products was improved significantly with a negligible amount of $C_1$ formed (<3%) in a wide potential range. C-C coupling was promoted at potentials < -0.78 V vs. RHE (all potentials are referenced to RHE) to form $C_2H_4$, $C_2H_6$ and $C_2H_5OH$. The total Faradaic efficiency for $C_2$ was over 40%. More importantly, our analysis showed the activation of $CO_2$ occurred at the copper surface; while the presence of copper oxide layer was likely due to the interaction between Cu and water during the post analysis.

## A.2 Experimental

### Materials preparation and characterization

Nanoporous Cu electrode was fabricated by the electrochemical reduction of CuO NRAs as shown in the **Schematic A1.1a**.[15-16] For a typical synthesis process, NaOH (125 mmol), NaCl (34.2 mmol), $Na_2S_2O_8$ (3.5 mmol), and $CuSO_4$ (0.04 mmol) were dissolved into 100 mL deionized water (Siemens, Labstar). Cu foil (99.99% purity) with a geometric surface area of 4 $cm^2$ was immersed in the as-prepared solution at $86^oC$ for 8 min, during which Cu was oxidized to CuO. The foil was then taken out of the solution, rinsed with deionized water, and dried in air. X-ray photoelectron spectroscopy (XPS) analysis was carried out with an ECSALAB 250Xi high-performance electron spectrometer (Thermo Fisher Company). The porous Cu NRAs were protected against oxidation in air under Argon atmosphere while transferring it from electrolytic cell to the XPS machine. The morphology of the samples was analyzed by using scanning electron microscopy (SEM, Carl ZEISS Microscopy). The crystal structure was examined by using x-ray diffraction (XRD, Rigaku Miniflex II X-ray diffractometer, Cu $K_\alpha$ radiation).

### Electrochemical measurements and Product analysis

The potentiostatic electrolysis of $CO_2$ was carried out in a conventional three-electrode cell by using a potentiostat (Bio-Logic VMP3). A Pt foil and Ag/AgCl were used as the counter and reference electrode, respectively. All measured potentials were converted to the RHE reference scale using E (vs. RHE) = E (vs. Ag/AgCl) +0.210 +0.059×pH. During electrolysis, $CO_2$ gas (purity 99.999%) was bubbled through the aqueous 0.1 M $KHCO_3$ solution ($KHCO_3$ purity 99.7%) using a gas disperser. The gas and liquid products were analyzed using gas chromatography (GC) and $^1H$ nuclear magnetic resonance spectroscopy (NMR), the details of which can be found in our previous work.[7,17]

### A.3 Results and Discussions

**Schematic A.1b** illustrates the advantages of using ribbon arrays as the electrodes, including the rapid delivery of electrolyte into all the surface of the electrode, enhanced interaction between $CO_2$ and the Cu ribbon via the open structure of the arrays, fast one dimensional electronic transport, and presence of numerous active sites due to the roughened porous nature of Cu ribbons.

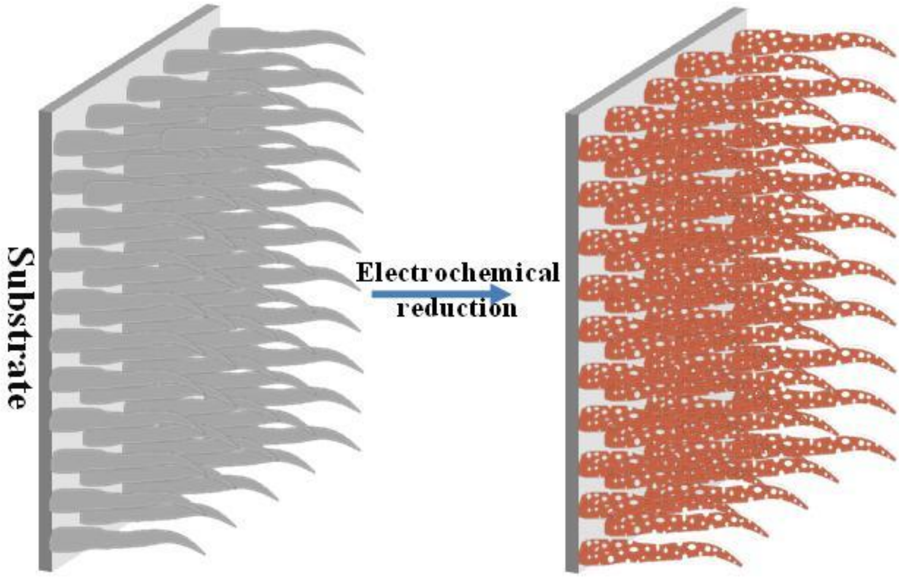

**(a)**

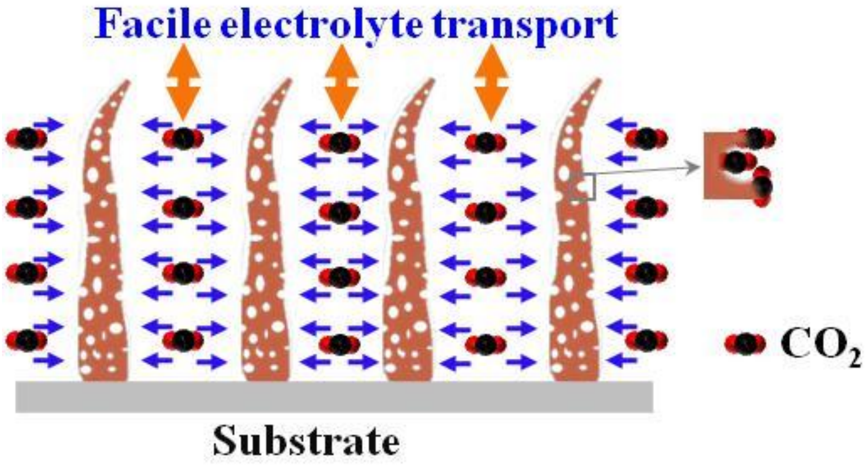

**(b)**

**Scheme A.1.** (a) A schematic showing the electrochemical process to fabricate Cu electrode (right hand side) comprised of nanoporous ribbon arrays from CuO (left hand side); and (b) a schematic showing the advantages of the nanoporous array electrode, including facile electrolyte transport and large number of active sites

**Figures A.1 (a) and (b)** show an SEM image and a Cu 2p XPS spectrum of the as-synthesized CuO NRAs, respectively. The SEM shows the CuO nanoribbons cover the surface uniformly and compactly. Moreover, the nanoribbons are aligned perpendicular to the copper substrate forming an array, which can reduce the diffusion resistance of the reactants and products.[18] The thickness of an individual nanoribbon was ~ 10 nm. The XRD pattern indicates the presence of a single monoclinic CuO phase, while cross-sectional SEM image shows the thickness of ~ 1.2 μm for NRAs film, consistent with our previous results.[15] The XPS spectra contain Cu $2p_{3/2}$ and $2p_{1/2}$ peaks at 933.6 and 953.4 eV, respectively. Characteristic shake-up satellite peaks are observed at ~ 9 eV higher in binding energy than the main $2p_{3/2}$ and $2p_{1/2}$ peaks, indicating the presence of CuO.[19]

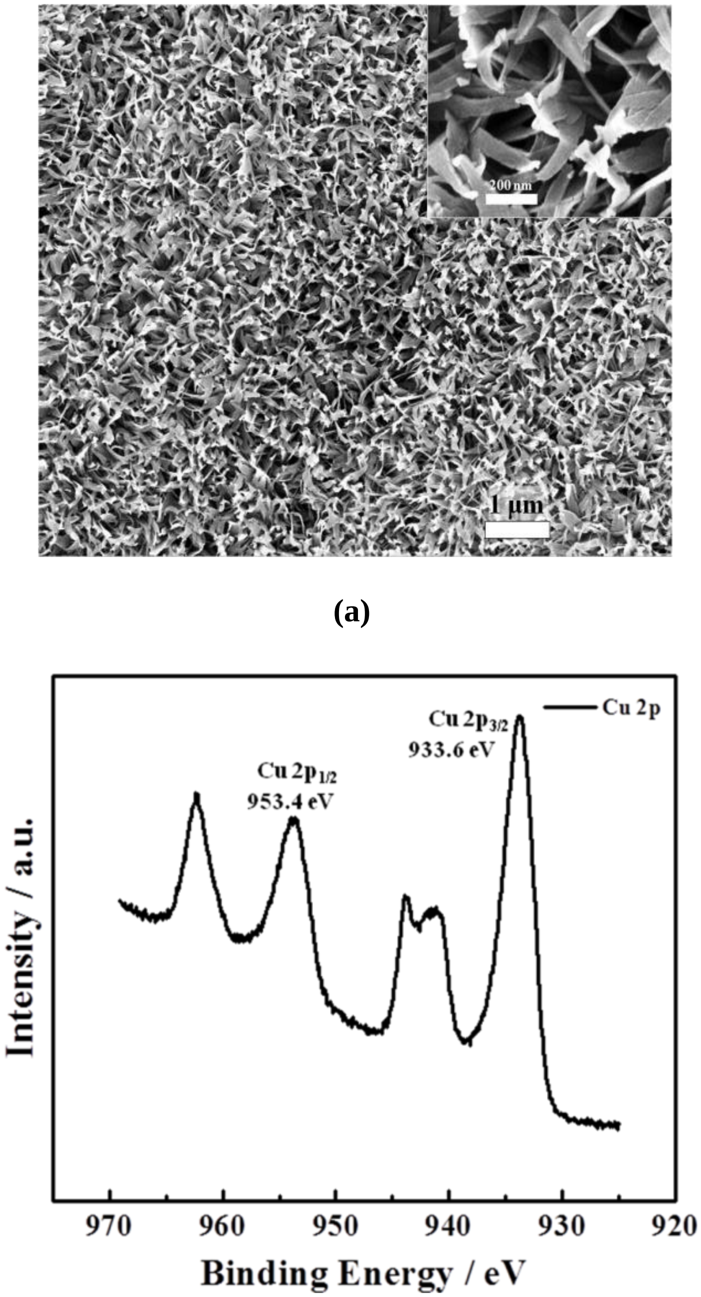

**(a)**

**(b)**

**Figure A.1.** (a) SEM image of CuO nanoribbon arrays. The inserted image is a high magnification image, showing individual ribbons. (b) Cu 2p XPS spectrum of CuO NRAs. Satellite peaks observed at ~ 9 eV higher in binding energy than the main $2p_{3/2}$ and $2p_{1/2}$ peaks, which correspond to CuO

These satellite peaks arise from the charge transfer transitions from the $O^{2-}$ ions into the unfilled ($d^9$) valence state of the $Cu^{2+}$ ion.[20] These charge transfer transitions are not allowed in cuprous oxides ($Cu_2O$) because of the filled ($d^{10}$) valence state configuration, thus causing the absence of satellite peaks.[21]

The chronoamperometric responses obtained during the electrochemical reduction of three different CuO NRA electrodes at -0.18 V are shown in **Figure A.2**. The current response of these electrodes was observed to match well with each other indicating the reproducibility of the electrodes. The current approached zero as an asymptote after 10 min, suggesting the complete transformation from CuO to Cu. Subsequent XRD measurements confirmed the presence of single phase copper. **Figure A.2** illustrates the current density during electroreduction of $CO_2$ as a function of time at various applied potentials. As expected the current density increases with increasing overpotential. This total current density reflects the contribution from both the hydrogen evolution reaction and $CO_2$ reduction happening at cathode. The Faradaic efficiencies for the products as a function of potential are shown in **Figure A.3.** At low overpotentials, the formation of CO and $HCOO^-$ is kinetically favorable because these products are formed by only two electron reduction.

$$CO_2 + 2H^+ + 2e^- \rightarrow CO + H_2O;\ \ E^0 = -0.10\,V\ vs.RHE$$

$$CO_2 + 2H^+ + 2e^- \rightarrow HCOOH;\quad E^0 = -0.20\,V\ vs.RHE$$

$$HCOOH \leftrightarrow HCOO^- + H^+;\quad At\,pH\ 7$$

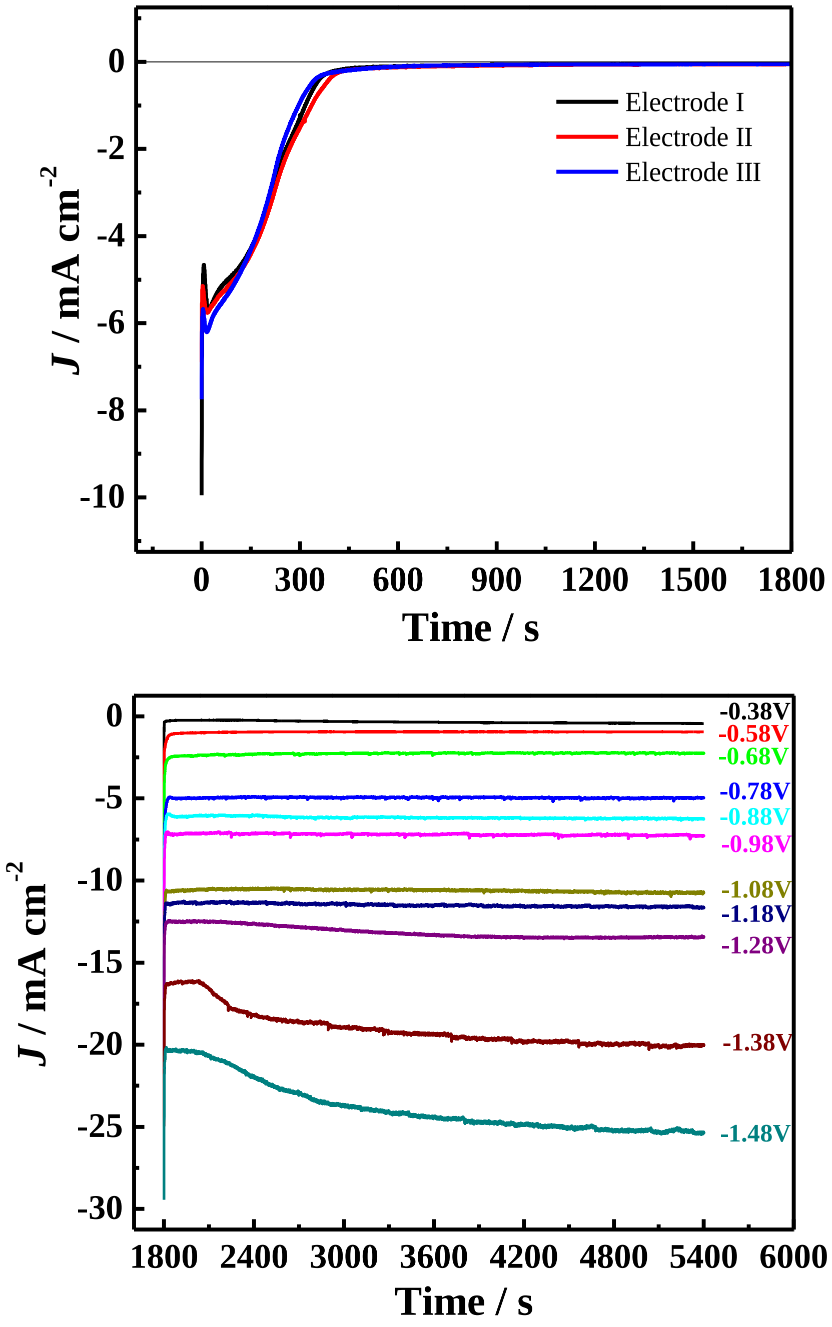

**Figure A.2.** Total current density vs. time for CuO NRAs at -0.18 V vs RHE. The total currents reach to zero, showing the complete conversion of CuO to Cu (Top). Total current density vs. time for $CO_2$ electrolysis on Cu electrodes comprised of nanoporous ribbon arrays under various potentials (Bottom).

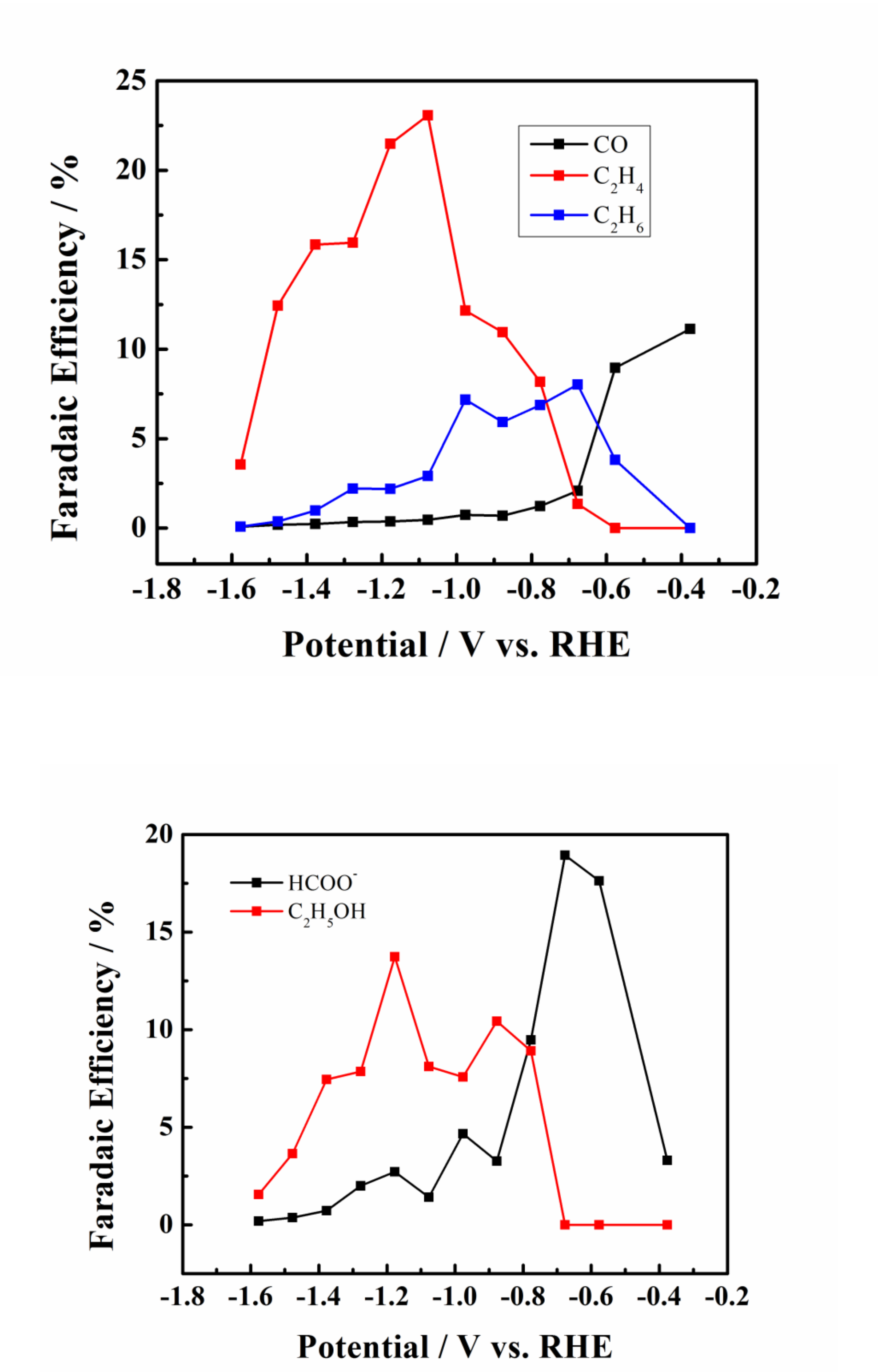

**Figure A.3.** Faradaic efficiencies towards the formation of CO, $C_2H_4$ and $C_2H_6$ vs. potential (Top). Faradaic efficiencies for liquid products ($HCOO^-$ and $C_2H_5OH$) vs. potential (Bottom).

At higher overpotentials, further reduction of CO becomes feasible and results in the formation of higher hydrocarbons.[10] Indeed, at potentials from -0.38 to -0.68 V, CO and $HCOO^-$ were primary products (~ 14% at -0.38 V, 21% at -0.68 V), while at more negative potentials $C_2H_4$ and $C_2H_5OH$ became the major products. The formation of $C_2H_4$, $C_2H_6$ and $C_2H_5OH$ necessitates a C-C coupling, which requires favorable reaction energetics and sufficient surface coverage of the pre-coupling intermediates.[10] The C-C coupling to form $C_2H_4$ and $C_2H_5OH$ started at -0.68 and -0.78 V, with an overpotential of ~ -0.75 and - 0.86 V, respectively. The highest Faradaic efficiencies for $C_2H_4$, $C_2H_6$, and $C_2H_5OH$ observed in our work were 23%, 7%, and 13.7% respectively. Previous experimental studies showed that the formation of $C_2$ products occurred via enol-like surface intermediates[10].

Unlike polycrystalline Cu foils as the electrode, $CH_4$ was not observed in gas products on our nanoporous Cu NRA electrodes. The primary gas products are $C_2H_6$ and $C_2H_4$. The increase in selectivity towards the formation of $C_2H_6$ and $C_2H_4$ is attributed to the difference in the surface copper arrangement of a smooth polycrystalline Cu foil and porous Cu nanoribbons. The selectivity of the nanoporous Cu NRAs in this work resulted in an unprecedented $C_2$ selectivity, producing more than double the Faradic efficiency toward $C_2$ at -0.80 V, compared to literature data.[5] The Cu nanoflowers showed an enhanced selectivity for $C_2H_4$ (~10%) compared with Cu foil (~2%). Copper electrodes comprised of nanoribbons are superior electrodes for the formation of $C_2$ products due to the presence of undercoordinated atoms and step sites on the roughened surfaces,[22] thus explaining larger selectivity towards $C_2H_4$ formation. The mechanism by which $C_2$ was formed has been carried out by several computational studies, which showed the stabilization of CHO* intermediates on step defected surfaces[22] led to the formation of hydrocarbons such as $C_2H_4$.[23]

In order to relate the surface properties of the catalyst with the selectivity, the structure of the Cu NRA electrode was analyzed after electrolysis. The SEM images in **Figure A.4** show that Cu nanoribbons maintained their alignment on the substrate after electrolysis. Additionally, small pores with a diameter 5-20 nm (inserted image in **Figure A.4**) were also observed. These pores were originated from the electrochemical reduction of CuO to Cu, where the monoclinic CuO is transformed to face-centered cubic Cu.[16] The electro-reduction of CuO NRA to Cu NRA can be described by the following two electrochemical reactions.[16]

$$At\ Cathode: \quad CuO + H_2O + 2e^- = Cu + 2OH^-$$

$$At\ Anode: \quad H_2O = 2H^+ + {}^1/_2\, O_2 + 2e^-$$

These pores offer a large number of active sites and facile electrolyte transport channels as illustrated in **Scheme A.1b**. The Cu 2p XPS spectrum (**Figure A.4**), which lacks shake-up satellite peaks, clearly shows the absence of CuO in the NRAs after electrolysis process. Therefore, the role of CuO on the electrochemical conversion of $CO_2$ in this work is negligible. **Figure A.4** alone, however, cannot differentiate the presence of Cu or $Cu_2O$. A thin layer (~ 1nm) of $Cu_2O$ might be present during $CO_2$ electrocatalysis on Cu electrodes.

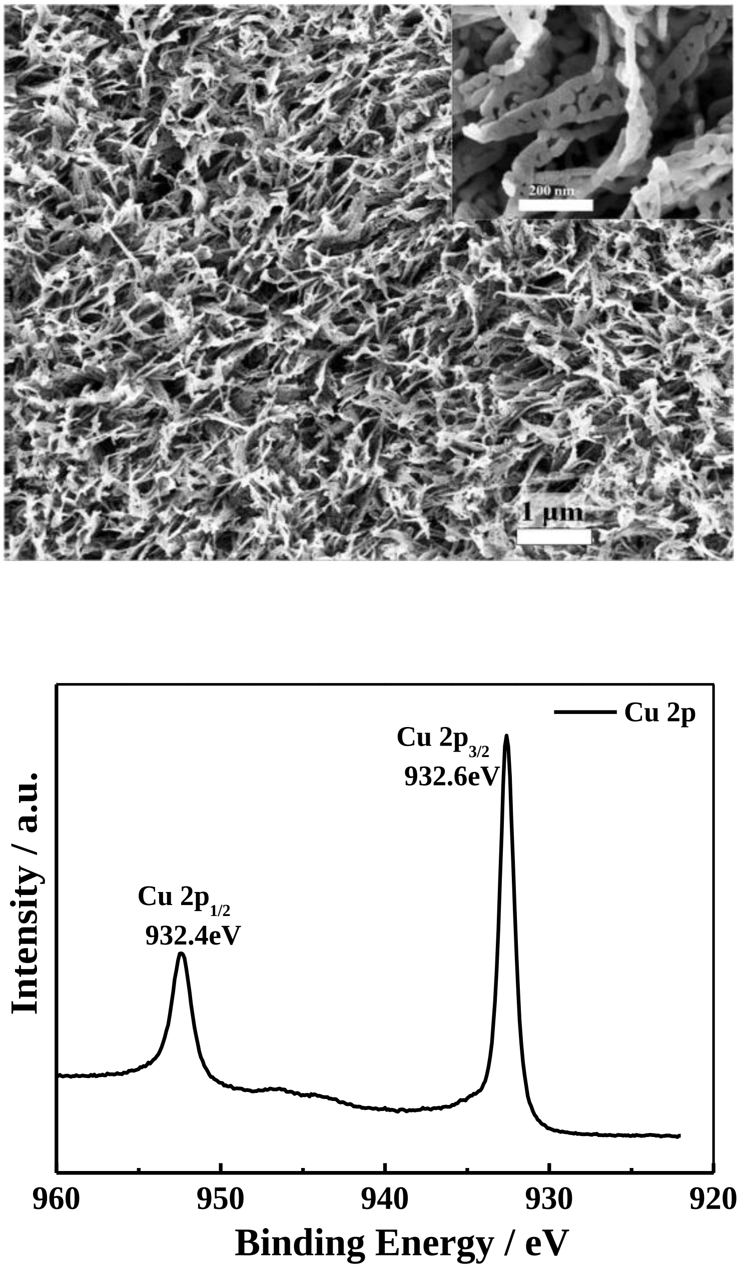

**Figure A.4.** SEM image of Cu nanoribbon arrays. The inserted is a high magnification image showing the presence of numerous nanosized pores (Top). XPS spectrum of Cu electrode after electrolysis (Bottom).

## A.4 Conclusions

In summary, 3-D nanoporous Cu electrodes were synthesized by electrochemically reducing CuO nanoribbon arrays. The roughened porous channels of these electrodes allowed for facile diffusion of electrolyte and provided large number of active step sites for $CO_2$ reduction. This type of copper electrode exhibited a selective formation of $C_2$ products ($C_2H_4$, $C_2H_6$ and $C_2H_5OH$) from $CO_2$ electroreduction. The C-C coupling is promoted at potentials < -0.78 V vs. RHE with $C_2H_4$ and $C_2H_5OH$ as major products while suppressing the formation of $C_1$ products ($CH_4$, CO, and $HCOO^-$). The highest observed current efficiencies for $C_2H_4$ and $C_2H_5OH$ were ~ 23% and ~ 13% at -1.18 V vs. RHE, respectively. The synthetic route for the preparation of these nanoporous architectures can potentially provide an effective method to engineer the porosity and surface area of catalysts.

## References

1. Frese, K. W.; Leach, S. *Journal of The Electrochemical Society* **1985,** 132, (1), 259-260.
2. Summers, D. P.; Frese, K. W. *Langmuir* **1988,** 4, (1), 51-57.
3. Hori, Y.; Vayenas, C. G.; White, R. E.; Gamboa-Aldeco, M. E., *Modern Aspects of Electrochemistry*. 2008; Vol. 42, p 89.
4. Rosen, B. A.; Salehi-Khojin, A.; Thorson, M. R.; Zhu, W.; Whipple, D. T.; Kenis, P. J. A.; Masel, R. I. *Science* **2011,** 334, (6056), 643-644.
5. Li, C. W.; Kanan, M. W. *Journal of the American Chemical Society* **2012,** 134, (17), 7231-7234.
6. Peterson, A. A.; Nørskov, J. K. *The Journal of Physical Chemistry Letters* **2012,** 3, (2), 251-258.
7. Wu, J. J.; Risalvato, F. G.; Ke, F. S.; Pellechia, P. J.; Zhou, X. D. *Journal of the Electrochemical Society* **2012,** 159, (7), F353-F359.
8. Chen, Z.; Kang, P.; Zhang, M.-T.; Stoner, B. R.; Meyer, T. J. *Energy & Environmental Science* **2013,** 6, (3), 813-817.
9. Hori, Y.; Kikuchi, K.; Suzuki, S. *Chemistry Letters* **1985,** 14, (11), 1695-1698.
10. Kuhl, K. P.; Cave, E. R.; Abram, D. N.; Jaramillo, T. F. *Energy & Environmental Science* **2012,** 5, (5), 7050-7059.
11. Murata, A.; Hori, Y. *Bull. Chem. Soc. Jpn* **1991,** 64, 123.
12. Hara, K.; Tsuneto, A.; Kudo, A.; Sakata, T. *Journal of Electroanalytical Chemistry* **1997,** 434, (1–2), 239-243.
13. Hori, Y.; Takahashi, I.; Koga, O.; Hoshi, N. *The Journal of Physical Chemistry B* **2001,** 106, (1), 15-17.
14. Xie, J.-F.; Huang, Y.-X.; Li, W.-W.; Song, X.-N.; Xiong, L.; Yu, H.-Q. *Electrochimica Acta* **2014,** 139, (0), 137-144.
15. Ke, F.-S.; Huang, L.; Wei, G.-Z.; Xue, L.-J.; Li, J.-T.; Zhang, B.; Chen, S.-R.; Fan, X.-Y.; Sun, S.-G. *Electrochimica Acta* **2009,** 54, (24), 5825-5829.
16. Ke, F.-S.; Huang, L.; Solomon, B. C.; Wei, G.-Z.; Xue, L.-J.; Zhang, B.; Li, J.-T.; Zhou, X.-D.; Sun, S.-G. *Journal of Materials Chemistry* **2012,** 22, (34), 17511-17517.
17. Wu, M.; Sabisch, J. E. C.; Song, X.; Minor, A. M.; Battaglia, V. S.; Liu, G. *Nano Letters* **2013,** 13, (11), 5397-5402.
18. Wu, J.; Sharma, P. P.; Harris, B. H.; Zhou, X.-D. *Journal of Power Sources* **2014,** 258, (0), 189-194.
19. Poulston, S.; Parlett, P. M.; Stone, P.; Bowker, M. *Surface and Interface Analysis* **1996,** 24, (12), 811-820.
20. Kim, K. S. *Journal of Electron Spectroscopy and Related Phenomena* **1974,** 3, (3), 217-226.
21. Hernandez, J.; Wrschka, P.; Oehrlein, G. S. *Journal of The Electrochemical Society* **2001,** 148, (7), G389-G397.
22. Tang, W.; Peterson, A. A.; Varela, A. S.; Jovanov, Z. P.; Bech, L.; Durand, W. J.; Dahl, S.; Norskov, J. K.; Chorkendorff, I. *Physical Chemistry Chemical Physics* **2012,** 14, (1), 76-81.
23. Peterson, A. A.; Abild-Pedersen, F.; Studt, F.; Rossmeisl, J.; Norskov, J. K. *Energy & Environmental Science* **2010,** 3, (9), 1311-1315.

# Appendix B: Electrocatalytic Activity of Rutile Titanium Dioxide towards the Conversion of Carbon Dioxide to CO and Formate

## B.1 Introduction

Electrochemical fixation of $CO_2$ offers a promising route for recycling $CO_2$ from the atmosphere over a wide temperature region. While high temperature (600 – 900ºC) $CO_2$ conversion is thermodynamically in favor of the formation of CO,[26] low temperature (25 – 100°C) electrolysis provides an alternative to form a variety of products, both gases (CO, $CH_4$, $C_2H_4$, $C_2H_6$) and liquids ($HCO_2H$, $CH_3OH$, $C_2H_5OH$). Furthermore, low temperature conversion of $CO_2$ enables the use of proton exchange membrane (PEM) electrolyzer, which has the potential to convert $CO_2$ to fuels at a large scale in a cost effective manner.

Metallic catalysts have been extensively investigated for their electrocatalytic activity for $CO_2$ reduction. Metals such as Sn and Cu, on one hand offer reasonable selectivity and current efficiency (>70%), [27-29] however, suffer from poor stability with a profound degradation in electrocatalytic activity during several hours of operation. On the other hand, mixture of conductive metal oxides such as $RuO_2$ based catalysts while demonstrate good stability (> 40 hours), but lack high current densities (<1 $mA/cm^2$).[30] Metals such as Cu and Au derived from micron thick $Cu_2O$ and Au oxide films respectively have been reported to exhibit superior activity and stability than the respective polycrystalline metal electrodes.[5,31] The role of the native oxide layer present on a metal surface towards electrocatalytic conversion of $CO_2$ has also been reported. For example, the oxide ($SnO_x$) layer over Sn surface has been shown to play a major role in efficient $CO_2$ reduction.[32] In spite of these recent developments, however, $CO_2$ reduction research still continues to pursue an efficient and durable catalyst.

Titanium dioxide ($TiO_2$) has been widely studied in the field of heterogeneous catalysis as a support material due to its ability to facilitate strong-metal support interaction;[33] and as a photocatalyst, because of its tunable bandgap, effective charge separation and adsorption of water, oxygen and organic molecules.[34] Anatase $TiO_2$ is known to exhibit superior photocatalytic properties than rutile phase mainly because of a lower recombination rate of electron-holes pair in anatase.[35] On the other hand, the role of polymorphic phases of $TiO_2$ on the electrocatalytic activity is unknown, in particular towards the conversion of $CO_2$ to fuels. In this present work, $TiO_2$ is reported as a possible electrocatalyst for $CO_2$ reduction. The electrocatalytic activity of $TiO_2$ for $CO_2$ reduction is observed to substantially depend on its crystal structure. A much higher electrocatalytic activity of rutile phase than anatase for $CO_2$ reduction was observed, which contradicts the widely reported significantly higher photocatalytic activity of anatase than rutile phase.

## B.2 Experimental

**Materials & Characterization –** Aeroxide $TiO_2$ P25 nanoparticles were procured from Evonik, while $TiO_2$ anatase (99.8% purity) was obtained from Sigma Aldrich. Rutile $TiO_2$ was prepared by annealing $TiO_2$ P25 nanoparticles at 1100°C for 1 h. These samples were characterized by X-ray diffraction (XRD) using Cu $K_\alpha$ (1.5418 A.U.)

radiation in the Rigaku Miniflex II, benchtop X-ray diffractometer from 20 – 80° at a scan speed of 3°/min. BET measurements were done with $N_2$ sorption at 77 K using Micrometrics ASAP 2020 surface area analyzer. High-resolution transmission electron microscopy (HRTEM) images were acquired with a JEM-2100 F TEM with a field-emission gun. X-ray photoelectron spectroscopy (XPS) measurements were obtained using Al $K_\alpha$ monochromatic source in a XPS, Kratos Axis Ultra DLD with hemispherical energy analyzer. Accurate binding energies (±0.1 eV) were determined with respect to the position of C 1s peak observed at 284.8 eV.

**Electrochemical Measurements –** The gas diffusion electrodes (GDEs) for cathode side were prepared by spraying the $TiO_2$ catalyst ink over the gas diffusion layer (GDL). The catalyst ink was prepared by ultrasonicating a mixture of $TiO_2$ particles, Nafion ionomer solution, water and isopropanol for about 1 h. The geometric area of the GDE was 4 $cm^2$. Catalyst loading was calculated from weighing the GDL before and after spraying and drying the catalyst layer. These various $TiO_2$ GDEs were tested for their electrocatalytic activity for $CO_2$ reduction in a proton exchange membrane (PEM) electrolyzer with 0.1 M $KHCO_3$ electrolyte solution having an ohmic resistance of ~ 25 $\Omega$-$cm^2$. Further details of the fabrication of membrane electrode assembly (MEA) and design of the electrochemical cell can be found in our previous work.[17] The operating conditions of the cell were ambient temperature and pressure, i.e., T=298.15K and $P^o$ =1.013 bar. The electrolyte was pumped at 5 mL/min. The anode side of the full electrochemical cell was supplied with $H_2$ at a flow rate of 150 mL/min, while cathode was supplied with $CO_2$ at 45 mL/min. This full electrochemical cell was controlled by Solartron 1470E potentiostat/galvanostat and operated in the potentiostatic mode. The average current was calculated by dividing the total charge passed by the time of electrolysis. The electrolysis was conducted for 0.5 h in the potential range, -1 to -2.5 V.

**Products Quantification –** The gas and the liquid products of $CO_2$ reduction were analyzed using gas chromatography (GC) and $^1$H nuclear magnetic resonance (NMR) spectroscopy, respectively. The method details and procedure to calculate the faradaic efficiency for different products have been addressed elsewhere.[17,36]

## B.3 Results & Discussion

Initial research focused on the investigation of the activities of polymorphic $TiO_2$ by incorporating different $TiO_2$ electrodes in the full electrochemical cell with 0.1 M $KHCO_3$ as the buffer layer. **Figure B.1** shows the XRD patterns of various $TiO_2$ samples studied in this work. The weight fractions of anatase and rutile in these samples were calculated using the empirical equation described by Spurr and Myres.[37]

$W_R/W_A = 1.22*I_R/I_A – 0.028$where $W_R$ and $W_A$ are the respective weight fractions for rutile and anatase, while $I_R$ and $I_A$ denote the intensity of observed rutile (110) peak at 27.35° and anatase (101) peak at 25.16° 2θ, respectively. The crystallite size was also calculated for these powders using Scherrer's equation, ($d = 0.9*\lambda/\beta*\cos\theta$, where d is the crystallite size; λ, X-ray wavelength; β, the full width at half maximum; and θ, the diffraction angle) based on the observed first diffraction peak, i.e., 25.16° for anatase and 27.35° for rutile.

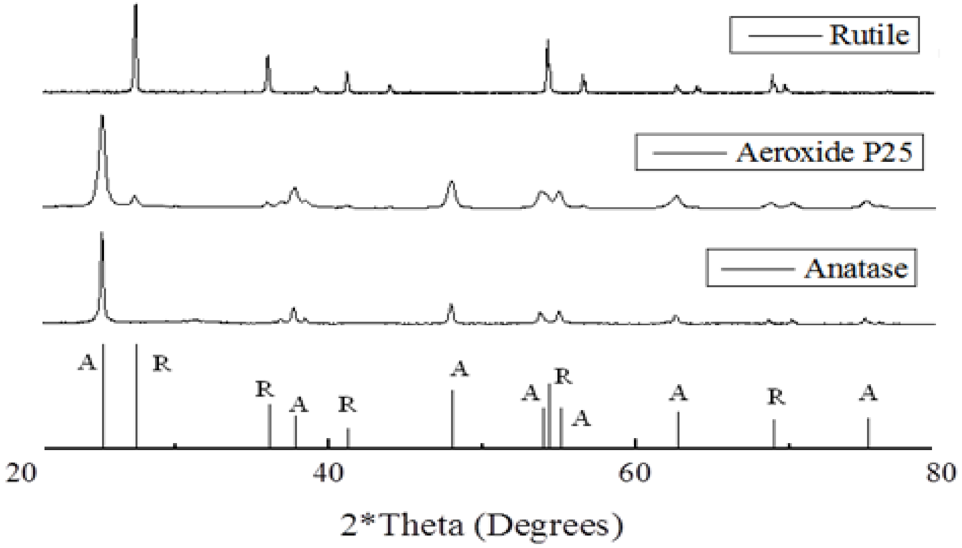

**Figure B.1.** XRD patterns of various $TiO_2$ samples studied in this work. Vertical lines represent the standard diffractions observed for anatase (JCPDS # 71-1167) and rutile (JCPDS # 88-1172) phases denoted by A and R respectively

**Table B.1.** Phase composition, crystallite size, BET surface area and catalyst loading of various $TiO_2$ samples

| **Sample** | **Phase composition (weight %)** | **Crystallite size (nm)** | **BET surface area ($m^2$/g)** | **Catalyst loading ($mg/cm^2$)** |
|---|---|---|---|---|
| Anatase | 99.7% anatase,<br>0.3% rutile | 34 | 15.09 | 1.76 |
| Aeroxide P25 | 87.5% anatase,<br>12.5% rutile | 18 | 38.75 | 2.14 |
| Rutile | 1.6% anatase,<br>98.4% rutile | 51 | 2.24 | 1.52 |

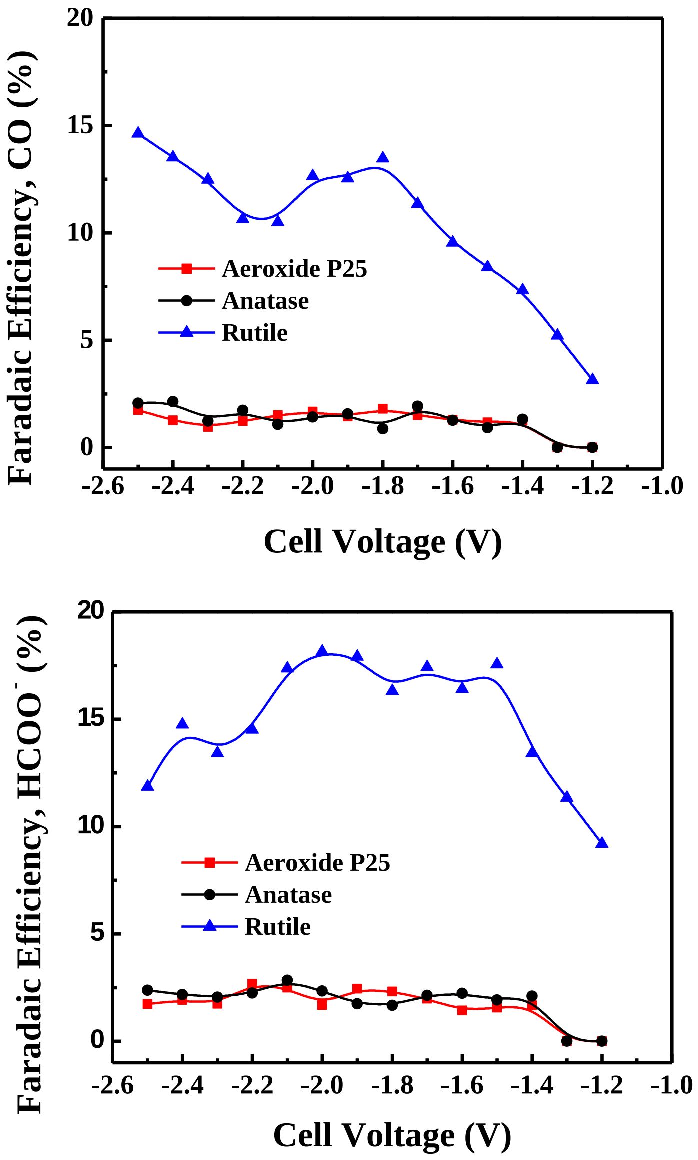

**Figure B.2.** Faradaic efficiency vs. cell voltage for CO and HCOO- on various $TiO_2$ electrodes

The phase compositions, crystallite size have been listed in **Table B.1** along with the BET surface area and the catalyst loading of these $TiO_2$ samples. $CO_2$ electro-reduction is known to compete with hydrogen evolution reaction, and therefore, the total current density reflects the formation of products from $CO_2$ reduction along with hydrogen formation at cathode. A much higher electrocatalytic activity of rutile than P25 particles towards $CO_2$ reduction was initially observed for both CO and HCOO-. **Figure B.2** illustrates the Faradaic efficiencies for various electrolysis products, i.e., CO, $HCOO^-$ and $H_2$ as a function of cell voltage on anatase and rutile $TiO_2$ electrodes. $CO_2$ reduction starts at -1.1 V on rutile $TiO_2$, yielding CO and $HCOO^-$ with Faradaic efficiencies of ~ 6.5 and 3% respectively. On the other hand, CO and $HCOO^-$ were detected at cell voltages more negative to -1.6 V on the anatase $TiO_2$ electrode. The Faradaic efficiencies for CO and HCOO- reached a maximum of ~ 20% at -2.5 V for rutile $TiO_2$ while being only ~3% for anatase. Inconsistencies in measurements of Faradaic efficiency for $H_2$ at low cell voltages (< -1.4 V) were observed because of difficulties in accurately measuring very low concentrations of $H_2$ using the GC.

XRD measurements of the $TiO_2$ electrodes were done in order to notice any structural changes in $TiO_2$ before and after electrolysis. The XRD peaks, however, were identical suggesting that bulk structure was intact during electrolysis. On the other hand, the XPS measurements as seen in **Figure B.3** show a decrease in the binding energy of Ti $2p_{3/2}$ peaks after electrolysis. The binding energies of Ti $2p_{3/2}$ and Ti $2p_{1/2}$ peak change from 459.4 to 458.4 eV and from 465 to 464.2 eV respectively after electrolysis suggesting the presence of surface defects. A wide range of binding energies, i.e., 459.3 to 458.5 eV, attributing to the presence of $Ti^{4+}$ ions has been reported in literature. The presence of surface defects can cause the rigid shift of the whole XPS spectrum which results in the above discrepancy. This slightly reduced $TiO_2$ provides surface defects, i.e. $Ti^{3+}$ and oxygen vacancies ($V_o$), thereby increasing the active sites for $CO_2$ adsorption and dissociation. Though the surface defects are observed to be present on both anatase and rutile, the electrocatalytic activity of rutile is still observed to be much higher than anatase. This suggests that the presence of surface defects alone can't explain the observed trend in the catalytic activity. In addition, the surface structure plays a major role in catalytic reactions.[16-17] The most stable surface of rutile is (110) [34] while (101) for anatase.[18] The (110) rutile surface exhibits the highest atomic density for titanium (10.2 $Ti/nm^2$)[19] and the number of co-ordinative unsaturated sites for anatase surfaces vary from 4-7 $Ti/nm^2$. Rutile (110) surface is relatively easy to reduce in comparison to anatase (101) surface resulting in formation of higher number of surface defects over rutile (110) surface. $Ti^{3+}$ surface defect is known to be responsible electrocatalytic active site for $CO_2$ reduction. This relatively higher atomic density of Ti ions along with the oxygen vacancies in the reduced (110) rutile surface contributes to more number of active sites and hence significantly improves the electrocatalytic activity for $CO_2$ reduction. The ideal $TiO_2$ (110) rutile surface consists of alternating rows of fivefold-coordinated titaniums ($Ti_{5c}$) and protruding twofold-coordinated bridging oxygens ($O_b$). The $O_b$ vacancies and $Ti_{5c}$ sites play crucial role in surface reactions.[20] The interaction of $CO_2$, either in isolation or together with other species, with $TiO_2$ rutile (110) surface has been studied.[21-23] Both $O_b$ vacancies and $Ti_{5c}$ sites have been discovered to play a major role in the adsorption of $CO_2$. The two configurations in which $CO_2$ can adsorb on $Ti_{5c}$ sites are tilted monodentate and flat bidentate[38]. Similarly, two adsorption configurations of $CO_2$ have been identified at $O_b$ vacancies with the more stable being the one involving $CO_2$ adsorption in a tilted arrangement.[24] On the other hand, anatase (101) surface is widely known to be unreactive. Molecules such as water and other organics have been observed to adsorb but not dissociate on the anatase (101) surface.[25-27]

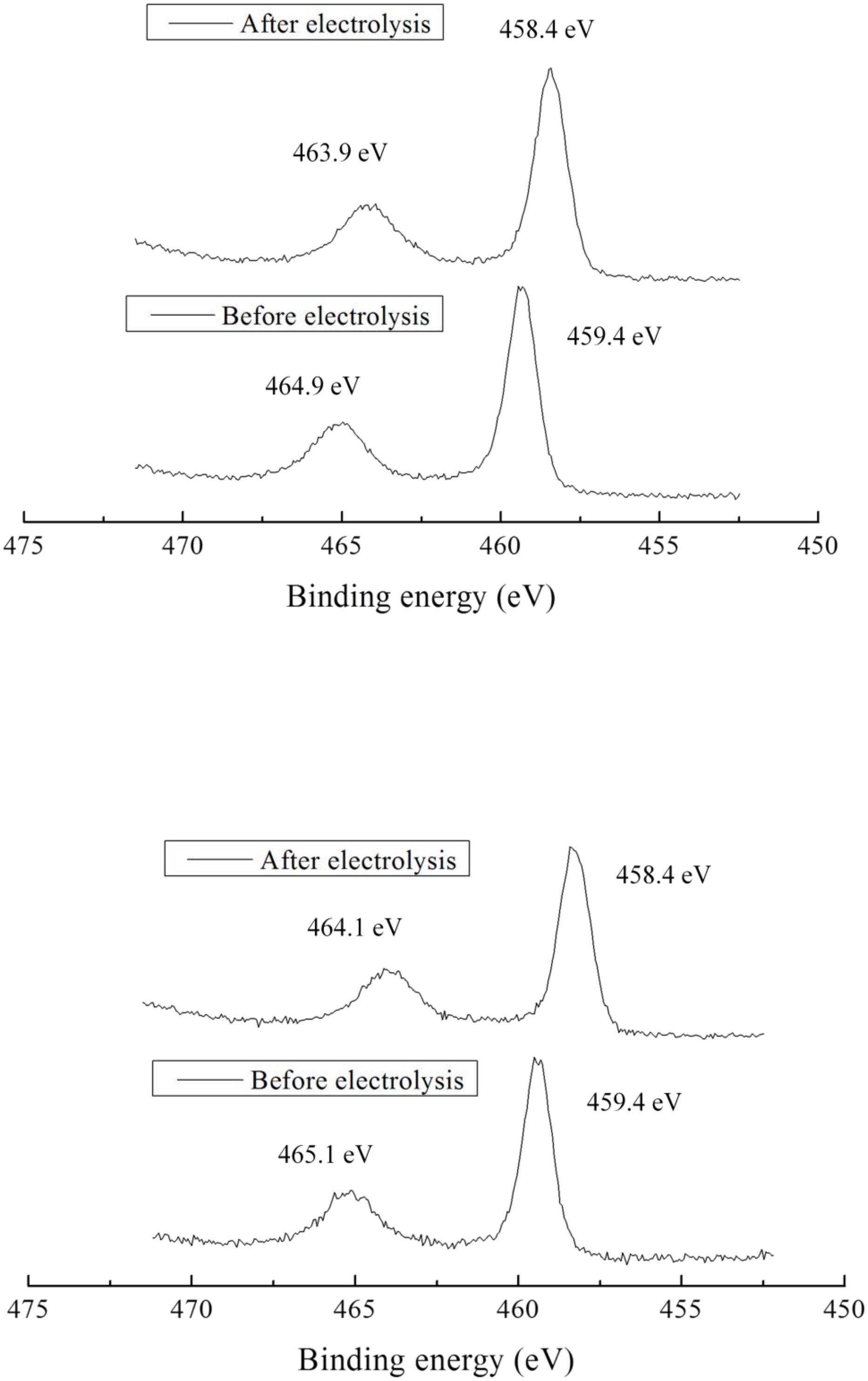

**Figure B.3.** XPS results before and after electrolysis for anatase (top) and rutile (bottom) $TiO_2$ electrodes

Theoretical investigations have been done to understand the mechanism of electrochemical reduction of $CO_2$ on metallic catalysts. The protonation of adsorbed CO is proposed to be rate limiting for the production of hydrocarbons on Cu electrodes. In the case of metal oxides as electrocatalyst, the one electron activation of $CO_2$, however, appears to be rate limiting on anatase but can be promoted on rutile. In order to validate this hypothesis, tafel data was extracted from the $CO_2$ electrolysis experiments. The tafel slopes for CO and HCOO- were found to be 320 and 204 mV/dec suggesting the one electron transfer activation of $CO_2$ to be the rate limiting step of $CO_2$ electro-reduction.[28] Scanning tunneling microscopy (STM) has been used to further understand this electron transfer to $CO_2$ molecule on $TiO_2$ (110) surface[29]. The formation of a metastable $CO_2^-$ anion ocurs at the $V_o$ site, which further dissociates releasing an oxygen atom which in turn, heals the oxygen vacancy.[29] In another plausible scheme, $CO_2$ interacts with $Ti^{3+}$ to form $CO_2^-$ which further dissociates to CO via reaction with $H^+$, self tranformation or direct dissociation by healing the oxygen vacancy sites.[30] The intermediate $CO_2^-$ anion formed can also undergo protonation followed by a second electron transfer to yield formate.[30]

## B.4 Conclusions

In summary, the electrocatalytic activity of $TiO_2$ for $CO_2$ reduction is demonstrated in a full electrochemical cell. The electrocatalytic activity is observed to strongly depend on the crystal structure and in particular the surface structure of $TiO_2$. Rutile $TiO_2$ is found to exhibit a much higher electrocatalytic activity towards $CO_2$ reduction than anatase. $TiO_2$ can be reduced at the surface on applying negative potentials as seen from the XPS measurements; however, bulk structure is retained. The reduced $TiO_2$ surface can provide more active sites for molecules adsorption and dissociation. $TiO_2$ rutile reduced at the surface can provide more active sites, i.e., oxygen vacancies and fivefold-coordinated Ti; and therefore might be a potential catalyst for electron transfer reactions.

## References

(1) Frese, K. W.; Leach, S. *Journal of The Electrochemical Society* **1985**, *132*, 259.

(2) Summers, D. P.; Frese, K. W. *Langmuir* **1988**, *4*, 51.

(3) Hori, Y.; Vayenas, C. G.; White, R. E.; Gamboa-Aldeco, M. E. *Modern Aspects of Electrochemistry*, 2008; Vol. 42.

(4) Rosen, B. A.; Salehi-Khojin, A.; Thorson, M. R.; Zhu, W.; Whipple, D. T.; Kenis, P. J. A.; Masel, R. I. *Science* **2011**, *334*, 643.

(5) Li, C. W.; Kanan, M. W. *Journal of the American Chemical Society* **2012**, *134*, 7231.

(6) Peterson, A. A.; Nørskov, J. K. *The Journal of Physical Chemistry Letters* **2012**, *3*, 251.

(7) Wu, J. J.; Risalvato, F. G.; Ke, F. S.; Pellechia, P. J.; Zhou, X. D. *Journal of the Electrochemical Society* **2012**, *159*, F353.

(8) Chen, Z.; Kang, P.; Zhang, M.-T.; Stoner, B. R.; Meyer, T. J. *Energy & Environmental Science* **2013**, *6*, 813.

(9) Hori, Y.; Kikuchi, K.; Suzuki, S. *Chemistry Letters* **1985**, *14*, 1695.

(10) Kuhl, K. P.; Cave, E. R.; Abram, D. N.; Jaramillo, T. F. *Energy & Environmental Science* **2012**, *5*, 7050.

(11) Murata, A.; Hori, Y. *Bull. Chem. Soc. Jpn* **1991**, *64*, 123.

(12) Hara, K.; Tsuneto, A.; Kudo, A.; Sakata, T. *Journal of Electroanalytical Chemistry* **1997**, *434*, 239.

(13) Hori, Y.; Takahashi, I.; Koga, O.; Hoshi, N. *The Journal of Physical Chemistry B* **2001**, *106*, 15.

(14) Xie, J.-F.; Huang, Y.-X.; Li, W.-W.; Song, X.-N.; Xiong, L.; Yu, H.-Q. *Electrochimica Acta* **2014**, *139*, 137.

(15) Ke, F.-S.; Huang, L.; Wei, G.-Z.; Xue, L.-J.; Li, J.-T.; Zhang, B.; Chen, S.-R.; Fan, X.-Y.; Sun, S.-G. *Electrochimica Acta* **2009**, *54*, 5825.

(16) Ke, F.-S.; Huang, L.; Solomon, B. C.; Wei, G.-Z.; Xue, L.-J.; Zhang, B.; Li, J.-T.; Zhou, X.-D.; Sun, S.-G. *Journal of Materials Chemistry* **2012**, *22*, 17511.

(17) Wu, J.; Risalvato, F. G.; Sharma, P. P.; Pellechia, P. J.; Ke, F.-S.; Zhou, X.-D. *Journal of The Electrochemical Society* **2013**, *160*, F953.

(18) Wu, J.; Sharma, P. P.; Harris, B. H.; Zhou, X.-D. *Journal of Power Sources* **2014**, *258*, 189.

(19) Poulston, S.; Parlett, P. M.; Stone, P.; Bowker, M. *Surface and Interface Analysis* **1996**, *24*, 811.

(20) Kim, K. S. *Journal of Electron Spectroscopy and Related Phenomena* **1974**, *3*, 217.

(21) Hernandez, J.; Wrschka, P.; Oehrlein, G. S. *Journal of The Electrochemical Society* **2001**, *148*, G389.

(22) Tang, W.; Peterson, A. A.; Varela, A. S.; Jovanov, Z. P.; Bech, L.; Durand, W. J.; Dahl, S.; Norskov, J. K.; Chorkendorff, I. *Physical Chemistry Chemical Physics* **2012**, *14*, 76.

(23) Peterson, A. A.; Abild-Pedersen, F.; Studt, F.; Rossmeisl, J.; Norskov, J. K. *Energy & Environmental Science* **2010**, *3*, 1311.

(24) Li, C. W.; Ciston, J.; Kanan, M. W. *Nature* **2014**, *508*, 504.

(25) Zuo, Z.-J.; Li, J.; Han, P.-D.; Huang, W. *The Journal of Physical Chemistry C* **2014**, *118*, 20332.

(26) Ebbesen, S. D.; Mogensen, M. *Journal of Power Sources* **2009**, *193*, 349.

(27) Hori, Y.; Wakebe, H.; Tsukamoto, T.; Koga, O. *Electrochimica Acta* **1994**, *39*, 1833.

(28) Hori, Y.; Kikuchi, K.; Suzuki, S. *Chemistry Letters* **1985**, *14*, 1695.

(29) Hori, Y. In *Modern Aspects of Electrochemistry*; Vayenas, C., White, R., Gamboa-Aldeco, M., Eds.; Springer New York: 2008; Vol. 42, p 89.

(30) Bandi, A. *Journal of The Electrochemical Society* **1990**, *137*, 2157.

(31) Chen, Y.; Li, C. W.; Kanan, M. W. *Journal of the American Chemical Society* **2012**, *134*, 19969.

(32) Chen, Y.; Kanan, M. W. *Journal of the American Chemical Society* **2012**, *134*, 1986.

(33) Haller, G. L.; Resasco, D. E. In *Advances in Catalysis*; D.D. Eley, H. P., Paul, B. W., Eds.; Academic Press: 1989; Vol. Volume 36, p 173.

(34) Diebold, U. *Surface Science Reports* **2003**, *48*, 53.

(35) Hurum, D. C.; Agrios, A. G.; Gray, K. A.; Rajh, T.; Thurnauer, M. C. *The Journal of Physical Chemistry B* **2003**, *107*, 4545.

(36) Wu, J.; Risalvato, F. G.; Ke, F.-S.; Pellechia, P. J.; Zhou, X.-D. *Journal of The Electrochemical Society* **2012**, *159*, F353.

(37) Spurr, R. A.; Myers, H. *Analytical Chemistry* **1957**, *29*, 760.

(38) Sorescu, D. C.; Lee, J.; Al-Saidi, W. A.; Jordan, K. D. *The Journal of Chemical Physics* **2011**, *134*.

# Appendix C: The Role of Nonstoichiometry on the Electrocatalytic Properties of $TiO_{2-x}$ towards the Conversion of Carbon Dioxide to Fuels

## C.1 Introduction

Titanium is found to exist in a number of suboxide forms with a general formula $Ti_nO_{2n-1}$, known as Magneli phases where n ranges from 4 to 10.[1] The Magneli phases derive their respective crystal structures through a crystallographic shear from the rutile structure. Presently, these oxides are synthesized by controlled oxidation of titanium or by high temperature reduction of $TiO_2$.[2] These titanium suboxides have attracted attention because of their high electrical conductivity and chemical stability in harsh acidic and alkaline environments.[3] For example, these non-stoichiometric oxides have been studied as potential catalysts, electrochemical components, biocompatible coatings, electroconducting ceramics for several applications.[2] Out of these various titanium suboxides, $Ti_3O_5$ has been studied for solar cells and photocatalytic applications.[4]

In this current study, $Ti_3O_5$ was further investigated as the possible electrocatalysts for $CO_2$ electro-reduction in a polymer exchange membrane fuel cell (PEMFC) based full electrochemical cell. $Ti_3O_5$ was first synthesized from $TiO_2$ P25 nanoparticles by reducing it under hydrogen environment. To understand the role of nonstoichiometry, stoichiometric oxides of titanium, i.e. TiO and $TiO_2$ were also studied for their electrocatalytic activity towards $CO_2$ reduction. A much higher electrocatalytic activity was observed for the formation of CO and formate with $Ti_3O_5$. This increase in catalytic activity of nonstoichiometric titania is attributed to the formation of defects such as $Ti^{3+}$ and oxygen vacancies during hydrogen treatment.

## C.2 Experimental

**Materials & Characterization –** $TiO_2$ P25 nanoparticles were procured from Evonik, while TiO (99.9% purity) was obtained from Sigma Aldrich. $Ti_3O_5$ was prepared by reduction of $TiO_2$ P25 nanoparticles in hydrogen environment at 900°C for 72 hours in a tubular flow reactor. This temperature condition was rationalized by a systematic time-dependent study of $TiO_2$ reduction under hydrogen atmosphere at various temperatures. The powders were ball milled with yttria stabilized zirconia (YSZ), 2 mm spherical beads. These samples were characterized by X-ray diffraction (XRD) using Cu $K_\alpha$ (1.5418 A.U.) radiation in the Rigaku Miniflex II, benchtop X-ray diffractometer from 20 – 80° at a scan speed of 3°/min. BET measurements were done with $N_2$ sorption at 77 K using Micrometrics ASAP 2020 surface area analyzer.

**Electrochemical Measurements –** The gas diffusion electrodes (GDEs) for cathode were prepared by spraying catalyst ink over the gas diffusion layer (GDL). Catalyst ink composition included catalyst particles, DI water, isopropyl alcohol and 20 wt%. Nafion ionomer. The geometric area of the GDE used was 4 $cm^2$. Catalyst loading was calculated from weight measurements before and after spraying the catalyst onto GDL. The other details of the fabrication of membrane electrode assembly (MEA) and design of the electrochemical cell can be found in the previous work.[5] The electrolysis cell was controlled by Solartron 1470E potentiostat/galvanostat and operated in the potentiostatic mode. The total average current was calculated by dividing the total charge passed in coulombs by the time of electrolysis in seconds. The electrolysis was started at a cell voltage of -1 V and then moved at higher negative cell voltages till -2.5 V with step size of 0.1 V. The electrolysis time was 0.5 hr at each voltage.

**Product Quantification –** The gas and the liquid products of $CO_2$ reduction were analyzed using gas chromatography (GC) and $^1$H nuclear magnetic resonance (NMR) spectroscopy, respectively. The specific details and procedure to calculate the Faradaic efficiency for different products have been addressed in the previous reports.[5,6]

## C.3 Results and Discussion

The different powder samples were physically characterized using XRD and BET measurements. The diffraction lines observed for synthesized $Ti_3O_5$ corresponded to monoclinic $\gamma$-$Ti_3O_5$ phase (JCPDS # 97-003-5148) as shown in **Figure C.1**. The weight fractions of anatase and rutile in $TiO_2$ P25 were calculated using the empirical equation described by Spurr and Myres[7].

$$W_R/W_A = 1.22 \times I_R/I_A - 0.028 \qquad [1]$$

where $W_R$ and $W_A$ are the respective weight fractions for rutile and anatase, while $I_R$ and $I_A$ denote the intensity of observed rutile (110) peak at 27.35° and anatase (101) peak at 25.16° 2θ, respectively. The crystallite size was also calculated for these powders using Scherrer's equation, ($d = 0.9\lambda/(\beta \times \cos\theta)$, where $d$ is the crystallite size; $\lambda$, X-ray wavelength; $\beta$, the full width at half maximum; and $\theta$, the diffraction angle) based on the observed first diffraction peak for these samples. The crystallite size was found to be 18, 32 and 41 nm for $TiO_2$, γ-$Ti_3O_5$ and TiO, respectively. The BET surface area and catalyst loading for different electrodes are listed in **Table C.1**.

The gas diffusion electrodes (GDEs) of these samples were studied in a PEMFC based full electrochemical cell. The products of $CO_2$ reduction reaction were observed along with hydrogen evolution at the cathode side. **Figure C.2** shows the trend in the Faradaic efficiency for CO and formate, formed during electrochemical reduction of $CO_2$, as a function of cell voltage. As evident from these results, the nonstoichiometric phase, γ-$Ti_3O_5$ exhibits the highest selectivity for $CO_2$ reduction. In the case of γ-$Ti_3O_5$, CO formation started with a Faradaic efficiency of ~ 3% at -1.4 V, corresponding to a total overpotential of ~ -0.9 V with respect to apparent cell potential of -0.51 V, considering anodic reaction ($2H^+ + 2e^- = H_2$, $E^o$ = 0 V vs. NHE) and cathodic reaction ($CO_2 + 2H^+ + 2e^- = CO + H_2O$, $E^o$ = -0.10 V vs. NHE) at pH 7.

**Table C.1.** BET surface area and catalyst loading for various samples

| **Sample** | **BET surface area ($m^2/g$)** | **Catalyst loading (mg $cm^{-2}$)** |
|---|---|---|
| $TiO_2$ P25 | 38.8 | 2.14 |
| γ-$Ti_3O_5$ | 10.3 | 1.74 |
| TiO | 8.5 | 1.81 |

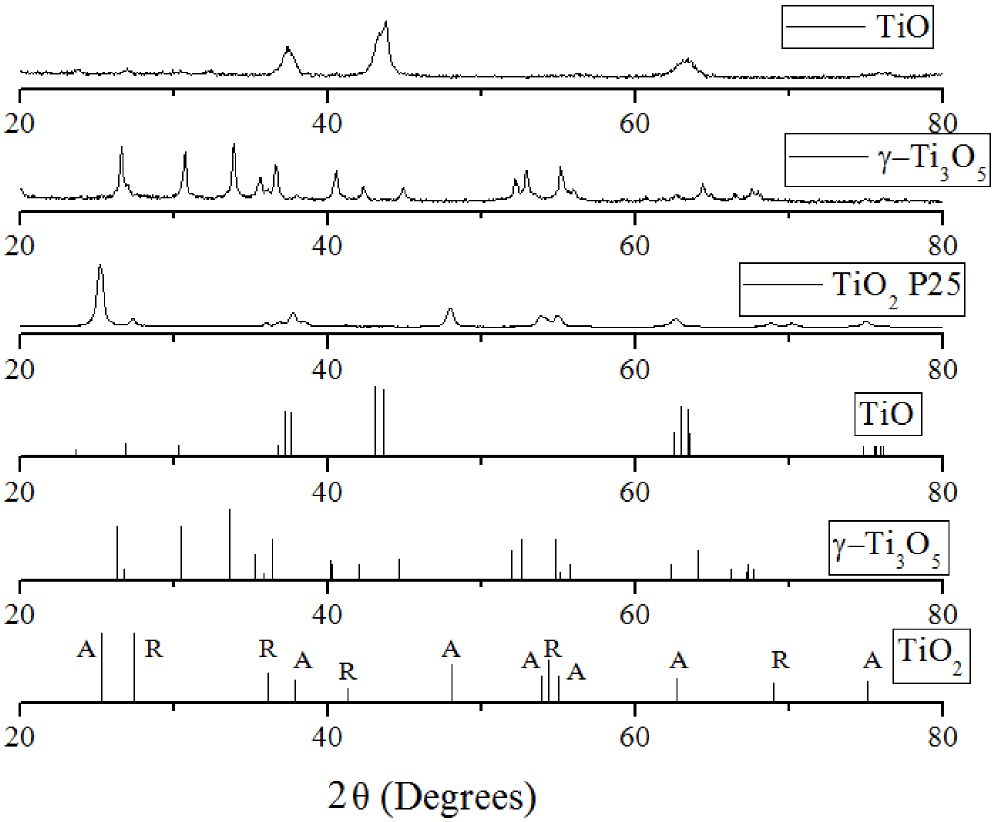

**Figure C.1.** XRD results of $TiO_2$ P25, $Ti_3O_5$ and TiO ball milled powders along with standard diffraction patterns; $TiO_2$, both anatase and rutile phases, standard diffraction lines represented by A and R respectively

On the other hand, formate formation for γ-$Ti_3O_5$ also started at -1.4 V with a Faradaic efficiency of ~ 4%, corresponding to an overpotential of ~ -0.8 V with respect to apparent cell potential of -0.61 V, considering anodic reaction ($2H^+ + 2e^- = H_2$, E° = 0 V vs. NHE) and cathodic reaction ($CO_2 + 2H^+ + 2e^- = HCOOH$, E° = -0.20 V vs. NHE) at pH 7. The Faradaic efficiency for CO reached a maximum of ~7% at -2.5 V for γ-$Ti_3O_5$ while being only ~3% for both $TiO_2$ P25 and TiO. On the similar trend, the highest Faradaic efficiency for formate for γ-$Ti_3O_5$ was observed ~ 10% at -2.3 V while only ~

3% for $TiO_2$ and TiO. **Figure C.3** depicts the trend in partial current density for CO and formate for these electrodes at different cell voltages. While the highest partial current density for CO formation was observed for $\gamma$-$Ti_3O_5$ ~ -1.5 mA/cm$^2$ at an overpotential of ~ -2 V, in comparison to only ~ -0.5 mA/cm$^2$ for both $TiO_2$ and TiO; the highest partial current density for formate formation for $\gamma$-$Ti_3O_5$ was ~ 2 mA/cm$^2$, in comparison to – 0.5 mA/cm$^2$ for $TiO_2$ and TiO, corresponding to an overpotential of ~ -1.9 V. The energy efficiency for both CO and formate formation was also calculated by the following equation:

$$\text{Energy efficiency} = E_{eq}\times\text{Faradaic efficiency/Applied cell voltage} \qquad [2]$$

where $E_{eq}$ is the apparent standard potential, which is -0.51 and -0.61 V for CO and formate respectively. The variation in energy efficiency for the formation of CO and formate with cell voltage is shown in **Figure C.4**. The energy efficiency, both for the formation of CO and formate is ~ 1.5 and 3% respectively, much higher on $\gamma$-$Ti_3O_5$ electrodes than $TiO_2$ and TiO ~ 0.5% for both CO and formate.

The reaction mechanism and approaches to increase the electrochemical properties of $TiO_{2-x}$ electrodes are being investigated. Our recent work showed that not only the nonstoichiometry but also the crystal structure play a key role in determining the selectivity and the activity of $TiO_{2-\square}$-based electrodes. Indeed, the surface defects, such as $Ti^{3+}$ and oxygen vacancies present in $\gamma$-$Ti_3O_5$, might act as active sites for electrochemical $CO_2$ reduction.

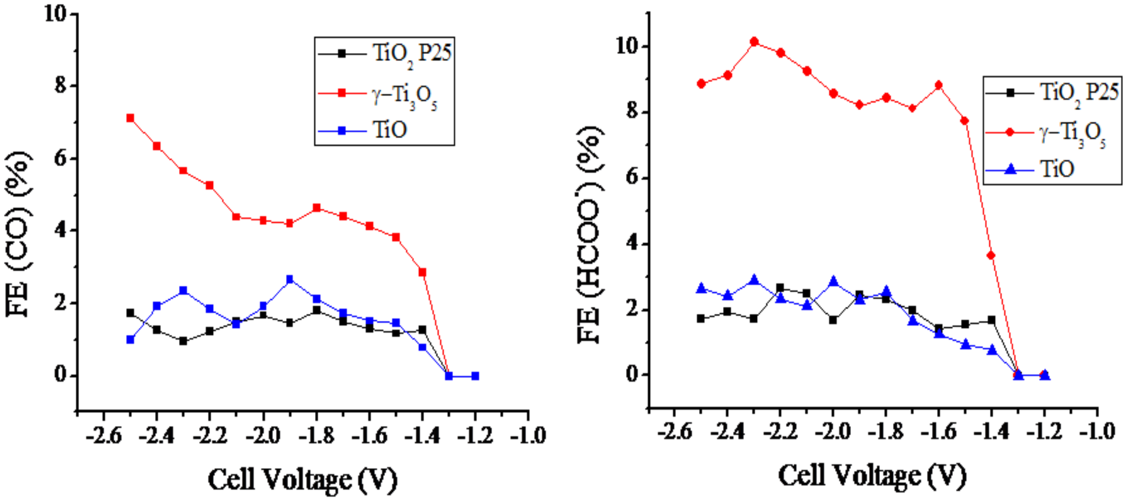

**Figure C.2.** Faradaic efficiency for CO and formate formation as a function of cell voltage on different $TiO_x$ electrodes

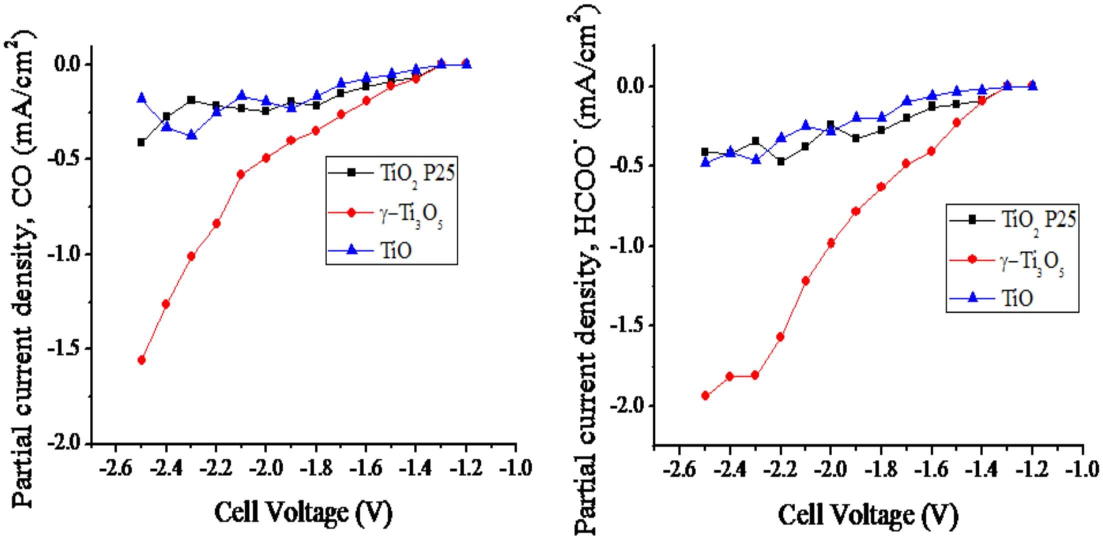

**Figure C.3.** Partial current density for CO and formate formation as a function of cell voltage on different $TiO_x$ electrodes

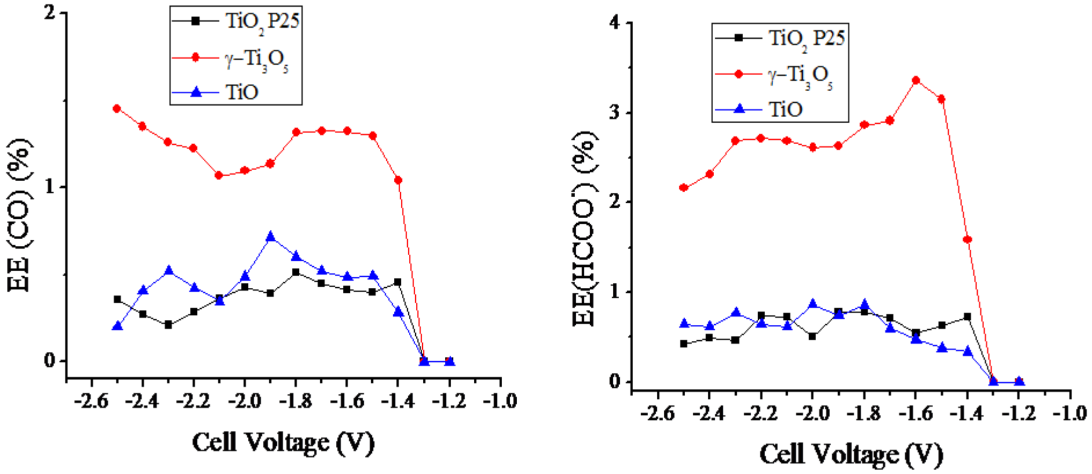

**Figure C.4.** Energy efficiency for CO and formate formation as a function of cell voltage on different $TiO_x$ electrodes

The reaction mechanism for $CO_2$ reduction on γ-$Ti_3O_5$ might consist of these steps, represented by Eqs. [3] – [6], as proposed for $CO_2$ photoreduction on brookite and anatase $TiO_2$ with $Ti^{3+}$ and oxygen vacancy as the surface defects.[8] Though the presence of surface defects significantly impact the electrocatalytic activity, the surface structure of $TiO_2$ polymorphs also plays a key role in the selectivity towards electrochemical $CO_2$ reduction.[9]

$$CO_2 + Ti^{3+} = Ti^{4+} - CO_2^- \qquad [3]$$

$$CO_2^- + H^+ + e^- = CO + OH^- \qquad [4]$$

$$CO_2^- + [Ti^{3+} - V_o - Ti^{4+}] = CO + [Ti^{4+} - O^{2-} - Ti^{4+}] \qquad [5]$$

$$CO_2^- + 2H^+ + e^- = HCOOH \qquad [6]$$

## C.4 Conclusions

In summary, the nonstoichiometric $TiO_x$ ($\gamma$-$Ti_3O_5$) is synthesized by the reduction of $TiO_2$ P25 nanoparticles in the presence of hydrogen at 900° C and ambient pressure. Further, the electrocatalytic activity of $\gamma$-$Ti_3O_5$ is demonstrated for $CO_2$ reduction to CO and formate in a PEMFC based full electrochemical cell. The selectivity of $\gamma$-$Ti_3O_5$ towards $CO_2$ reduction is found to be higher than stoichiometric $TiO_x$, i.e. both $TiO_2$ P25 and TiO. The performance of $\gamma$-$Ti_3O_5$ though remains low as compared to other metallic catalysts such as Sn and Cu; this work, however, shows the potential application of nonstoichiometric $TiO_x$ as electrocatalysts for proton-coupled electron transfer reactions.

## References

1. J. Anderson, B. Collen, U. Kuylenstierna, A. Magneli, *Acta. Chem. Scand.*, **11**, 1641 (1957).
2. R. A. Palmer, T. M. Doan, P. G. Lloyd, B. L. Jarvis, N. U. Ahmed, *Plasma Chem. Plasma Process.*, **22**(3), 335 (2002).
3. X. Li, A. L. Zhu, W. Qu, H. Wang, R. Hui, L. Zhang, *Electrochim. Acta.*, **55**, 5891 (2010).
4. N. Stem, E. D. Chinaglia, S. G. D. S. Filho, *ECS Trans.*, **39**(1), 347 (2011).
5. J. Wu, F. G. Risalvato, P. P. Sharma, P. J. Pellechia, F. S. Ke, X. D. Zhou, *J. Electrochem. Soc.*, **160**(9), F953 (2013).
6. J. Wu, F. G. Risalvato, F. S. Ke, P. J. Pellechia, X. D. Zhou, *J. Electrochem. Soc.*, **159**(7), F353 (2012).
7. R. A. Spurr, H. Myers, *Anal. Chem.*, **29**(5), 760 (1957).
8. L. Liu, H. Zhao, M. J. Andino, Y. Li, *ACS Catalysis,* **2**, 1817 (2012).
9. P. P. Sharma, F. S. Ke, X. D. Zhou, unpublished data

# Appendix D: Author's Publications

1. J. Wu, R. M. Yadav, M. Liu, **P. P. Sharma**, C. S. Tiwary, L. Ma, X. Zou, X.-D. Zhou, B. I. Yakobson, J. Lou, P. M. Ajayan, "Achieving Highly Efficient, Selective and Stable $CO_2$ Reduction on Carbon Nanotubes", *ACS Nano* **2015**, 9, 5364.
2. **P. P. Sharma**, J. Wu, R. M. Yadav, M. Liu, C. J. Wright, C. S. Tiwary, B. I. Yakobson, J. Lou, P. M. Ajayan, X.-D. Zhou, "Nitrogen Doped Carbon Nanotube Arrays for High Efficiency Electrochemical Reduction of $CO_2$: On the Understanding of Defects, Defect Density, and Selectivity", *Angew. Chem.* **2015**, 127, 13905.
3. J. Wu, M. Liu, **P. P. Sharma**, R. M. Yadav, L. Ma, Y. Chao, X.-D. Zhou, B. I. Yakobson, J. Lou, P. M. Ajayan, "Incorporation of Nitrogen Defects for Efficient Reduction of $CO_2$ via Two-Electron Pathway on Three-Dimensional Graphene Foam", *Nano Lett.* **2016**, 16, 466.
4. J. Wu, **P. P. Sharma**, B. Harris, X.-D. Zhou, "Dependence of the Faradaic efficiency and current density on the microstructure and thickness of tin electrode towards the electrochemical conversion of $CO_2$ into formate", *J. Power Sources* **2014**, 258, 189.
5. J. Wu, F. G. Risalvato, **P. P. Sharma**, X.-D. Zhou, "Electrochemical Reduction of Carbon Dioxide II. Design, Assembly and Performance of Low Temperature Electrochemical Cells" *J. Electrochem. Soc.* **2013**, 160, F953.

6. **P. P. Sharma**, F-S. Ke, X.-D. Zhou. “The Role of Nonstoichiometry on the Electrocatalytic Properties of $TiO_{2-\delta}$ towards the Conversion of Carbon Dioxide to Fuels”, *ECS Trans.* **2014**, 61 (1), 331.
7. J. Wu, B. Harris, **P. P. Sharma**, X.-D. Zhou, “Morphological Stability of Sn Electrode for Electrochemical Conversion of $CO_2$”, *ECS Trans.* **2013** 58 (2), 71.
8. **P. P. Sharma**, F.-S. Ke, C. J. Wright, J. Wu, Y. Wu, J. Qiao, X.-D. Zhou, “Selective Formation of $C_2$ Products from the Electrochemical Conversion of $CO_2$ on Cu Electrodes Comprised of Nanoporous Ribbon Arrays”, submitted.
9. **P. P. Sharma**, X.-D. Zhou, “Electrocatalytic Conversion of Carbon Dioxide to Fuels: A Review on the Interaction between $CO_2$ and the Liquid Electrolyte”, submitted.